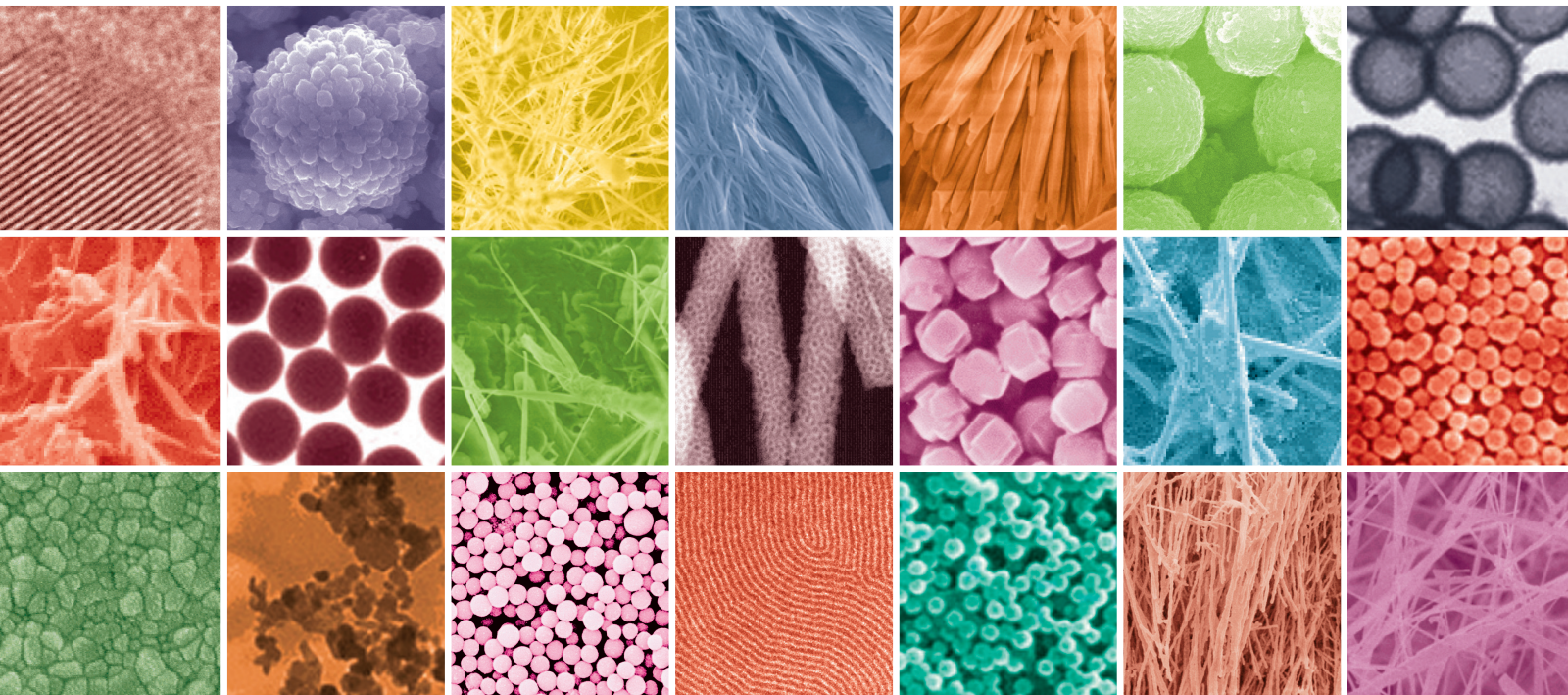


Concepts of Novel Nanomaterial Device and Application

Guest Editors: Ting-Jen Hsueh, Sheng-Po Chang, Shyh-Jer Huang,
Chieh-Chih Huang, and Michael Hu





Concepts of Novel Nanomaterial Device and Application

Concepts of Novel Nanomaterial Device and Application

Guest Editors: Ting-Jen Hsueh, Sheng-Po Chang,
Shyh-Jer Huang, Chieh-Chih Huang, and Michael Hu



Copyright © 2014 Hindawi Publishing Corporation. All rights reserved.

This is a special issue published in "Journal of Nanomaterials." All articles are open access articles distributed under the Creative Commons Attribution License, which permits unrestricted use, distribution, and reproduction in any medium, provided the original work is properly cited.

Editorial Board

Katerina E. Aifantis, USA
Nageh K. Allam, USA
Margarida Amaral, Portugal
Xuedong Bai, China
Lavinia Balan, France
Enrico Bergamaschi, Italy
Theodorian Borca-Tasciuc, USA
C. Jeffrey Brinker, USA
Christian Brosseau, France
Xuebo Cao, China
Shafiq Chowdhury, USA
Kwang-Leong Choy, UK
Cui ChunXiang, China
Miguel A. Correa-Duarte, Spain
Shadi A. Dayeh, USA
Ali Eftekhari, USA
Claude Estournés, France
Alan Fuchs, USA
Lian Gao, China
Russell E. Gorga, USA
Hongchen Chen Gu, China
Mustafa O. Guler, Turkey
John Z. Guo, USA
Smrati Gupta, Germany
Michael Harris, USA
Zhongkui Hong, China
Michael Z. Hu, USA
David Hui, USA
Y.-K. Jeong, Republic of Korea
Sheng-Rui Jian, Taiwan
Wanqin Jin, China
Rakesh K. Joshi, UK
Zhenhui Kang, China
Fathallah Karimzadeh, Iran
Alireza Khataee, Iran

Do K. Kim, Korea
Alan K. T. Lau, Hong Kong
Burtrand Lee, USA
Jun Li, Singapore
Benxia Li, China
Xing-Jie Liang, China
Shijun Liao, China
Gong-Ru Lin, Taiwan
Tianxi Liu, China
Jun Liu, USA
Songwei Lu, USA
Daniel Lu, China
Jue Lu, USA
Ed Ma, USA
Gaurav Mago, USA
Santanu K. Maiti, India
Sanjay R. Mathur, Germany
Vikas Mittal, UAE
Weihai Ni, Germany
Sherine Obare, USA
Atsuto Okamoto, Japan
Abdelwahab Omri, Canada
Edward A. Payzant, USA
Kui-Qing Peng, China
Anukorn Phuruangrat, Thailand
Mahendra Rai, India
Suprakas Sinha Ray, South Africa
Ugur Serincan, Turkey
Huaiyu Shao, Japan
Donglu Shi, USA
Vladimir Sivakov, Germany
Marinella Striccoli, Italy
Bohua Sun, South Africa
Saikat Talapatra, USA
Nairong Tao, China

Titipun Thongtem, Thailand
Somchai Thongtem, Thailand
Alexander Tolmachev, Ukraine
Valeri P. Tolstoy, Russia
Tsung-Yen Tsai, Taiwan
Takuya Tsuzuki, Australia
Raquel Verdejo, Spain
Mat U. Wahit, Malaysia
Zhenbo Wang, China
Ruiping Wang, Canada
Shiren Wang, USA
Cheng Wang, China
Yong Wang, USA
Jinquan Wei, China
Ching-Ping Wong, Hong Kong
Xingcai Wu, China
Guodong Xia, Hong Kong
Ping Xiao, UK
Zhi Li Xiao, USA
Yangchuan Xing, USA
Shuangxi Xing, China
Nanping Xu, China
Doron Yadlovker, Israel
Yingkui Yang, China
Khaled Youssef, USA
Kui Yu, Canada
William W. Yu, USA
Haibo Zeng, China
Tianyou Zhai, China
Renyun Zhang, Sweden
Bin Zhang, China
Yanbao Zhao, China
Lianxi Zheng, Singapore
Chunyi Zhi, Hong Kong

Contents

Concepts of Novel Nanomaterial Device and Application, Ting-Jen Hsueh, Sheng-Po Chang, Shyh-Jer Huang, Chieh-Chih Huang, and Michael Hu
Volume 2014, Article ID 414790, 1 page

Damp-Heat Induced Performance Degradation for InGaP/GaAs/Ge Triple-Junction Solar Cell, Hwen-Fen Hong, Tsung-Shiew Huang, Wu-Yih Uen, and Yen-Yeh Chen
Volume 2014, Article ID 410717, 6 pages

Terahertz Performance of a GaN-Based Planar Nanochannel Device, K. Y. Xu, Y. N. Wang, C. J. Zheng, J. W. Xiong, and G. Wang
Volume 2014, Article ID 850915, 5 pages

Microstructures and Recording Mechanism of Mo/Si Bilayer Applied for Write-Once Blue Laser Optical Recording, Sin-Liang Ou, Kuo-Sheng Kao, Han-Feng Chang, Tsung-Shine Ko, and Chin-Yen Yeh
Volume 2014, Article ID 862928, 6 pages

Structural, Surface Morphology and Optical Properties of ZnS Films by Chemical Bath Deposition at Various Zn/S Molar Ratios, Fei-Peng Yu, Sin-Liang Ou, Pin-Chuan Yao, Bing-Rui Wu, and Dong-Sing Wu
Volume 2014, Article ID 594952, 7 pages

Investigation of Low-Frequency Noise Characterization of 28-nm High-k pMOSFET with Embedded SiGe Source/Drain, Shih-Chang Tsai, San-Lein Wu, Jone-Fang Chen, Bo-Chin Wang, Po Chin Huang, Kai-Shiang Tsai, Tsung-Hsien Kao, Chih-Wei Yang, Cheng-Guo Chen, Kun-Yuan Lo, Osbert Cheng, and Yean-Kuen Fang
Volume 2014, Article ID 787132, 6 pages

Texture-Etched SnO₂ Glasses Applied to Silicon Thin-Film Solar Cells, Bing-Rui Wu, Sin-Liang Ou, Shih-Yung Lo, Hsin-Yuan Mao, Jhen-Yu Yang, and Dong-Sing Wu
Volume 2014, Article ID 907610, 9 pages

Resistive Switching Characteristics of a SiO_x Layer with CF₄ Plasma Treatment, Chih-Yi Liu, Yueh-Ying Tsai, Wen-Tsung Fang, and Hung-Yu Wang
Volume 2014, Article ID 703463, 5 pages

Enhanced Performance of Mg_{0.1}Zn_{0.9}O UV Photodetectors Using Photoelectrochemical Treatment and Silica Nanospheres, Hsin-Ying Lee, Yu-Chang Lin, Meng-Ju Lee, Wu-Yih Uen, and Kondepudy Sreenivas
Volume 2014, Article ID 972869, 6 pages

Performance Improvement of GaN-Based Flip-Chip White Light-Emitting Diodes with Diffused Nanorod Reflector and with ZnO Nanorod Antireflection Layer, Hsin-Ying Lee, Yu-Chang Lin, Yu-Ting Su, Chia-Hsin Chao, and Véronique Bardinal
Volume 2014, Article ID 987479, 6 pages

P3HT:PCBM Incorporated with Silicon Nanoparticles as Photoactive Layer in Efficient Organic Photovoltaic Devices, Shang-Chou Chang, Yu-Jen Hsiao, and To-Sing Li
Volume 2013, Article ID 354035, 4 pages

Improvement of Charge-Discharge Characteristics of the Mg-Ni Powder Electrodes at 55°C, Kuan-Jen Chen, Fei-Yi Hung, Truan-Sheng Lui, and Ren-Syuan Xiao
Volume 2013, Article ID 638953, 6 pages

Editorial

Concepts of Novel Nanomaterial Device and Application

**Ting-Jen Hsueh,¹ Sheng-Po Chang,² Shyh-Jer Huang,³
Chieh-Chih Huang,⁴ and Michael Hu⁵**

¹ National Nano Device Laboratories, Tainan-Based Science Park, Tainan 741, Taiwan

² Advanced Optoelectronic Technology Center, National Cheng Kung University, Tainan 70101, Taiwan

³ Department of Electrical Engineering, University of California, Los Angeles, CA 90095-1594, USA

⁴ Low Energy Electronic Systems, Singapore-MIT Alliance for Research and Technology, Singapore 138602

⁵ Oak Ridge National Laboratory, Oak Ridge, TN 37831, USA

Correspondence should be addressed to Ting-Jen Hsueh; tj.hsueh@gmail.com

Received 23 June 2014; Accepted 23 June 2014; Published 10 July 2014

Copyright © 2014 Ting-Jen Hsueh et al. This is an open access article distributed under the Creative Commons Attribution License, which permits unrestricted use, distribution, and reproduction in any medium, provided the original work is properly cited.

Nanomaterial comprises several hundred atoms and molecules, which a lot of complicated and interesting interactions occur in it. Characteristics in nanoscale, such as transmittance, electrical conductivity, thermal conductivity, magnetic, corrosion, and other effects.

Furthermore, nanomaterial manufacturing technology is applied on all kinds of nanomaterial devices, such as photo device, FET, and biosensor, and enhances electronic, optical, and mechanical properties. Most importantly, taking advantage of nanotechnology, the cost of devices will go down with better quality.

This special issue is about novel nanomaterials device and applications and other related fields. This special issue enables interdisciplinary collaboration between material science and engineering technologists in the academic and industrial fields. The paper describes sealed and non-sealed InGaP/InGaAs/Ge triple-junction solar cell in a complex high temperature and high humidity environment and investigated the electrical properties over time. Another paper presents combined two-dimensional-three-dimensional (2D-3D) ensemble Monte Carlo (EMC) model, and the performance of a planar nanochannel device is studied at the terahertz (THz) region. Another paper is on Mo/Si bilayer thin films which were grown by magnetron sputtering and applied to write-once blu-ray disc (BD-R). Another paper studies the ZnS thin films which were prepared on glass substrates by chemical bath deposition at various Zn/S molar ratios from 1/50 to 1/150. Another paper describes low-frequency noise characterizations in 28 nm high-k (HK)

pMOSFET with embedded SiGe source/drain (S/D) through noise and random telegraph noise measurements simultaneously. Another paper adopts transparent electrodes of tin dioxide (SnO₂) on glasses which were further wet-etched in the diluted HCl:Cr solution to obtain larger surface roughness and better light-scattering characteristic for thin-film solar cell applications.

The paper describes A 20 nm SiO_x layer which is deposited using radiofrequency sputtering to form the resistive switching layer of a Cu/SiO_x/Pt memory device. Another paper proposes Mg_{0.1}Zn_{0.9}O films which were grown using atomic layer deposition (ALD) system and applied to metal-semiconductor-metal ultraviolet photodetectors (MSM-UPDs) as an active layer. Another paper describes GaN-based flip-chip white light-emitting diodes (FCWLEDs) with diffused ZnO nanorod reflector and with ZnO nanorod antireflection layer which were fabricated. Another paper proposes to use silicon nanoparticles doped poly(3-hexylthiophene) and [6,6]-phenyl C61-butyric acid methyl ester blends (P3HT : PCBM : Si NP) which have been produced as the photoactive layer of organic photovoltaic devices (OPVs). Another paper of this special issue uses magnesium-nickel (Mg-Ni) powders which are used as the anode materials for secondary lithium (Li) ion batteries.

*Ting-Jen Hsueh
Sheng-Po Chang
Shyh-Jer Huang
Chieh-Chih Huang
Michael Hu*

Research Article

Damp-Heat Induced Performance Degradation for InGaP/GaAs/Ge Triple-Junction Solar Cell

Hwen-Fen Hong,¹ Tsung-Shiew Huang,¹ Wu-Yih Uen,² and Yen-Yeh Chen³

¹ Department of Materials Science and Engineering, National Tsing Hua University, Hsinchu 30013, Taiwan

² Department of Electronic Engineering, College of Electrical Engineering and Computer Science, Chung Yuan Christian University, Chungli 32023, Taiwan

³ Institute of Nuclear Energy Research, 1000 Wenhua Road, Jiaan Village, Longtan, Taoyuan 32546, Taiwan

Correspondence should be addressed to Hwen-Fen Hong; d937537@oz.nthu.edu.tw

Received 23 December 2013; Revised 8 January 2014; Accepted 10 January 2014; Published 24 April 2014

Academic Editor: Ting-Jen Hsueh

Copyright © 2014 Hwen-Fen Hong et al. This is an open access article distributed under the Creative Commons Attribution License, which permits unrestricted use, distribution, and reproduction in any medium, provided the original work is properly cited.

We performed accelerated tests on sealed and nonsealed InGaP/InGaAs/Ge triple-junction (TJ) solar cells in a complex high temperature and high humidity environment and investigated the electrical properties over time. The degradation of energy conversion efficiency in nonsealed cells was found to be more serious than that in sealed cells. The short-circuit current (I_{SC}), open-circuit voltage (V_{OC}), and fill factor (FF) of sealed cells changed very slightly, though the conversion efficiency decreased 3.6% over 500 h of exposure. This decrease of conversion efficiency was suggested to be due to the deterioration of silicone encapsulant. The I_{SC} , V_{OC} , and FF of nonsealed cells decreased with increasing exposure time. By EL and SEM analysis, the root causes of degradation can be attributed to the damage and cracks near the edge of cells induced by the moisture ingress. It resulted in shunt paths that lead to a deterioration of the conversion efficiency of solar cell by increasing the leakage current, as well as decreasing open-circuit voltage and fill factor of nonsealed solar cells.

1. Introduction

TJ solar cells are fabricated using organometallic vapor phase epitaxy (OMVPE) to deposit subcells of GaInP and GaInAs on Ge substrate [1]. A TJ solar cell consists of three individual subcells that are stacked on top of each other to form a series connection. The individual subcells are connected to each other through very thin tunnel junction film of several nanometers. These tunnel junctions are typically very thin to allow the tunneling mechanism to dominate the majority carrier transport [2]. Among solar technologies, TJ solar cells have attracted increasing attention owing to their very high conversion efficiencies [3, 4] as well as long term stability [5–7]. TJ solar cells based on III–V semiconductors are being evaluated globally in concentrator photovoltaic (CPV) systems designed to supplement electricity generation for utility companies. III–V TJ solar cells, with demonstrated efficiency over 40% since 2007 [8], strongly reduce the cost of CPV systems and make III–V multijunction concentrator

cells the technology of choice for most concentrator systems today. The world's highest energy conversion efficiency solar cells with 44.7% have been demonstrated on June 2013 [9]. In fact, the III–V TJ solar cells have nanoscale thin films which can take good advantage of solar light from 300 nm to 1800 nm.

In recent years, there have been many research groups that reported the improvements of III–V triple-junction concentration solar cells using different approaches [10–13]. In addition to pursuing high efficiency for III–V concentration solar cells, one should also understand the degradation mechanism of these devices to maintain their reliability. The reliability of III–V single-junction, dual-junction, and multijunction concentration solar cells has been analyzed by some research groups using different methods and strategies. However, so far, the studies about the reliability on GaInP/GaInAs/Ge concentration solar cells were rather rare and almost focused on clarifying the degradation induced by thermal stress [14–17]. It is believed that the understanding

of mechanism of degradation caused by moisture will favor the upgrading qualities of III–V triple-junction concentration solar cells. Once the reliability of III–V triple-junction concentration solar receivers is realized, the prospect of the HCPV systems will be more clearly demonstrated.

The aim of this study is to examine the degradation mechanism of GaInP/GaInAs/Ge triple-junction solar receivers by accelerated damp-heat environment test. These results are considered to be helpful for researchers to understand the causes of degradation and improve the efficiency and stability of TJ solar cells.

2. Samples Preparation and Test Description

IEC62108 standard is the most commonly used test method for concentrator solar receivers. In this study, III–V InGaP/InGaAs/Ge concentrator solar cells were exposed to 85°C and 85% relative humidity without electrical bias according to IEC 62108 standard. A photograph of typical concentrator solar receiver used in this study is shown in Figure 1, including concentrator solar cell, protection silicone layer, bypass diode, ceramic substrate, and heat sink. The cells with active area of 0.3025 (0.55 × 0.55) cm² were glued to aluminum plates using an adhesive. The schematic structure of the GaInP/GaInAs/Ge triple-junction concentrator solar cell is shown in Figure 2, and the schematic graph of cross-section of silicone sealed cell is shown in Figure 3. Those concentration solar cells are divided into two groups. One is denoted as test *A* with 20 pieces of cells protected with optical silicone layer. The other is denoted as test *B* with 20 cells without any protection layer. Test *B* is designed to provide a contrast to test *A*, which is favorable for analyzing the predominant factor in degradation of solar cells. The experimental time sequence of accelerated degradation test for tests *A* and *B* is the same.

Finally, we have performed both dark current versus voltage (DIV) and light current versus voltage (LIV) tests for all solar cells to analyze the variation of their electrical characteristics. We have also visually inspected samples before humidity exposure and after 100, 200, 300, 400, and 500 h of exposure. According to IEC62108 standard, samples should be tested over 2000 h; however, we have observed apparent degradation in nonsealed cells after 500 h of damp-heat exposure. We therefore report these results in advance. A solar simulator (WACOM WXS-155S-L2) was used to measure the LIV. In the meanwhile, scanning electron micrographic (SEM) and electroluminescent (EL) examinations were applied to understand the root cause of degradation in this investigation.

3. Results and Discussion

The collected average performance data of sealed and bare solar cells are shown in Table 1. It can be seen that the energy conversion efficiency of sealed cells degraded by 3~4% after 500 h exposure. However, V_{oc} and FF except I_{sc} changed only very slightly in sealed cells. On the surface of the sealed cells, no significant morphological change was observable.

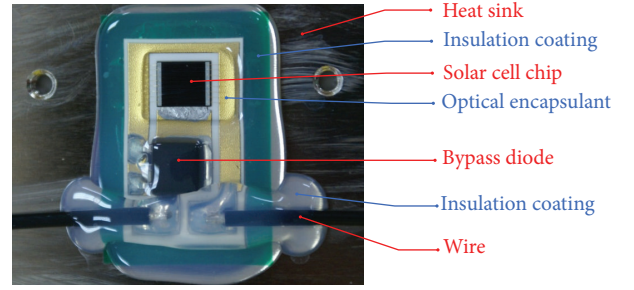


FIGURE 1: Picture of concentrator solar receiver used in this study.

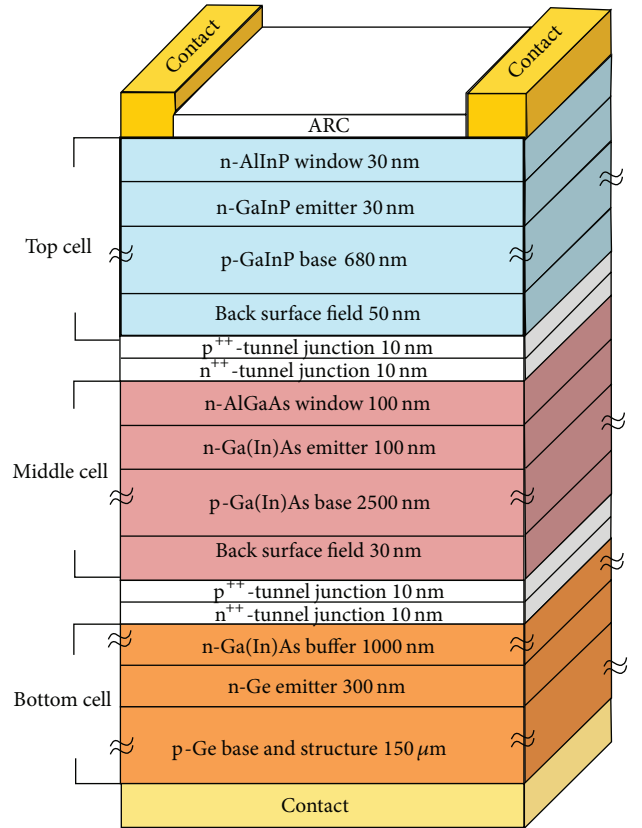


FIGURE 2: Schematic structure of GaInP/GaInAs/Ge triple-junction solar cell.

TABLE 1: Performance of sealed and bare solar cells after damp-heat test.

Type	$\Delta I_{sc}/I_{sc(initial)}$	$\Delta V_{oc}/V_{oc(initial)}$	$\Delta FF/FF_{(initial)}$	$\Delta \eta/\eta_{(initial)}$
Sealed	-0.978%	-0.071%	-0.013%	-3.59%
Bare	-1.098%	-0.102%	-1.531%	-5.55%

Figure 4 shows the typical dark I - V curves of solar cells which were measured sequentially after each 100 h time interval. In general, the dark current of III–V solar cells as a function of bias voltage can be formulated by double exponential terms [18] as described in

$$I_{\text{dark}}(V) = I_{\text{diff}}(V) + I_{\text{scr}}(V). \quad (1)$$

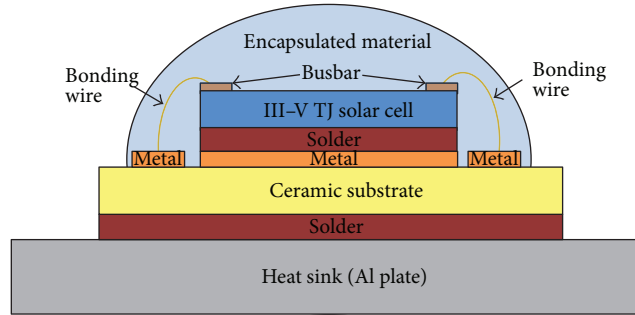


FIGURE 3: Schematic graph of cross-section of concentrator solar receiver.

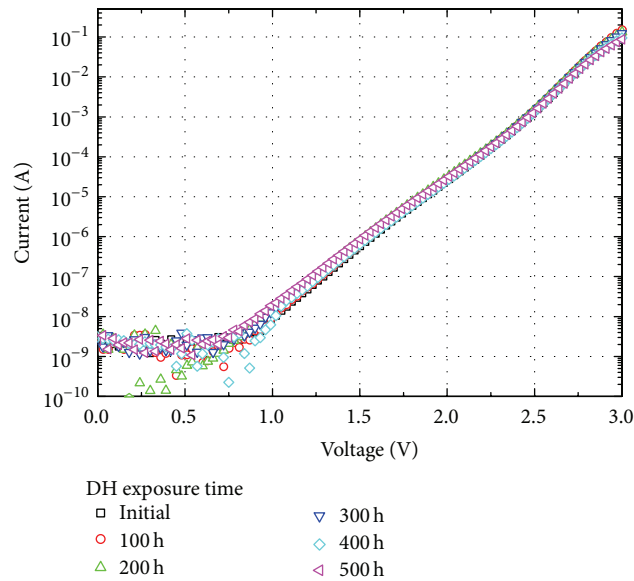


FIGURE 4: Typical dark I - V curves of sealed cells measured sequentially after each step of damp-heat exposures.

Here, $I_{\text{diff}}(V)$ denotes the diffusion current in the neutral region and $I_{\text{scr}}(V)$ is related to the generation-recombination current in the depletion region. In general, the dark current is dominated by recombination current at low voltage and by diffusion current at high voltage. Since the decrease of FF was very small, this implied that both shunt and series resistances did not change apparently. From Figure 4, it is noteworthy that almost all sealed cells showed similar dark I - V characteristics. No obvious difference can be recognized between these I - V curves implying that both I_{diff} and I_{scr} did not change even after 500 h of exposure. In other words, there were no significant defects generated, which would increase the recombination current [19]. We believe that there is no deterioration of electrical characteristics in sealed cells. Hence, the losses of conversion efficiency were suggested to be due to encapsulant material. These results are similar to that reported previously by McIntosh et al. [20]. They reported that water moisture can diffuse into silicone materials, then the water molecules will scatter incident light and decrease the transmission coefficient of silicone materials, thus decrease the short-circuit current and conversion efficiency.

As for bare solar cells, the average energy conversion efficiency of 20 cells after 500 h of exposure degraded by 5~6%, which is higher than the data of sealed cells. It is worth mentioning that there are two cells that are denoted as S1 and S2 and degraded over 10% on energy conversion efficiency. The light I - V and dark I - V curves of S1 are shown in Figures 5(a) and 5(b), respectively. The variation of I_{SC} was not apparent over the damp-heat test. The degradation of V_{OC} was also not apparent before 400 h exposure; however, V_{OC} decreased significantly after 500 h of exposure. From the EL images of 400 h and 500 h exposed samples, as shown in Figure 6, some different color zones near the edge of cells can be observed. It reveals that some defects were generated after 500 h of damp-heat test. Evidently, these defects increase $I_{\text{scr}}(V)$, therefore, result in the elevation of I_{dark} and a significant decrease in V_{OC} .

Figures 7(a) and 7(b) show the light I - V curves and dark I - V curves of S2 cell before and after 100, 200, 300, 400, and 500 h of exposure in damp-heat environment, respectively. It exhibits a linear (ohmic) behavior after 500 h of exposure. It is well known that a lot of commercially produced silicon solar cells have a problem caused by local

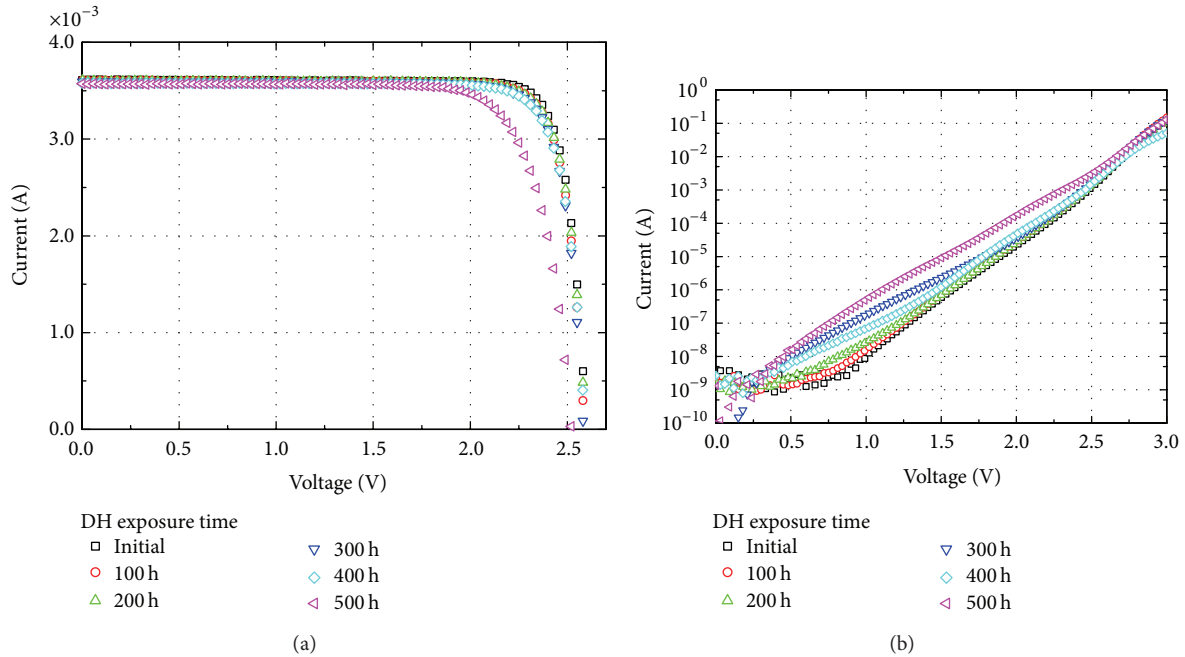


FIGURE 5: (a) Light *I-V* and (b) dark *I-V* curves of bare cell S1 measured sequentially after each step of damp-heat exposures.

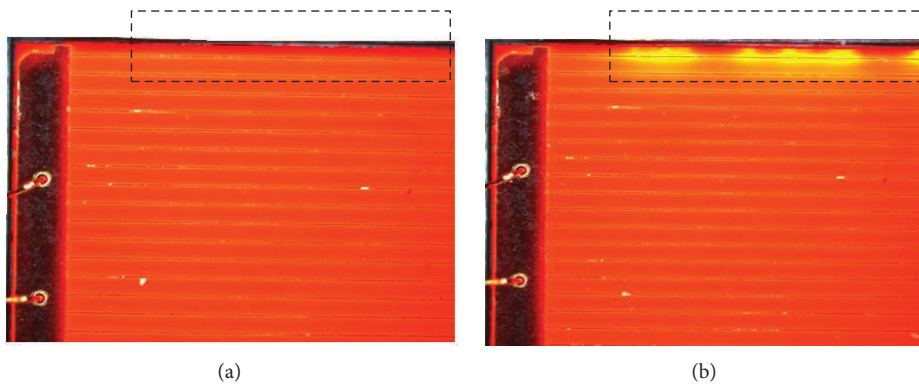


FIGURE 6: EL images of sample S1 after 400 h (a) and 500 h (b) of exposure.

short circuits called shunts [21]. These shunts may lead to a deterioration of the conversion efficiency of solar cells by increasing the leakage current and decreasing both the open-circuit voltage and the fill factor of the solar cells. Shunts in solar cells often localized at the cell edges. Some of these edge shunts have a linear *I-V* (ohmic) behavior and some of them have a nonlinear *I-V* (diode-like). To analyze the cause of the sudden degradation after 500 h of exposure, we performed SEM and EDX examination for S2. Figure 8 shows the EL images of S2 after 400 h and 500 h of exposures. No obvious damage was found in the EL image of 400 h exposed sample; however bright zones, as marked by dashed-rectangle, appeared in the 500 h of exposed sample. We inspected the bright zone with SEM and found that a particle existed in the zone, which was furthermore identified by EDX to be a segregated particle composed mainly of Au. Therefore, the bright zone exhibited low resistance, and leakage current resulted in shunts. The SEM micrograph of Figure 9 also

shows a crack at the edge, as marked by a circle. Figure 10 shows an enlarged SEM micrograph of crack region. We furthermore performed EDX analysis and found that region a is the Ge substrate, regions b and c are GeO_x , and region d is the epitaxial layer. The crack initiated in the nanoscaled epilayer, possibly induced by in-diffused moisture and part of Ge was oxidized into GeO_x . Both the EL and SEM analysis suggested that the shunt and leakage paths occurred in the edge of cells and resulted in the degradation.

4. Conclusions

We performed accelerated tests on both sealed and bare TJ concentrator solar cells in a damp-heat environment and investigated the degradation of electrical characteristics over time. Our results indicated that silicone encapsulant really protects solar receiver and resists moisture ingress; therefore, the performance of sealed cells is much better than unsealed

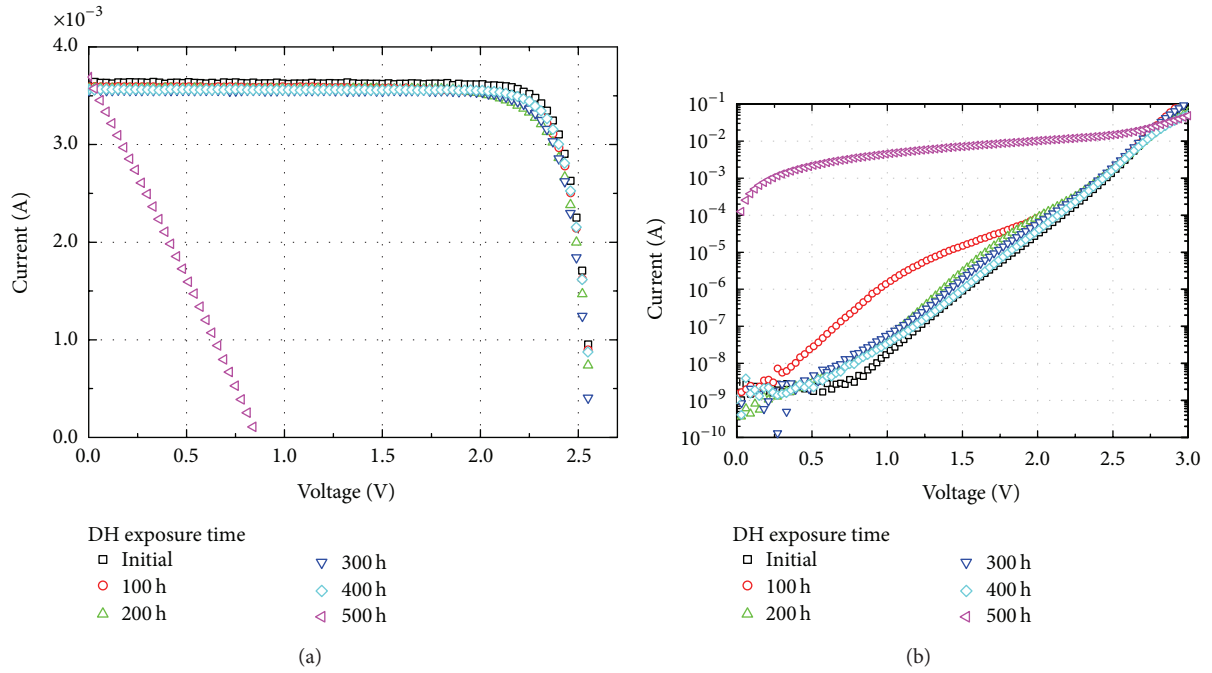


FIGURE 7: (a) Light *I-V* and (b) dark *I-V* curves of bare cell S2 measured sequentially after each step of damp-heat exposures.

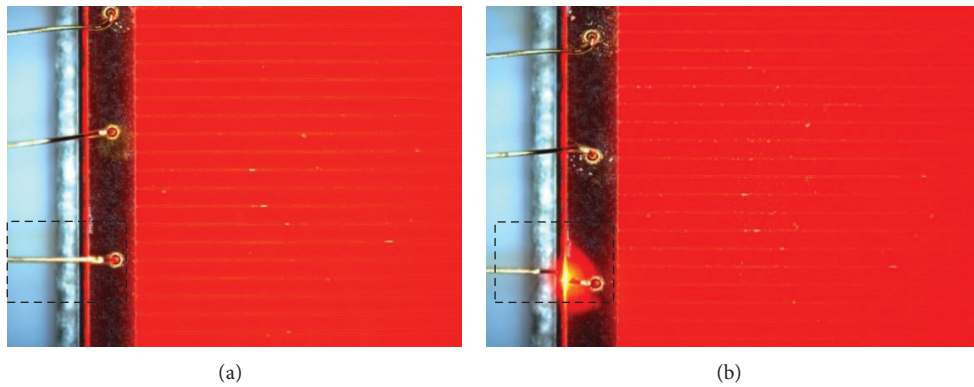


FIGURE 8: EL images of sample S2 after 400 h (a) and 500 h (b) of exposure.

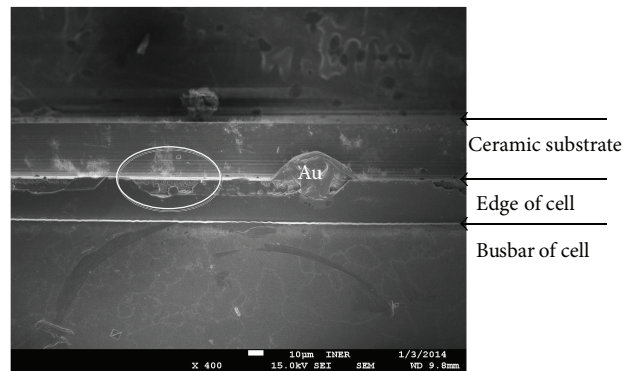


FIGURE 9: Cross-sectional SEM micrograph shows the crack and the Au particle in the edge of nonsealed solar cell.

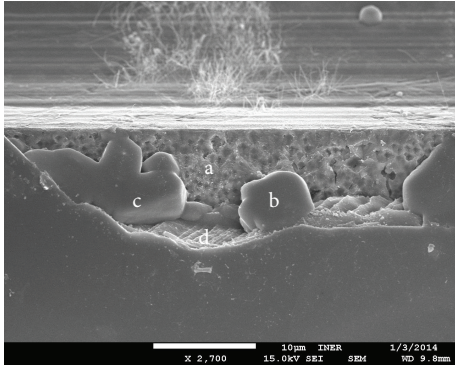


FIGURE 10: Cross-sectional SEM micrograph shows partial crack in the edge of nonsealed solar cell. Region a is the Ge substrate, regions b and c are GeO_x , and region d is the epitaxial layer as analyzed by EDX.

cells. However, careful selection of silicone material should be adopted to avoid the deterioration of silicone from moisture attack and to preserve the reliability. For bare cells, we found that I_{sc} , V_{oc} , and FF and conversion efficiency degraded after long time exposure to damp-heat environment. Both EL and SEM analysis indicated that the causes of degradation can be attributed to the damage and cracks in the edge of cells. The damage and cracks resulted in the leakage paths and increased recombination current. In the near future, we will investigate solar cells with different silicone materials and increase the damp-heat test time in order to clarify the degradation mechanism of silicone-sealed solar cells and to understand the lifetime under the influence of damp-heat environment.

Conflict of Interests

The authors declare that there is no conflict of interests regarding the publication of this paper.

References

- [1] C. M. Fetzer, X. Q. Liu, J. Chang et al., "Progress in large area organometallic vapor phase epitaxy for III-V multijunction photovoltaics," *Journal of Crystal Growth*, vol. 352, no. 1, pp. 181–185, 2011.
- [2] G. J. Bauhuis, P. Mulder, and J. J. Schermer, "Ultra-thin, high performance tunnel junctions for III-V multijunction cells," in *Proceedings of the 38th IEEE Photovoltaic Specialists Conference (PVSC '12)*, pp. 909–912, Austin, Tex, USA, June 2012.
- [3] M. A. Green, K. Emery, Y. Hishikawa, W. Warta, and E. D. Dunlop, "Solar cell efficiency tables (version 42)," *Progress in Photovoltaics*, vol. 21, no. 5, pp. 827–837, 2013.
- [4] J. L. Hou, S. J. Chang, T. J. Hsueh, C. H. Wu, W. Y. Weng, and J. M. Shieh, "InGaP/GaAs/Ge triple-junction solar cells with ZnO nanowires," *Progress in Photovoltaics*, vol. 21, no. 8, pp. 1645–1652, 2013.
- [5] S. P. Philipps, G. Peharz, R. Hoheisel et al., "Energy harvesting efficiency of III-V triple-junction concentrator solar cells under realistic spectral conditions," *Solar Energy Materials and Solar Cells*, vol. 94, no. 5, pp. 869–877, 2010.

- [6] M. Yamaguchi, T. Takamoto, A. Khan, M. Imaizumi, S. Matsuda, and N. J. Ekins-Daukes, "Super-high-efficiency multi-junction solar cells," *Progress in Photovoltaics*, vol. 13, no. 2, pp. 125–132, 2005.
- [7] C. G. Zimmermann, C. Noemayr, M. Kolb, and A. Rucki, "A mechanism of solar cell degradation in high intensity, high temperature space missions," *Progress in Photovoltaics*, vol. 21, no. 4, pp. 420–435, 2013.
- [8] R. R. King, D. C. Law, C. M. Fetzer et al., "40% efficient metamorphic GaInP/GaInAs/Ge multijunction solar cells," *Applied Physics Letters*, vol. 90, no. 18, Article ID 183516, 2007.
- [9] 2013, <http://sharp-world.com/corporate/news/130614.html>.
- [10] J. H. Ermer, R. K. Jones, P. Hebert et al., "Status of C3MJ+ and C4MJ production concentrator solar cells at spectrolab," *IEEE Journal of Photovoltaics*, vol. 2, no. 2, pp. 209–213, 2012.
- [11] F. Dimroth, W. Guter, J. Schöne et al., "Metamorphic GaInP/GaInAs/Ge triple-junction solar cells with $\gg 41\%$ efficiency," in *Proceedings of the 34th IEEE Photovoltaic Specialists Conference (PVSC '09)*, pp. 001038–001042, Philadelphia, Pa, USA, June 2009.
- [12] W. Guter, J. Schöne, S. P. Philipps et al., "Current-matched triple-junction solar cell reaching 41.1% conversion efficiency under concentrated sunlight," *Applied Physics Letters*, vol. 94, no. 22, Article ID 223504, 3 pages, 2009.
- [13] G. S. Kinsey, P. Pien, P. Hebert, and R. A. Sherif, "Operating characteristics of multijunction solar cells," *Solar Energy Materials and Solar Cells*, vol. 93, no. 6–7, pp. 950–951, 2009.
- [14] I. Rey-Stolle and C. Algora, "High-irradiance degradation tests on concentrator GaAs solar cells," *Progress in Photovoltaics*, vol. 11, no. 4, pp. 249–254, 2003.
- [15] P. Espinet, C. Algora, J. R. González, N. Núñez, and M. Vázquez, "Degradation mechanism analysis in temperature stress tests on III-V ultra-high concentrator solar cells using a 3D distributed model," *Microelectronics Reliability*, vol. 50, no. 9–11, pp. 1875–1879, 2010.
- [16] J. R. González, M. Vázquez, N. Núñez, C. Algora, I. Rey-Stolle, and B. Galiana, "Reliability analysis of temperature step-stress tests on III-V high concentrator solar cells," *Microelectronics Reliability*, vol. 49, no. 7, pp. 673–680, 2009.
- [17] N. Núñez, M. Vázquez, J. R. González, C. Algora, and P. Espinet, "Novel accelerated testing method for III-V concentrator solar cells," *Microelectronics Reliability*, vol. 50, no. 9–11, pp. 1880–1883, 2010.
- [18] J. Nelson, *The Physics of Solar Cells*, Imperial College Press, London, UK, 2002.
- [19] O. Ueda, "Reliability issues in III-V compound semiconductor devices: optical devices and GaAs-based HBTs," *Microelectronics Reliability*, vol. 39, no. 12, pp. 1839–1855, 1999.
- [20] K. R. McIntosh, N. E. Powell, A. W. Norris, J. N. Cotsell, and B. M. Ketola, "The effect of damp-heat and UV aging tests on the optical properties of silicone and EVA encapsulants," *Progress in Photovoltaics*, vol. 19, no. 3, pp. 294–300, 2011.
- [21] M. Langenkamp and O. Breitenstein, "Classification of shunting mechanisms in crystalline silicon solar cells," *Solar Energy Materials and Solar Cells*, vol. 72, no. 1–4, pp. 433–440, 2002.

Research Article

Terahertz Performance of a GaN-Based Planar Nanochannel Device

K. Y. Xu,¹ Y. N. Wang,¹ C. J. Zheng,¹ J. W. Xiong,¹ and G. Wang²

¹Laboratory of Quantum Engineering and Quantum Materials, School of Physics and Telecommunication Engineering, South China Normal University, Guangzhou 510006, China

²State Key Laboratory of Optoelectronic Materials and Technologies, Sun Yat-sen University, Guangzhou 510275, China

Correspondence should be addressed to K. Y. Xu; xuky@scnu.edu.cn and G. Wang; stswang@mail.sysu.edu.cn

Received 13 January 2014; Revised 16 March 2014; Accepted 25 March 2014; Published 10 April 2014

Academic Editor: Sheng-Po Chang

Copyright © 2014 K. Y. Xu et al. This is an open access article distributed under the Creative Commons Attribution License, which permits unrestricted use, distribution, and reproduction in any medium, provided the original work is properly cited.

Using a combined two-dimensional-three-dimensional (2D-3D) ensemble Monte Carlo (EMC) model, the performance of a planar nanochannel device is studied at the terahertz (THz) region. The device is based on a GaN/AlGa_N heterostructure in which a two-dimensional electron gas (2DEG) forms at the interface. Simulation results reveal that, at low working frequencies, the performance of the device is almost frequency independent. However, when the working frequency is higher than 0.5 THz, obvious enhancements in the device performance have been observed. The enhancements are characterized by two resonant peaks at frequencies of about 4 THz and 8 THz. Also, the frequency-dependent performance exhibits nonmonotonicity. Further studies show that the performance enhancements can be attributed to the excitations of 2D plasma waves in the device, with the emergence of the above resonant peaks corresponding to the formation of standing plasma waves. Moreover, simulation results show that the device performance increases monotonically with signal amplitude, when the device is unbiased. However, when a DC bias is applied, the performance remains almost unchanged for large signals but is significantly enhanced for small signals. Therefore, the device performance shows a strong nonmonotonic dependence on signal amplitude, and its minimal value occurs when the signal amplitude is only about $\sqrt{2}$ times the DC bias.

1. Introduction

In the past few decades, continuous miniaturization of semiconductor devices has led to high-speed operations and large-scale integration of electronics. A single silicon chip can now contain more than a billion transistors and operate at frequencies higher than 1 GHz. The operation frequency can be further increased by utilizing a planar architecture. In planar devices, electrodes are connected to the sides of the active semiconductor layer, rather than being placed on its top and bottom surface, as in conventional multilayered vertical-structured devices. As a result, very low parasitic capacitances are obtainable, leading to very high operating speeds. Planar nanodevices based on 2DEGs in semiconductor heterostructures have been demonstrated to operate at tens of GHz or more [1–3]. In particular, self-switching diodes (SSDs) have been shown to possess zero threshold voltages and be able to work as high-frequency detectors. At room

temperature, they can operate at frequencies up to 1.5 THz [4] at room temperature and up to 2.5 THz [5] at a temperature of 150 K.

Apart from improving the operational frequency of the devices, planar architecture can also lead to some additional mechanisms. It has been shown that when the thickness of the conducting layer is lower than 10 nm, 2D plasmonic noise is dominant, resulting in a geometric dependence of noise characteristics [6]. Moreover, it has been proved that in a submicron field-effect transistor (FET) with asymmetric boundary conditions, 2D plasma waves can be excited simply by a DC current [7]. This discovery has prompted intensive investigations of nanometer FETs as THz sources and detectors, resulting in substantial progress in this field [8–13].

The physics of plasma wave based collective electron transport is vastly different from conventional individual (uncorrelated) electron transport. However, the studies so far have been mostly limited to plasma waves occurring

in submicron FET structures. In this study, based on a combined 2D-3D EMC model [14], we will focus on the role of 2D plasma waves in improving the THz performance of a two-terminal nanometer device. The paper is structured as follows. In Section 2, the structure of the device is first introduced and then the combined 2D-3D EMC model is concisely described. In Section 3, the frequency-dependent performance of the device is studied under various conditions, and the plasma related features are analysed in detail. In Section 4, the conclusions of this work are presented.

2. Device Structure and Numerical Model

Figures 1(a) and 1(b) schematically show the top view and cross section of a nanochannel device. The device is based on a GaN/AlGaN heterostructure, in which a 2DEG is formed at the GaN/AlGaN interface with a carrier concentration of $8.0 \times 10^{12} \text{ cm}^{-2}$ [15]. The two insulating trenches (rectangular grey areas in Figure 1(a)) are created by etching through the 2DEG layer. Therefore, electrons have to pass through the narrow channel between the two trenches in order to conduct current from the left electron reservoir to the right one. It is evident that while the device performance at low frequencies might be trivial, at the THz region, it would be quite complex because additional phenomena, such as plasma waves, would be dominant.

In this work, we employed a combined 2D-3D EMC model based on a semiclassical 2D EMC method self-consistently coupled with 3D Poisson equations. This combined model is developed from our entirely 2D model, which has been successfully applied in earlier studies [16, 17]. It is noteworthy that a fully 3D EMC model has been developed to study three-terminal T-branch junctions (TBJs) with a top gate terminal [18, 19]. Despite minimizing the need for parameter fitting and including the effect of electron transfers from the channel to other layers, the 3D model leads to almost the same results as those obtained from an entirely 2D model for GaAs-based devices [20]. There are two reasons for the above agreement between an entirely 2D model and a 3D model. The first is that the operating properties of TBJs are mainly determined by the 2DEG layer, which can be well described by an entirely 2D model. The other is that an artificially introduced side gate in the 2DEG layer can serve the function of TBJs' top gate. If the top gate cannot be modelled as a side gate, at least a combined 2D-3D model is needed.

As in an entirely 2D model, all the electrons in the combined model are assumed to be confined within the 2DEG layer. This means that the effect of electron transfers from the channel to other layers is ignored. As such, the 2D EMC method is sufficient to describe the microscopic behaviour of electrons in devices. However, the main advantage of the combined model lies in upgrading the 2D Poisson solver in the entirely 2D model to a 3D Poisson solver. This would enable the proper inclusion of electric-field couplings beyond the 2DEG layer, which can lead to the appearance of 2D plasma waves. In order to sufficiently include the 3D electric-field couplings, Poisson equations should be solved in a domain beyond the device's realistic structure. As shown

in Figure 1(b), the GaN substrate and a region (air) above the device surface, both of height $1 \mu\text{m}$, were included in the simulations. Insulating trenches were assumed to have vertical sidewalls. Moreover, the depth of all the insulating trenches was assumed to be 1030 nm. This uniform-depth treatment can avoid the trench-depth effect [14]. Dielectric constants used in the simulations for Air, AlGa_N, and GaN were 1, 8.5, and 8.9, respectively. For convenience, the effect of surface states at the semiconductor-air interface was included by a simple constant charge model with negative charge density, $N_S = -0.8 \times 10^{12} \text{ cm}^{-2}$ [21]. Of course, the use of an advanced surface charge model, such as the self-consistent charge model, would result in more accurate results, but it is time consuming, and the results have no qualitative difference [22]. Geometric parameters used in the simulations can be found in Figure 1(a). All simulations were performed at room temperature with the left terminal grounded. The Poisson equations were solved in $5 \text{ nm} \times 5 \text{ nm}$ meshes with a time step of 1 fs. More information about the model can be found in our recent work [14, 23].

3. Simulation Results and Analysis

Figure 2 shows the frequency-dependent performance of the device shown in Figure 1. In the simulations, the right terminal was biased with different DC voltages of $V_{\text{DC}} = 2.0 \text{ V}$ (red curve), 1.5 V (green curve), 1.0 V (navy blue curve), 0.5 V (pink curve), and 0.0 V (powder-blue curve). Then, a sinusoidal signal with an amplitude of $V_{\text{AC}} = 0.5 \text{ V}$ was also applied, and the AC current I_{AC} through the nanochannel was recorded. For ease of comparison, all the data were normalized to those obtained at the lowest simulated frequency, that is, 0.1 THz. We find that the performance of the device biased with a voltage of 1.0 V remains unchanged at low frequency, while showing obvious enhancement (i.e., the normalized amplitude of I_{AC} is larger than 1) when the frequency is higher than 0.5 THz. The normalized amplitude increases with frequency and reaches its first maximal value at a frequency of about 4 THz. Subsequently, it dramatically reduces to a minimum at a frequency of about 6.7 THz and then increases again to reach the second maximal value at a frequency of about 8 THz. Similar trends are observed for devices with higher DC bias (i.e., $V_{\text{DC}} = 1.5 \text{ V}$ and 2.0 V). Moreover, results show that the enhancement is higher when a higher DC bias is applied. For example, the performance of the device at a DC bias of 2.0 V can be enhanced to more than 2.5 times that at low frequencies (see the red curve in Figure 2). This happens at a frequency of about 4 THz, at which a maximum power of about $10 \mu\text{W}$ can be reached. However, for the device with smaller DC bias (i.e., $V_{\text{DC}} = 0.5 \text{ V}$ and 0.0 V), no enhancement is observed, and the normalized amplitude monotonically reduces with frequency, as shown by the pink and powder-blue curves in Figure 2.

In order to identify the origin of the above performance enhancements, efforts are devoted to compare nonenhanced results obtained at a low frequency of 0.1 THz with the enhanced ones obtained at a high frequency of 4.0 THz. During simulations, the time-dependent 2D-current-distribution

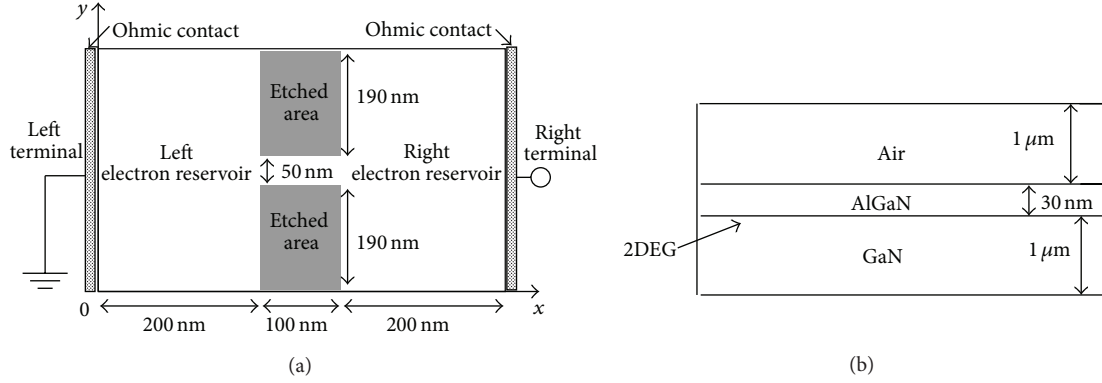


FIGURE 1: Schematic top view (a) and side view (b) of the simulated nanochannel device (not to scale). The grey areas and the white area in the top view represent insulating trenches and the 2DEG, respectively. A GaN/AlGaIn interface is only 30 nm below the device surface, at which a sheet of 2DEG forms. In the simulations, all the insulating trenches are assumed to have vertical sidewalls and pass through the whole GaN/AlGaIn heterostructure.

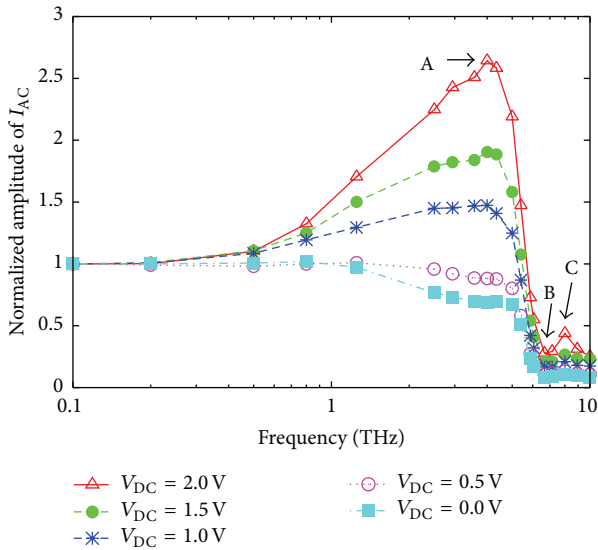


FIGURE 2: Frequency-dependent output-signal amplitude of the nanochannel device shown in Figure 1 when different DC voltages are applied (during all simulations, the input-signal amplitude was set to 0.5 V).

$I(t, X, Y)$ in the entire device (including the channel and the two reservoirs) was recorded. Then, the recorded currents were summed along the Y direction to obtain a time-dependent 1D-current-distribution $I(t, X)$ in the X direction. Here, t is the time, the X direction is parallel to the channel, and the Y direction is perpendicular to the channel, as shown in Figure 1. Results obtained at 0.1 THz and at 4.0 THz are shown in Figures 3(a) and 3(b), respectively. We find from Figure 3(a) that the low-frequency current distribution along the X direction is uniform during the entire working period (i.e., the period of the applied signal) and synchronously changes with the applied signal. In contrast, the high-frequency results are quite nonuniform, because standing waves have formed in both reservoirs, as shown in

Figure 3(b). The emergence of standing waves in the device strongly suggests a possibility of plasma-wave excitations. The dispersion relations for 2D plasma waves are given by [6]

$$f = \frac{1}{2\pi} \sqrt{\frac{e^2 n^{2D} k}{m_0 m \epsilon_0 \epsilon_{\text{eff}}}}, \quad (1)$$

where f and k are the frequency and wave vector, respectively; e is the electron charge; $n^{2D} = 8 \times 10^{12} \text{ cm}^{-2}$ is the 2D carrier concentration; m_0 and m are the free and effective electron masses; ϵ_0 is the vacuum dielectric permittivity; and ϵ_{eff} is the effective dielectric constant, which is defined as [24]

$$\epsilon_{\text{eff}} = \frac{1}{2} \left[\epsilon_2 + \epsilon_1 \frac{1 + \epsilon_1 \tanh(kd)}{\epsilon_1 + \tanh(kd)} \right]. \quad (2)$$

In our case, $\epsilon_1 = 8.5$ is the dielectric constant of AlGaIn, $\epsilon_2 = 8.9$ is the dielectric constant of GaN, and $d = 30 \text{ nm}$ is the thickness of the AlGaIn layer. The standing wave conditions in the reservoirs are given by

$$k = \frac{\pi(2n-1)}{2L}, \quad (3)$$

where $n = 1, 2, 3 \dots$ and $L = 200 \text{ nm}$ is the length of reservoirs. Substituting (2) and (3) into (1) and using the parameters provided above, one can observe that the frequency of standing waves is 4.5 THz, 7.1 THz, and 8.5 THz for $n = 1, 2$, and 3, respectively. Since damping effects (e.g., phonon scatterings) are not included in (1), analytic results obtained from (1)–(3) are expected to be higher than those obtained from the simulation. By making a comparison, one can find that each analytically obtained frequency is only a little higher than the frequency at special points A, B, and C shown in Figure 2. This confirms that the enhancement of device performance in the THz region is because of the excitations of 2D plasma waves. Moreover, the formation of standing plasma waves in the reservoirs is attributed to the performance peaks (special points A and C) shown in Figure 2. However, according to the analytic results, a peak,

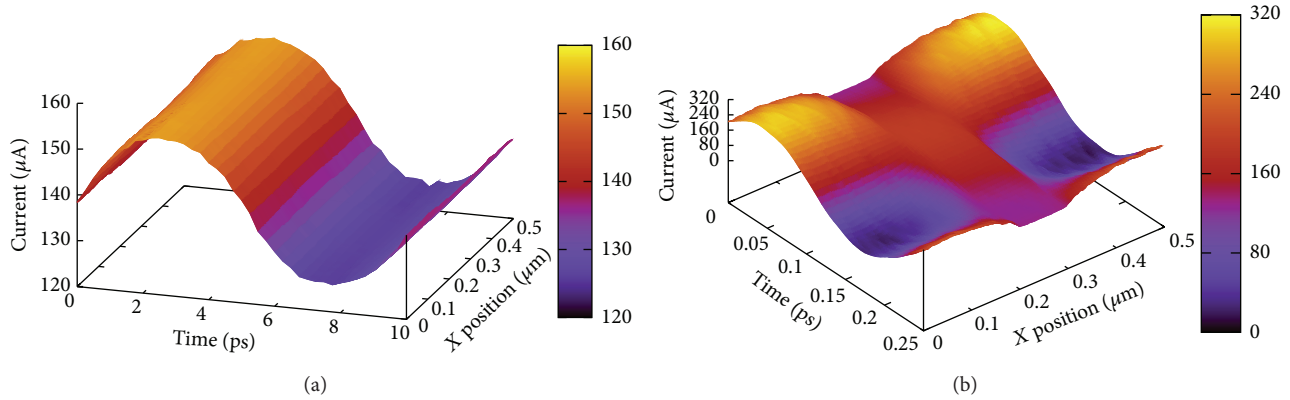


FIGURE 3: Time-dependent current distributions along the X direction (defined in Figure 1(a)) for the device operating at the frequencies of 0.1 THz (a) and 4.0 THz (b).

rather than a valley, should emerge at point B. To ascertain the reason for this anomaly, (1) was utilized to calculate the phase delay occurring in the plasma waves as they passed through the nanochannel. Considering that the electron density in the nanochannel is reduced by the surface states to about 75% of that in the reservoirs, a phase delay of π can be obtained. Because of this π -phase delay, the standing waves in the two reservoirs have opposite effects on the device performance. As a result, the resonant peak at point B disappears. From this calculation, we also find that the power-delay product for the device is frequency dependent.

It is well known that the length of electron reservoirs has negligible influence on the performance of traditional devices. However, as we have shown above, this is not true for nanodevices operating at the THz region, especially when the electron reservoir is low dimensional. Fortunately, the length of electron reservoirs can now be precisely defined by modern methods used in nanotechnology [25].

To further understand the influence of plasma waves on the device performance, signals with the same frequency of 4.0 THz but with different amplitudes were applied on the device under different DC biases. Simulation results are shown in Figure 4. We find that when the device is unbiased, the device performance shows a nearly linear increase with the amplitude of the applied signals. When DC bias is applied, the device performance for small signals is significantly enhanced, but that for large signals is nearly constant. The performance reduces with the amplitude of the applied signals and then reaches a minimal value before increasing in a manner similar to the unbiased case. The performance enhancement induced by the DC bias implies that plasma waves are easier to be excited on a DC flow. Furthermore, we can find from Figure 4 that the applied signal's amplitudes (DC biases) at the minimal performance points are about 0.4 V (0.3 V), 0.7 V (0.5 V), 1.1 V (0.8 V), and 1.4 V (1.0 V). It is interesting to see that, at these minimal points, the amplitude of each applied signal is only about $\sqrt{2}$ times the corresponding DC bias. Because the amplitude of a sinusoidal signal is also $\sqrt{2}$ times its time-averaged value over every semiperiod, one can expect that the time-averaged

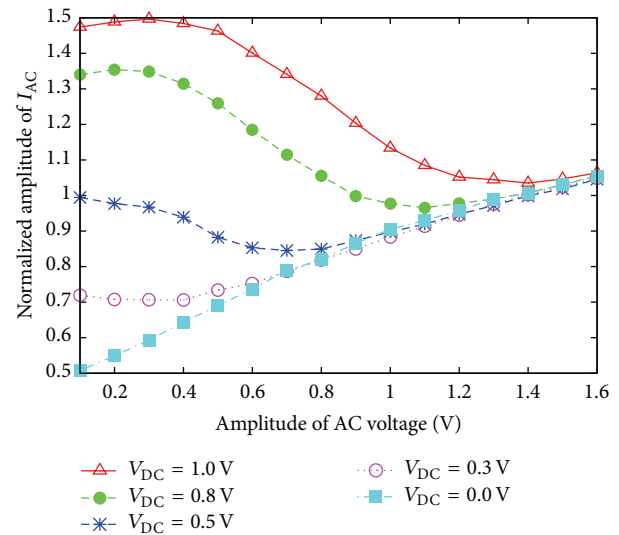


FIGURE 4: Current response of the nanochannel versus the amplitude of applied signal with a frequency of 4.0 THz, under different DC voltages of 1.0 V (red curve), 0.8 V (green curve), 0.5 V (navy blue curve), 0.3 V (pink curve), and 0.0 V (powder-blue curve).

electric-field should be zero in the device at the negative semiperiod of applied signals. This means that the effect of the DC bias is cancelled when the amplitude of the applied signal is larger than $\sqrt{2}$ times the DC bias; therefore, the device functions as one without any DC bias.

4. Conclusion

In this paper, we have employed a combined 2D-3D EMC model to analyse the THz performances of a GaN-based planar nanochannel device under different conditions. We observed that the performance of the device at frequencies higher than 0.5 THz is strongly enhanced by 2D plasma waves. The resonances of the 2D plasma waves with the device structure result in two performance peaks at frequencies of

about 4 THz and 8 THz, respectively. This resonant feature may be applied for frequency selection in RF circuits or THz systems. Moreover, the application of a DC bias allows for small signals to excite 2D plasma waves easier, resulting in a significant enhancement of the device performance. However, when the applied-signal amplitude is larger than $\sqrt{2}$ times the DC bias, the device operates as one without any DC bias.

Conflict of Interests

The authors declare that there is no conflict of interests regarding the publication of this paper.

Acknowledgments

This work was supported by Natural Science Foundation of Guangdong Province, China (no. S2013010012711), NSFC (nos. 11374185, 61072029), and FOK YING TONG Education Foundation (no. 122004). The authors also thank the high-performance computing platform of South China Normal University for technical support.

References

- [1] I. Bisotto, E. S. Kannan, S. Sassine et al., “Microwave based nanogenerator using the ratchet effect in Si/SiGe heterostructures,” *Nanotechnology*, vol. 22, no. 24, Article ID 245401, 2011.
- [2] H. Irie and R. Sobolewski, “Terahertz electrical response of nanoscale three-branch junctions,” *Journal of Applied Physics*, vol. 107, no. 8, Article ID 084315, 2010.
- [3] I. Íñiguez-de-la-Torre, S. Purohit, V. Kaushal et al., “Exploring digital logic design using ballistic deflection transistors through monte carlo simulations,” *IEEE Transactions on Nanotechnology*, vol. 10, no. 6, pp. 1337–1346, 2011.
- [4] C. Balocco, S. R. Kasjoo, X. F. Lu et al., “Room-temperature operation of a unipolar nanodiode at Terahertz frequencies,” *Applied Physics Letters*, vol. 98, no. 22, Article ID 223501, 2011.
- [5] C. Balocco, M. Halsall, N. Q. Vinh, and A. M. Song, “THz operation of asymmetric-nanochannel devices,” *Journal of Physics Condensed Matter*, vol. 20, no. 38, Article ID 384203, 2008.
- [6] J.-F. Millithaler, L. Reggiani, J. Pousset et al., “A Monte Carlo investigation of plasmonic noise in nanometric n-In_{0.53}Ga_{0.47}As channels,” *Journal of Statistical Mechanics: Theory and Experiment*, vol. 2009, no. 1, Article ID P01040, 2009.
- [7] M. Dyakonov and M. Shur, “Shallow water analogy for a ballistic field effect transistor: new mechanism of plasma wave generation by dc current,” *Physical Review Letters*, vol. 71, no. 15, pp. 2465–2468, 1993.
- [8] A. El Fatimy, N. Dyakonova, Y. Meziani et al., “AlGa_N/Ga_N high electron mobility transistors as a voltage-tunable room temperature Terahertz sources,” *Journal of Applied Physics*, vol. 107, no. 2, Article ID 024504, 2010.
- [9] V. Yu. Kachorovskii and M. S. Shur, “Current-induced Terahertz oscillations in plasmonic crystal,” *Applied Physics Letters*, vol. 100, no. 23, Article ID 232108, 2012.
- [10] T. Nagatsuma, “Terahertz technologies: present and future,” *IEICE Electronics Express*, vol. 8, no. 14, pp. 1127–1142, 2011.
- [11] Y. Chen, J. He, H. L. Liang et al., “Model-based prediction of the plasma oscillation excitation response characteristics of a high-electron mobility transistor-based Terahertz photomixer with the cap region,” *Journal of Computational and Theoretical Nanoscience*, vol. 9, no. 4, pp. 549–554, 2012.
- [12] L. Wang, W. Hu, J. Wang et al., “Plasmon resonant excitation in grating-gated AlN barrier transistors at Terahertz frequency,” *Applied Physics Letters*, vol. 100, no. 12, Article ID 123501, 2012.
- [13] Y. Zhou, J. Sun, Y. Sun et al., “Characterization of a room temperature Terahertz detector based on a GaN/AlGa_N HEMT,” *Journal of Semiconductors*, vol. 32, no. 6, Article ID 064005, 2011.
- [14] K. Y. Xu, J. W. Xiong, A. M. Song, and G. Wang, “Effects of three-dimensional electric-field coupling on a side-gated nanotransistor,” *Semiconductor Science and Technology*, vol. 26, no. 9, Article ID 095026, 2011.
- [15] I. Íñiguez-de-la-Torre, J. Mateos, D. Pardo, A. M. Song, and T. González, “Noise and Terahertz rectification linked by geometry in planar asymmetric nanodiodes,” *Applied Physics Letters*, vol. 94, no. 9, Article ID 093512, 2009.
- [16] K. Y. Xu, X. F. Lu, G. Wang, and A. M. Song, “Strong spatial dependence of electron velocity, density, and intervalley scattering in an asymmetric nanodevice in the nonlinear transport regime,” *IEEE Transactions on Nanotechnology*, vol. 7, no. 4, pp. 451–457, 2008.
- [17] K. Y. Xu, G. Wang, and A. M. Song, “Gunn oscillations in a self-switching nanodiode,” *Applied Physics Letters*, vol. 93, no. 23, Article ID 233506, 2008.
- [18] T. Sadi, F. Dessenne, and J.-L. Thobel, “Three-dimensional Monte Carlo study of three-terminal junctions based on InGaAs/InAlAs heterostructures,” *Journal of Applied Physics*, vol. 105, no. 5, Article ID 053707, 2009.
- [19] T. Sadi and J.-L. Thobel, “Analysis of the high-frequency performance of InGaAs/InAlAs nanojunctions using a three-dimensional Monte Carlo simulator,” *Journal of Applied Physics*, vol. 106, no. 8, Article ID 083709, 2009.
- [20] I. Íñiguez-de-la-Torre, T. González, D. Pardo et al., “Three-terminal junctions operating as mixers, frequency doublers and detectors: a broad-band frequency numerical and experimental study at room temperature,” *Semiconductor Science and Technology*, vol. 25, no. 12, Article ID 125013, 2010.
- [21] A. Íñiguez-de-la-Torre, I. Íñiguez-de-la-Torre, J. Mateos et al., “Searching for THz Gunn oscillations in Ga_N planar nanodiodes,” *Journal of Applied Physics*, vol. 111, no. 11, Article ID 113705, 2012.
- [22] J.-F. Millithaler, I. Íñiguez-de-la-Torre, A. Íñiguez-de-la-Torre et al., “Optimized V-shape design of Ga_N nanodiodes for the generation of Gunn oscillations,” *Applied Physics Letters*, vol. 104, no. 7, Article ID 073509, 2014.
- [23] K. Y. Xu, Z. N. Wang, Y. N. Wang, J. W. Xiong, and G. Wang, “Influence of electric field coupling model on the simulated performances of a Ga_N based planar nanodevice,” *Journal of Nanomaterials*, vol. 2013, Article ID 124354, 7 pages, 2013.
- [24] M. Shur, “Plasma wave Terahertz electronics,” *Electronics Letters*, vol. 46, no. 26, pp. S18–S21, 2010.
- [25] A. Khalid, C. Li, V. Papageorgiou et al., “In_{0.53}Ga_{0.47}As planar Gunn diodes operating at a fundamental frequency of 164 GHz,” *IEEE Electron Devices Letters*, vol. 34, no. 1, pp. 39–41, 2013.

Research Article

Microstructures and Recording Mechanism of Mo/Si Bilayer Applied for Write-Once Blue Laser Optical Recording

Sin-Liang Ou,¹ Kuo-Sheng Kao,² Han-Feng Chang,³ Tsung-Shine Ko,⁴ and Chin-Yen Yeh³

¹ Department of Materials Science and Engineering, National Taiwan University, Taipei 106, Taiwan

² Department of Computer and Communication, SHU-TE University, Kaohsiung 824, Taiwan

³ CMC Magnetics Corporation, Taoyuan 333, Taiwan

⁴ Department of Electronic Engineering, National Changhua University of Education, Changhua 500, Taiwan

Correspondence should be addressed to Sin-Liang Ou; odibear@gmail.com

Received 14 December 2013; Revised 22 February 2014; Accepted 24 February 2014; Published 7 April 2014

Academic Editor: Sheng-Po Chang

Copyright © 2014 Sin-Liang Ou et al. This is an open access article distributed under the Creative Commons Attribution License, which permits unrestricted use, distribution, and reproduction in any medium, provided the original work is properly cited.

Mo/Si bilayer thin films were grown by magnetron sputtering and applied to write-once blu-ray disc (BD-R). The microstructures and optical storage properties of Mo/Si bilayer were investigated. From the temperature dependence of reflectivity measurement, it was revealed that a phase change occurred in the range of 255–425°C. Transmission electron microscopy analysis showed that the as-deposited film possessed Mo polycrystalline phase. The hexagonal Mo₃Si₂ and cubic Mo₃Si phases appeared after annealing at 300 and 450°C, respectively. By measuring the optical reflectivity at a wavelength of 405 nm, the optical contrast of Mo/Si bilayer between as-deposited and 450°C-annealed states was evaluated to 25.8%. The optimum jitter value of 6.8% was obtained at 10.65 mW for 4× recording speed. The dynamic tests show that the Mo/Si bilayer has high potential in BD-R applications.

1. Introduction

For write-once blu-ray disc (BD-R), amorphous silicon (a-Si) was used as a recording layer due to its advantages of low cost and easy fabrication process. However, the high crystallization temperature of 700°C for a-Si is a serious shortcoming, leading to a high writing power in the recording characteristics. It is well known that metal induced crystallization (MIC) can be applied to decrease the crystallization temperature of a-Si by introducing various metals [1–5]. Therefore, several metal/a-Si bilayer structures such as Cu/Si [6], Al/Si [7], Ni/Si [8], and Cu-Al/Si [9] have been proposed as the recording films of BD-R.

It has been reported that the crystallization temperature of a-Si in Mo/Si multilayer films was ranging from 200 to 400°C [10], indicating that the Mo/Si based films could be suitable for BD-R. Actually, Mo/Si structured mirrors have been widely studied for applications in extreme ultraviolet lithography because of their high normal incidence reflectance [11–15]. Nevertheless, it has not been found that the Mo/Si based thin films were applied to optical recording

media. In this study, we presented the Mo (7 nm)/Si (7 nm) bilayer as the recording film of BD-R. The crystallization temperature, microstructures, and recording characteristics of this bilayer were analyzed and discussed.

2. Experimental Procedure

The Mo (7 nm)/Si (7 nm) bilayer was grown on nature oxidized Si wafers and polycarbonate (PC) substrates at room temperature by magnetron sputtering using the Mo and Si targets. In order to apply the Mo/Si bilayer to write-once optical recording media, the multilayer of Ag reflective layer (95 nm)/ZnS-SiO₂ (35 nm)/Mo (7 nm)/Si (7 nm)/ZnS-SiO₂ (24 nm) was fabricated on 1.1 mm-thick PC substrate which has a track pitch of 0.32 μm. Afterwards, a PC transparent cover layer with 0.1 mm thickness was covered on the top of these layers by spin-coating. The crystallization temperature of as-deposited specimen was measured by a home-made reflectivity-temperature analyzer. The microstructures and crystal orientations of the samples before and after annealing

TABLE 1: Dynamic test conditions.

User capacity	25 GB
Thickness of substrate	1.1 mm
Wavelength	405 nm
Numerical aperture (N.A.)	0.85
Modulation code	(1, 7) RLL
Track pitch	0.32 μm
Linear velocity	4.92 m/s (1 \times), 19.68 m/s (4 \times)
Recording format	On groove

were characterized by transmission electron microscopy (TEM). Relationship between reflectivity and wavelength was measured by means of a UV-VIS-NIR spectrophotometer (Perkin-Elmer Lambda 900). To study the diffusion characteristic of Mo/Si bilayer, the element concentration depth profiles of the as-deposited and annealed samples were analyzed using Auger electron spectrometer (AES). The recording characteristics of the discs were evaluated by a dynamic tester (ODU-1000, PULSTEC), and the testing conditions were shown in Table 1. The wavelength of the laser beam is 405 nm and the numerical aperture (N.A.) of the objective lens is 0.85. The modulation code is (1, 7) RLL. The linear velocities of 1 \times and 4 \times recording speeds are 4.92 and 19.68 m/s, respectively.

3. Results and Discussion

Figure 1 exhibits the reflectivity changes as a function of temperature for the Mo/Si bilayer at a heating rate of 20 $^{\circ}\text{C}/\text{min}$. The measured temperature was increased from room temperature to 550 $^{\circ}\text{C}$ using a resistive heater. It can be found that the reflectivity has a decrease as the temperature heated from 255 to 425 $^{\circ}\text{C}$. According to previous research, as the films undergo a structural transition, it could lead to the change of optical reflectivity [16]. Therefore, we choose the temperatures of 300 and 450 $^{\circ}\text{C}$ to perform the annealing experiments and examine the microstructures of these films.

The TEM bright field image and electron diffraction pattern of the as-deposited Mo/Si bilayer are shown in Figure 2. It reveals that the as-deposited film has Mo polycrystalline phase with the grain size of 5 nm, and the diffraction pattern rings are identified to Mo (110), Mo (200), and Mo (211). After annealing at 300 $^{\circ}\text{C}$ for 15 min, the grain size of Mo/Si bilayer was enlarged and the hexagonal MoSi₂ phase (h-MoSi₂) appeared, as shown in Figure 3. It is noted that the formation of Mo silicide in Mo/Si multilayers is attributed to the interdiffusion of Mo and Si atoms [17]. As the annealing temperature was increased to 450 $^{\circ}\text{C}$ for 15 min, we found that the grains can be divided into two parts, that is, the smaller grains (red circle) and larger grains with the size about 100–300 nm, as shown in Figure 4(a). The analysis of electron diffraction pattern also indicated that two phases existed in the film, one was h-MoSi₂ and the other was determined to be Mo₃Si phase. The h-MoSi₂ phase with continuous and clear diffraction rings were contributed from the small grains. On the other hand, the discontinuous rings

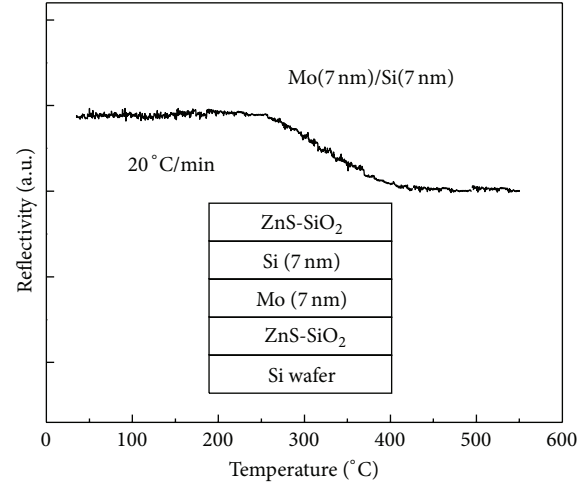


FIGURE 1: Relationship between the reflectivity and temperature of the as-deposited Mo/Si bilayer at a heating rate of 20 $^{\circ}\text{C}/\text{min}$.

corresponding to Mo₃Si phase could result from the large grains. Mo₃Si phase has the cubic A15 structure such as β -W and Cr₃Si [18]. This structure consists of Si atoms occupied the body centered cubic (bcc) positions in the unit cell and the Mo atoms form three orthogonal chains located in the [100] directions on the cube faces. To check the structure of the large grains precisely, the grain which was marked by red arrow was selected to examine by selected area electron diffraction (SAED) pattern. It shows that the large grain has Mo₃Si phase with [011] zone axis, as shown in Figure 4(b). Some reports indicated that the crystallization Si formed in the Mo/Si multilayer after annealing. However, there is no formation of crystallization Si in our results. Murarka et al. [19] have shown the relationship between Mo/Si atomic ratio and the formation in Mo-Si thin films. While the Mo/Si atomic ratio in the film was greater than 0.5, it revealed that only the Mo silicide including MoSi₂, Mo₃Si, and Mo₃Si₂ can be observed after annealing. On the contrary, both the Mo silicide and Si crystallization appeared after annealing as the Mo/Si atomic ratio was less than 0.5. Consequently, the atomic ratio of Mo to Si in the interdiffused region of our annealed Mo/Si bilayer was probably greater than 0.5. As we calculated, the number of Mo atoms in the Mo/Si bilayer with the thickness ratio of 1:1 was about ten times larger than that of Si atoms. As a result, no crystallized Si formed in the annealed film could be ascribed to the excessive Mo atoms in the Mo/Si bilayer. It suggested that the thickness of Mo layer should be reduced, and the Si crystallization could appear after annealing. Interestingly, we found that the large grains with Mo₃Si phase had radial distribution in the film as the TEM magnification was decreased, as shown in Figure 4(c). As mentioned above, the Mo silicide consisting of MoSi₂, Mo₃Si, and Mo₃Si₂ could appear in this study. However, there was no formation of Mo₃Si₂ phase in the annealed sample. In previous researches [20, 21], the activation energies of MoSi₂ and Mo₃Si were estimated to be 204 and 223 kJ/mol, respectively, which were close to each other. Thus, in this study, MoSi₂ and Mo₃Si phases were formed sequentially.

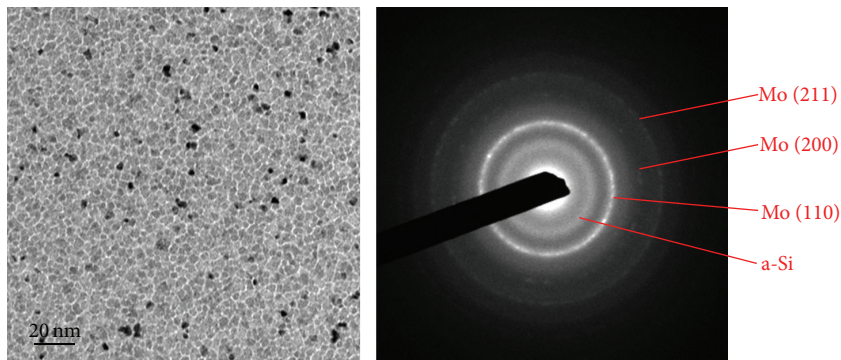


FIGURE 2: TEM bright field image and electron diffraction pattern of the as-deposited Mo/Si bilayer.

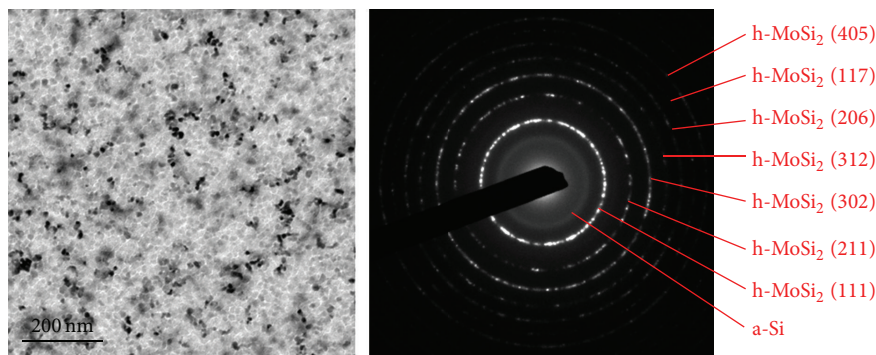


FIGURE 3: TEM bright field image and electron diffraction pattern of the 300°C-annealed Mo/Si bilayer.

Besides, the melting temperatures of MoSi_2 and Mo_3Si_2 were 1870 and 2190°C, respectively [22]. Commonly, the higher melting temperature of material would lead to a slower rate of formation. It can be speculated that the formation of Mo_3Si_2 is more difficult than MoSi_2 . This could be the reason why Mo_3Si_2 phase did not appear in this study. Based on previous research [16], the difference in reflectivity resulted from the materials with different complex dielectric functions. In other words, the reflectivity of material can be changed via the phase transition process. Consequently, the decreased reflectivity of our sample (shown in Figure 1) with increasing the temperature from 255 to 425°C can be ascribed to the transition from Mo phase to h- MoSi_2 and Mo_3Si phases. Moreover, in this study, there is another factor to affect the sample reflectivity, that is, the grain feature of the sample. In Figure 2, the small and uniform grain size of as-deposited film can result in the reduction of optical anisotropy and lead to high reflectivity. However, as the Mo/Si bilayer was annealed at 450°C (Figure 4), the nonuniform grain size would induce optical anisotropy, which caused the lower reflectivity of the annealed films. Actually, the optical isotropy and anisotropy of materials are also related to the crystal structures. This implies that h- MoSi_2 and Mo_3Si structures could both possess optical anisotropy, leading to the decreased reflectivity.

The reflectivity spectra in the wavelength ranging from 350 to 1000 nm for as-deposited, 300°C-annealed and 450°C-annealed ZnS- SiO_2 /Mo/Si/ZnS- SiO_2 samples are presented in Figure 5. For as-deposited sample, the reflectivity at a wavelength of 405 nm was measured to be 50.7%. After annealing at 300 and 450°C for 15 min, the reflectivities (at the wavelength of 405 nm) of these samples were decreased to 46.2% and 37.6%, respectively. The optical contrast is defined as $((R_1 - R_2)/R_1) \times 100\%$, where R_1 is the reflectivity of as-deposited state and R_2 is the reflectivity of annealed state. The optical contrast (at the wavelength of 405 nm) between as-deposited and 450°C-annealed Mo/Si films can be evaluated to 25.8%. It indicates that Mo/Si bilayer is suitable for BD-R application.

Figures 6(a) and 6(b) show the depth profiles measured by AES for as-deposited and 450°C-annealed Mo/Si films, respectively. Unlike the other annealing time of 15 min, the sample for AES measurement was only annealed for 3 min. In Figure 6(a), it was found that the film was composed by two layers, which were Mo layer and Si layer. After annealing at 450°C, the film was divided into three layers, that is, Mo layer, Mo-Si mixing layer, and Si layer. According to TEM observations, it can be confirmed that the Mo-Si mixing layer included the h- MoSi_2 and Mo_3Si phases. Additionally,

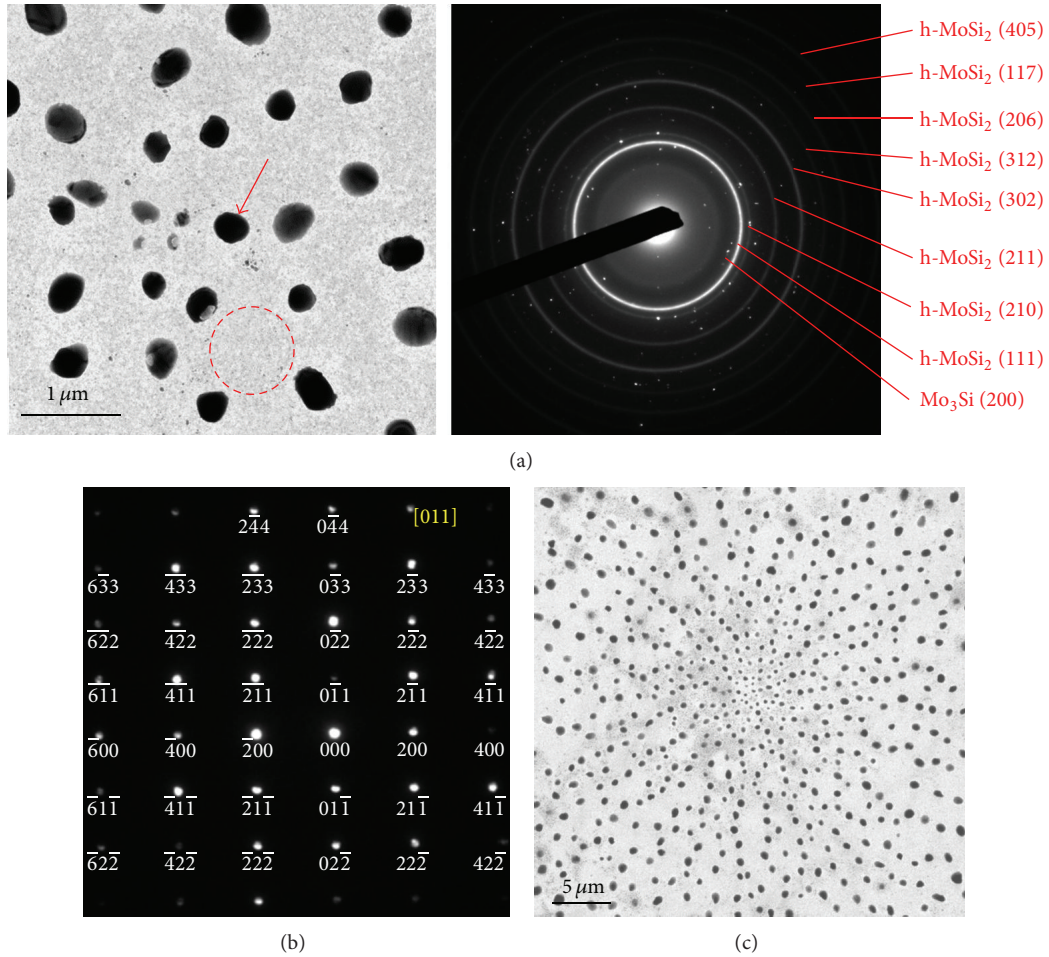


FIGURE 4: (a) TEM bright field image and electron diffraction pattern of the 450°C-annealed Mo/Si bilayer, (b) the SAED pattern of larger grain marked by an arrow in (a), and (c) TEM image with lower magnification.

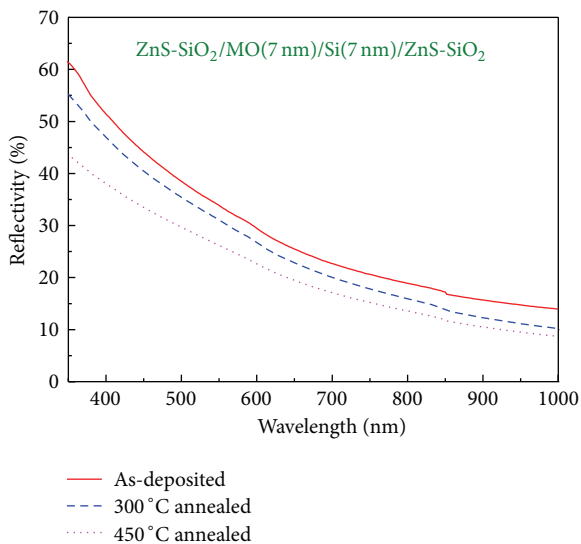


FIGURE 5: Variations of the reflectivity with wavelength for Mo/Si films at as-deposited, 300°C-annealed, and 450°C-annealed states.

the AES results revealed that the Mo silicide was formed by the interdiffusion of Mo and Si atoms, which was in good agreement with Holloway et al. research [17].

Figure 7 exhibits the dynamic test results that the jitter values and modulations vary with writing powers at 1× and 4× recording speeds. The suggested modulation and jitter value for BD-R should be larger than 0.4 and lower than 7%, respectively. As we can see, all measured modulations are larger than 0.4. From TEM results, the changes of structural phase and grain size uniformity in the as-deposited and annealed states would lead to high optical contrast. It probably results in enough modulation of the disc sample before and after laser writing. Experimental results show that the minimum jitter values are obtained to be 6.5% at 7.4 mW and 6.8% at 10.65 mW, respectively, for 1× and 4× recording speeds. It indicates that the Mo/Si bilayer has great potential in BD-R.

4. Conclusion

In summary, we have proposed a new BD-R containing Mo/Si recording layer. Thermal analysis shows that the Mo/Si bilayer

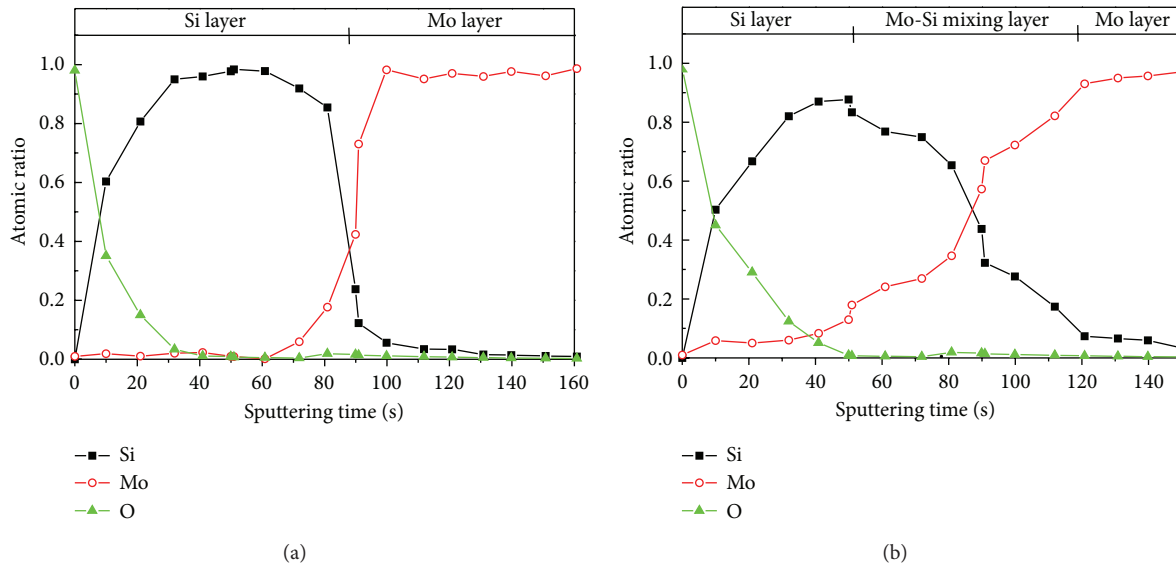


FIGURE 6: Element concentration depth profiles of (a) as-deposited and (b) 450°C-annealed Mo/Si bilayer samples.

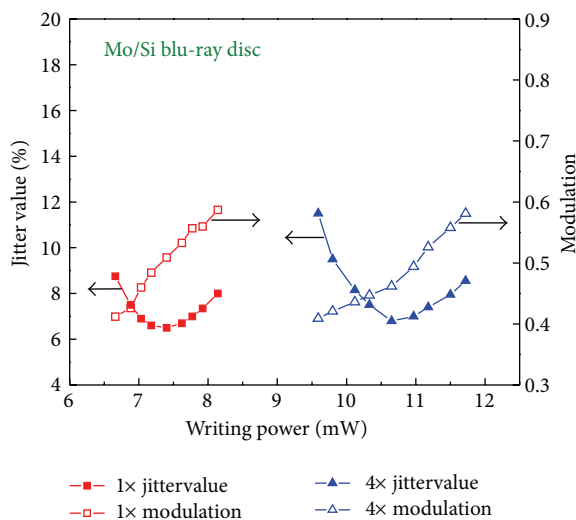


FIGURE 7: Jitter values and modulations as a function of writing power at the 1× and 4× recording speeds.

has a reflectivity change with the temperature ranging from 255 to 425°C. The Mo phase with grain size of 5 nm was found in the as-deposited film. After annealing at 300 and 450°C, the h-MoSi₂ and Mo₃Si were sequentially appeared. Due to the thicker Mo layer, there was no Si crystallization forming in the annealed film. The AES result confirmed that the formation of Mo silicide after annealing resulted from the interdiffusion of Mo and Si atoms. For 1× and 4× recording speeds, the optimum jitter values of 6.5% and 6.8% can be achieved at the recording powers of 7.4 and 10.65 mW, respectively. Obviously, the Mo/Si bilayer has great feasibility for write-once blue laser optical recording.

Conflict of Interests

The authors declare that there is no conflict of interests regarding the publication of this paper.

Acknowledgments

This research was supported by the National Science Council of Taiwan, Republic of China, under Contract nos. NSC 98-2221-E-002-053-MY3 and NSC 102-2221-E-366-002, respectively.

References

- [1] L. Hultman, A. Robertsson, H. T. G. Hentzell, I. Engström, and P. A. Psaras, "Crystallization of amorphous silicon during thin-film gold reaction," *Journal of Applied Physics*, vol. 62, no. 9, pp. 3647–3655, 1987.
- [2] S. W. Russell, J. Li, and J. W. Mayer, "In situ observation of fractal growth during a-Si crystallization in a Cu₃Si matrix," *Journal of Applied Physics*, vol. 70, no. 9, pp. 5153–5155, 1991.
- [3] B. Bian, J. Yie, B. Li, and Z. Wu, "Fractal formation in a-Si:H/Ag/a-Si:H films after annealing," *Journal of Applied Physics*, vol. 73, no. 11, pp. 7402–7406, 1993.
- [4] C. A. Achete, F. L. Freire Jr., G. Mariotto, and E. Zangheillni, "Low-temperature silicon crystallization mediated by copper suicide formation in Cu/a-Si: H bilayers," *Materials Letters*, vol. 18, no. 4, pp. 218–222, 1994.
- [5] M. Zou, L. Cai, H. Wang, and W. Brown, "Nano-aluminum-induced crystallization of amorphous silicon," *Materials Letters*, vol. 60, no. 11, pp. 1379–1382, 2006.
- [6] H. Inoue, K. Mishima, M. Aoshima, H. Hirata, T. Kato, and H. Utsunomiya, "Inorganic write-once disc for high speed recording," *Japanese Journal of Applied Physics 1: Regular Papers and Short Notes and Review Papers*, vol. 42, no. 2, pp. 1059–1061, 2003.

- [7] Y.-C. Her and C.-W. Chen, "Crystallization kinetics of ultrathin amorphous Si film induced by Al metal layer under thermal annealing and pulsed laser irradiation," *Journal of Applied Physics*, vol. 101, no. 4, Article ID 043518, 2007.
- [8] Y.-C. Her, S.-T. Jean, and J.-L. Wu, "Crystallization kinetics and recording mechanism of a-SiNi bilayer for write-once blue-ray recording," *Journal of Applied Physics*, vol. 102, no. 9, Article ID 093503, 2007.
- [9] H.-C. Mai, T.-E. Hsieh, and S.-Y. Jeng, "Characterization of write-once blu-ray disk containing Cu-Al/Si recording layer using transmission electron microscopy," *Applied Physics Letters*, vol. 98, no. 9, Article ID 094103, 2011.
- [10] R. S. Rosen, M. A. Viliardos, M. E. Kassner, D. G. Stearns, and S. P. Vernon, "Thermal stability of Mo/Si multilayers," in *Multilayer Optics for Advanced X-Ray Applications*, vol. 1547 of *Proceedings of SPIE*, pp. 212–220, 1991.
- [11] J. M. Freitag and B. M. Clemens, "Stress evolution in Mo/Si multilayers for high-reflectivity extreme ultraviolet mirrors," *Applied Physics Letters*, vol. 73, no. 1, pp. 43–45, 1998.
- [12] N.-W. Pu, J. Bokor, S. Jeong, and R.-A. Zhao, "Picosecond ultrasonic study of Mo/Si multilayer structures using an alternating-pump technique," *Applied Physics Letters*, vol. 74, no. 2, pp. 320–322, 1999.
- [13] E. J. Takahashi, Y. Nabekawa, and K. Midorikawa, "Low-divergence coherent soft x-ray source at 13 nm by high-order harmonics," *Applied Physics Letters*, vol. 84, no. 1, pp. 4–6, 2004.
- [14] T. Mocek, B. Rus, M. Stupka et al., "Focusing a multimillijoule soft x-ray laser at 21 nm," *Applied Physics Letters*, vol. 89, no. 5, Article ID 051501, 2006.
- [15] Y. Ueno, G. Soumagne, A. Sumitani, A. Endo, T. Higashiguchi, and N. Yugami, "Reduction of debris of a CO₂ laser-produced Sn plasma extreme ultraviolet source using a magnetic field," *Applied Physics Letters*, vol. 92, no. 21, Article ID 211503, 2008.
- [16] E. García-García, A. Mendoza-Galván, Y. Vorobiev et al., "Optical properties of Ge:Sb:Te ternary alloys," *Journal of Vacuum Science & Technology A*, vol. 17, no. 4, pp. 1805–1810, 1999.
- [17] K. Holloway, K. B. Do, and R. Sinclair, "Interfacial reactions on annealing molybdenum-silicon multilayers," *Journal of Applied Physics*, vol. 65, no. 2, pp. 474–480, 1989.
- [18] A. Misra, J. J. Petrovic, and T. E. Mitchell, "Microstructures and mechanical properties of a Mo₃Si-Mo₅Si₃ composite," *Scripta Materialia*, vol. 40, no. 2, pp. 191–196, 1998.
- [19] S. P. Murarka, D. B. Fraser, T. F. Retajczyk Jr., and T. T. Sheng, "Cospattered molybdenum silicides on thermal SiO₂," *Journal of Applied Physics*, vol. 51, no. 10, pp. 5380–5385, 1980.
- [20] A. A. Sharif, "High-temperature oxidation of MoSi₂," *Journal of Materials Science*, vol. 45, no. 4, pp. 865–870, 2010.
- [21] J.-K. Yoon, J.-Y. Byun, G.-H. Kim, J.-S. Kim, and C.-S. Choi, "Growth kinetics of three Mo-silicide layers formed by chemical vapor deposition of Si on Mo substrate," *Surface and Coatings Technology*, vol. 155, no. 1, pp. 85–95, 2002.
- [22] J. Y. P. Mui, "Corrosion mechanism of metals and alloys in the silicon-hydrogen-chlorosilane system at 500 C," *Corrosion*, vol. 41, no. 2, pp. 63–69, 1985.

Research Article

Structural, Surface Morphology and Optical Properties of ZnS Films by Chemical Bath Deposition at Various Zn/S Molar Ratios

Fei-Peng Yu,¹ Sin-Liang Ou,¹ Pin-Chuan Yao,² Bing-Rui Wu,¹ and Dong-Sing Wu^{1,2}

¹ Department of Materials Science and Engineering, National Chung Hsing University, 250 Kuo Kuang Road, Taichung 40227, Taiwan

² Department of Materials Science and Engineering, Da-Yeh University, Changhua 51591, Taiwan

Correspondence should be addressed to Dong-Sing Wu; dsw@dragon.nchu.edu.tw

Received 13 December 2013; Revised 8 March 2014; Accepted 10 March 2014; Published 31 March 2014

Academic Editor: Sheng-Po Chang

Copyright © 2014 Fei-Peng Yu et al. This is an open access article distributed under the Creative Commons Attribution License, which permits unrestricted use, distribution, and reproduction in any medium, provided the original work is properly cited.

In this study, ZnS thin films were prepared on glass substrates by chemical bath deposition at various Zn/S molar ratios from 1/50 to 1/150. The effects of Zn/S molar ratio in precursor on the characteristics of ZnS films were demonstrated by X-ray diffraction, scanning electron microscopy, optical transmittance, X-ray photoelectron spectroscopy, and Fourier transform infrared spectrometry. It was found that more voids were formed in the ZnS film prepared using the precursor with Zn/S molar ratio of 1/50, and the other ZnS films showed the denser structure as the molar ratio was decreased from 1/75 to 1/150. From the analyses of chemical bonding states, the ZnS phase was indeed formed in these films. Moreover, the ZnO and Zn(OH)₂ also appeared due to the water absorption on film surface during deposition. This would be helpful to the junction in cell device. With changing the Zn/S molar ratio from 1/75 to 1/150, the ZnS films demonstrate high transmittance of 75–88% in the visible region, indicating the films are potentially useful in photovoltaic applications.

1. Introduction

Zinc sulfide (ZnS) is a II-VI compound semiconductor with a wide direct band gap ($E_g = 3.6\sim 3.8$ eV). Moreover, ZnS has the high refractive index (2.35 at 632 nm) and high dielectric constant (9 at 1 MHz) [1]. As a result, it can be widely applied in the optoelectronic applications consisting of light emitting diodes with short wavelength, electroluminescent devices, and solar cells. For the photovoltaic applications, ZnS thin film is also transparent in all wavelengths of solar spectrum and has high absorption for the wavelength below 520 nm as compared to CdS. Many techniques including sputtering [2], molecular beam epitaxy [3], pulsed laser deposition [4], chemical vapor deposition [5], successive ionic layer adsorption and reaction [6], spray pyrolysis [7], and chemical bath deposition (CBD) [1, 8] have been proposed to fabricate the ZnS thin films. Among these methods, CBD is most attractive because it can be employed as the large-area growth without

vapor deposition related to physical techniques and free of some inherent problems associated with high temperature fabrication [9].

For the ZnS growth by CBD process, a soluble salt of Zn ion and nonmetallic S source compound dissolved in an aqueous solution is required, reacting by the following equation: $Zn^{2+} + S^{2-} \rightarrow ZnS$, $K_{sp} = 10^{-24.7}$ [10]. Owing to the low solubility product of Zn^{2+} and S^{2-} , ZnS precipitation will take place rapidly at very low concentration (homogeneous process), which results in the loose structure and poor transmittance in the thin film. However, the ZnS thin film with good uniformity and high transmittance can be achieved using the complex agents, such as trisodium citrate, ethylenediamine, and nitrilotriacetate (heterogeneous process). With the assistance of complex agents, the metal ions and negative ions were released slowly and then reacted to form the compound. The process is used to avoid the fast precipitation of the compound in the solution [11]. Moreover,

the use of hydrazine hydrate as second ligand in the process can also enhance the homogeneity and adhesion of the film and increase the growth rate [9].

Up to now, the CBD-ZnS films are always formed by using Zn-contained and S-contained solutions, which have the similar molar concentration to each other. For example, as the concentration of Zn-contained solution was fixed, the same or 2–10 times concentration of S-contained solution was used in the CBD process. However, there are very few researches on the CBD-ZnS films by these two solutions with large difference in concentration.

In this study, the CBD technique was performed to prepare the ZnS films. By modifying the Zn/S molar ratio from 1/50 to 1/150, the S-contained solutions with much higher concentrations than that of Zn-contained solution were employed to form the ZnS films. This could be expected that more nucleation sites will appear during the CBD process for the formation of ZnS clusters. As a result, the quality of ZnS film will be better and the growth rate can be increased. The morphology, chemical bonding states, and structural and optical properties of these ZnS films have been investigated in detail.

2. Experimental Procedure

In our work, ZnS thin films were prepared on the glass and Si substrates by CBD method. The substrates were cleaned ultrasonically by detergent solution, acetone, and deionized water, respectively, to ensure the complete cleanness. For the CBD process, the aqueous solutions of zinc sulfate (ZnSO_4) and thiourea ($\text{SC}(\text{NH}_2)_2$) were used to grow the ZnS films. The concentration of ZnSO_4 solution was fixed at 1.4×10^{-3} M, and the concentration of $\text{SC}(\text{NH}_2)_2$ solution was increased from 0.07 to 0.21 M, leading to the precursors with various Zn/S molar ratios from 1/50 to 1/150 in the mixed solution. The ZnS films prepared using the precursors with various Zn/S molar ratios of 1/50, 1/75, 1/100, 1/125, and 1/150 are denoted as samples A, B, C, D, and E, corresponding to the used $\text{SC}(\text{NH}_2)_2$ concentrations of 0.07, 0.105, 0.14, 0.175, and 0.21 M, respectively. Firstly, the 100 mL of 1.4×10^{-3} M ZnSO_4 and 26 mL of 28%–30% NH_4OH were mixed in a glass beaker by stirring for 10 min to form a stable complex with zinc ions. Next, the $\text{SC}(\text{NH}_2)_2$ with desired concentration was added to a 6 mL 98+% hydrazine hydrate in another beaker by stirring for 10 min. Then, these two solutions were poured into a glass tank and placed on a hotplate stirrer. For the films growth, the substrates were vertically immersed in the solution, and the reaction temperature was maintained at 85°C. The substrates were taken out after 2 hours and followed by cleaning them with deionized water.

The crystal structures of ZnS films were examined by X-ray diffraction (XRD, PANalytical, X'Pert Pro MRD) and transmission electron microscopy (TEM, JEOL JEM-2100F). The $\text{Cu K}\alpha$ line ($\lambda = 1.541874 \text{ \AA}$) was applied for the source and Ge (220) was employed as the monochromator for XRD. The films morphology was investigated by a scanning electron microscopy (SEM, JEOL JSM-6700F). The transmittance spectra of the films were determined by the UV-Vis

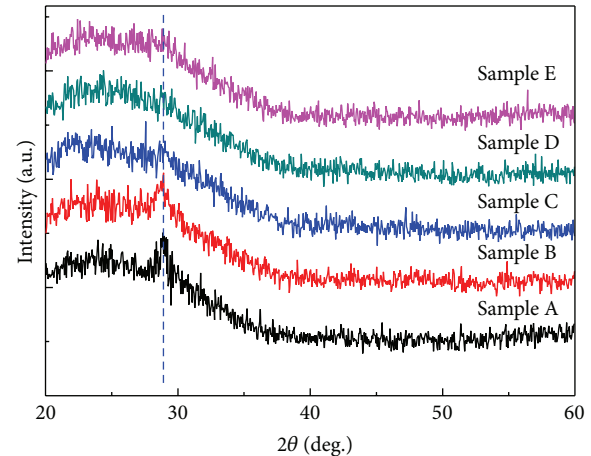


FIGURE 1: XRD patterns of samples A–E on glass substrates.

spectroscopy (UV-3101PC, Shimadzu). X-ray photoelectron spectroscopy (XPS, ULVAC-PHIPHI 5000) was used to analyze the film composition. Moreover, the existences of oxygen and carbon formed in the CBD process were also detected by XPS. The $\text{Al K}\alpha$ (1486.7 eV) radiation was applied for the excitation source. The chemical bonding states of ZnS films were characterized by Fourier transform infrared spectrometry (FTIR, DA8.3, Bomem Inc.) using grazing incident angle reflectance method.

3. Results and Discussion

Generally, the crystal structures of ZnS exist in two forms, that is, the cubic (zincblende) and hexagonal (wurtzite) phases. The cubic ZnS is stable at room temperature, while the hexagonal ZnS is formed as the temperature is above 1020°C [12]. Figure 1 shows the results of XRD θ - 2θ scan for samples A–E with increasing 2θ from 20° to 60°. As the ZnS films deposited using the precursors with Zn/S molar ratio of 1/100–1/150 (samples C, D and E), no obvious diffraction peak can be found except for a broad hump appeared in the 2θ range of 20–35°, indicating the amorphous phase was formed in these films. For the CBD process at Zn/S molar ratio of 1/50–1/75, only one diffraction peak around $2\theta = 28.5^\circ$ with low intensity appeared in these two spectra, which can be related to the cubic ZnS with (111) plane. Some reports have been proposed to demonstrate the ZnS grown by CBD method using ZnSO_4 or ZnCl_2 as precursors possessed the cubic structure [13, 14]. As a result, the peak appeared in our result ought to belong to the cubic structure because of the low temperature process and the ZnSO_4 precursor used in the chemical reaction. As well known, the film thickness is an important factor for the determination of crystalline structure in the film. According to our SEM results (as shown in below), the samples A and B both possessed a very thin thickness less than 70 nm. As a result, there is no diffraction peak indexed to cubic or hexagonal ZnS phase in these two films except for the (111) plane. Although the hexagonal ZnS could present the better optical and electrical properties

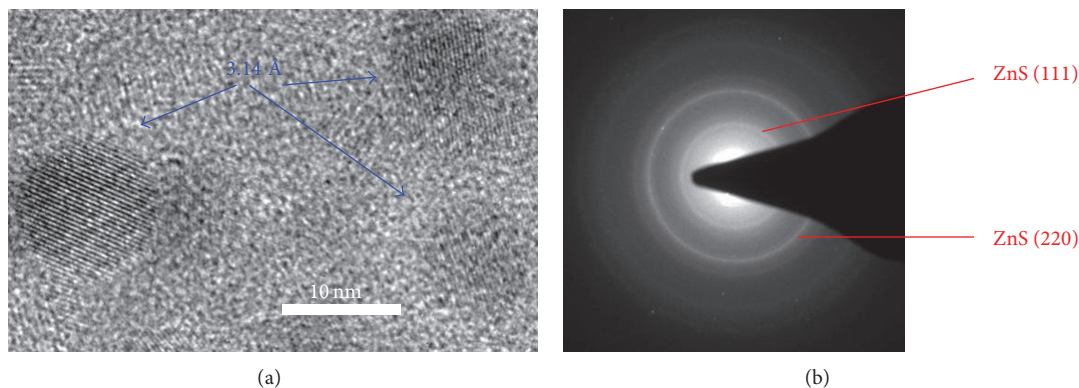


FIGURE 2: (a) High-resolution TEM bright field photograph and (b) electron diffraction pattern of sample B.

than those of cubic ZnS, the hexagonal ZnS is relatively difficult to prepare. According to Gilbert et al. research [12], the high temperature (above 1020°C) process was performed to fabricate the hexagonal ZnS bulk material. In fact, the CBD-ZnS films were usually prepared at low temperature (from room temperature to 90°C). It indicates that the high temperature process is unsuitable for the preparation of ZnS film by using CBD method. Additionally, the hexagonal phase may be formed by performing the postannealing process to ZnS sample at high temperature. Nevertheless, based on previous research [15], the annealing process would induce the significant reduction in the optical transmittance of CBD-ZnS film, lowering the feasibility for the photovoltaic applications. On the other hand, although no characteristic peaks induced by the Zn(OH)_2 or ZnO phase were detected in our result, these compounds were formed in the films by analyzing the bonding states in XPS measurements, as exhibited in the following discussion.

Figure 2(a) displays the high-resolution TEM image of sample B to check the formation of crystalline structure in ZnS films. It can be seen that there were some grains with uniform spherical shape in the image (marked by the blue arrows), and the size was measured to be about 8–10 nm. This indicates the nanocrystalline structure was indeed existed in the film. In addition, the presence of nanocrystal grains without aggregation supported the XRD peak with low intensity presented in Figure 1. Moreover, we observed the d -spacing clearly appeared in the grains. From our calculation, these grains all have the similar d -spacing value about 3.14 Å, which can be indexed to the (111) plane of cubic ZnS. It is in good agreement with the XRD result. Except for the XRD and high-resolution TEM measurements, the electron diffraction pattern was also used to further analyze the phase of ZnS film (sample B). As shown in Figure 2(b), it indicates that the ZnS film possesses polycrystalline nature with the cubic phase, and the diffraction pattern rings are identified to ZnS (111) and ZnS (220).

Figures 3(a)–3(e) show the plain-view SEM images of ZnS films with various reaction conditions (samples A–E). It was found that there were many voids in sample A, and the voids were reduced with increasing the $\text{SC(NH}_2)_2$ concentration, indicating that a denser structure on surface appeared in the ZnS films prepared using the precursors with

Zn/S molar ratio of 1/75–1/150. These surface states strongly influence the optical properties of ZnS film consisting of transmittance, absorbance, and reflection. Moreover, it is worth mentioning that the discontinuous film was emerged in sample A, revealing the aggregation of grains did not form the film in such reaction condition. This could lead to a leakage current as the ZnS film is used as the buffer layer for cell device. Except for sample A, the coalescence of grains was improved in the other samples (B–E), and the good adhesion of these films to the glass substrates was also observed. Cross-sectional SEM images indicate that the thicknesses of sample A, B, C, D, and E are measured to be 92, 63, 60, 61, and 59 nm, respectively, as shown in Figures 3(f)–3(j). Obviously, at Zn/S molar ratio of 1/50 in the CBD process, the ZnS film has higher growth rate than the others. Besides, at Zn/S molar ratio of 1/75–1/150, the ZnS films have the similar growth rate to each other. This is because the ZnS films with Zn/S molar ratio of 1/75~1/150 all possess the dense structure (observed by SEM). The adhesion of CBD-ZnS film to the substrate is also an important factor for the photovoltaic applications. Based on our results, the adhesion of CBD-ZnS film to the substrate became worse as the Zn/S molar ratio was decreased. Actually, in this study, the adhesions of these ZnS films are good enough to use in the photovoltaic applications, even for the ZnS film with a lower Zn/S molar ratio of 1/150. However, further decreasing the Zn/S molar ratio to 1/200 and 1/300, these two ZnS films possessed very poor adhesion, which were unsuitable for the fabrication of optoelectronic devices. Besides, as the Zn/S molar ratio was reduced to 1/200 and 1/300, it would result in a lot of Zn(OH)_2 formation in the ZnS sample. The excessive Zn(OH)_2 formation can decrease the optical transmittance of ZnS film, causing the degradation in the device performance.

Figure 4(a) shows the transmittance spectra of samples A–E recorded in a wavelength range of 200–1000 nm. We can observe that the sample A has a lower transmittance than that of samples B–E in the spectral range of 350–1000 nm. For the ZnS films deposited using the precursors with Zn/S molar ratio of 1/75–1/150 (samples B–E), it can be found that the transmittance is higher than 75% when the wavelength is larger than 360 nm and reaches at a maximum value about 88%. According to the results of film adhesion and optical transmittance, it indicates that the ZnS film with Zn/S molar

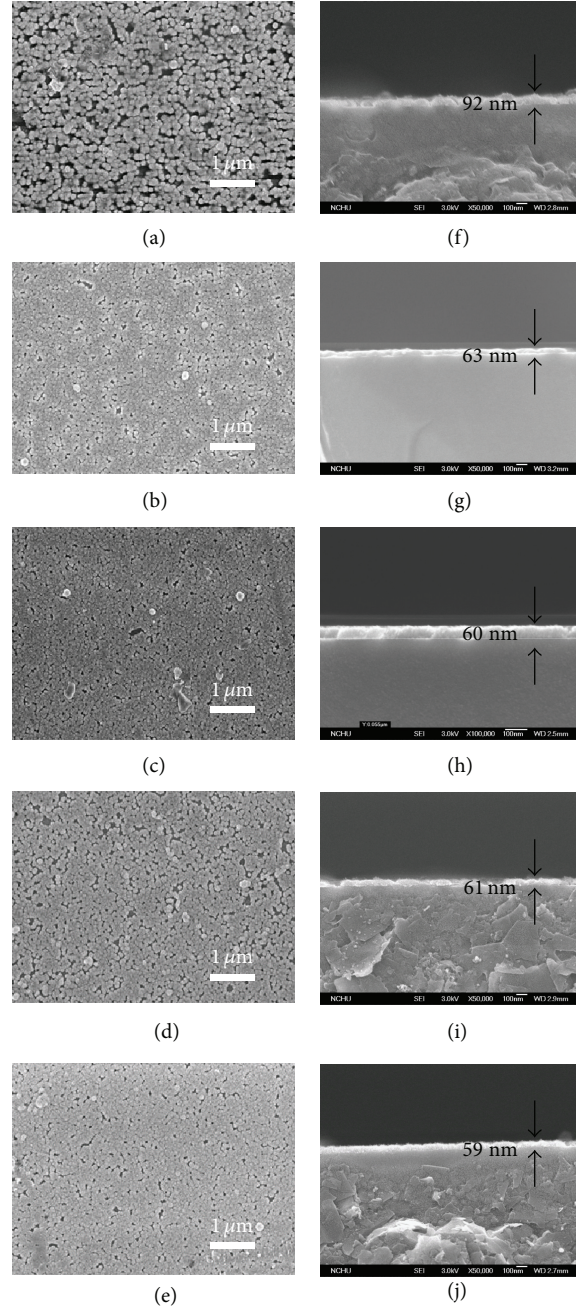


FIGURE 3: ((a)–(e)) Plane-view SEM images and ((f)–(j)) cross-sectional SEM images of samples A–E.

ratio of 1/75 is most suitable for use in the buffer layer of solar energy device. On the other hand, all ZnS films exhibit the clear absorption edges near 310–320 nm. From the Beer-Lambert law [16], the absorption coefficient (α) can be obtained by the following equation:

$$\alpha = \frac{1}{t} \ln\left(\frac{1}{T}\right), \quad (1)$$

where t is the film thickness and T the optical transmittance. Because ZnS belongs to the direct band gap semiconductor,

the relationship between α and incident photon energy ($h\nu$) is represented as [17]

$$\alpha h\nu = A(h\nu - E_g)^{1/2}, \quad (2)$$

where A is the constant and E_g the band gap of semiconductor. In the curve of α^2 versus $h\nu$, the band gap is determined by extrapolating the linear region near the onset, as shown in Figure 4(b). The band gaps of these samples are about 3.85–3.86 eV, which agree well with that of ZnS single crystal.

During the growth process of CBD-ZnS, not only the Zn and S were found in the film, but also the elements of

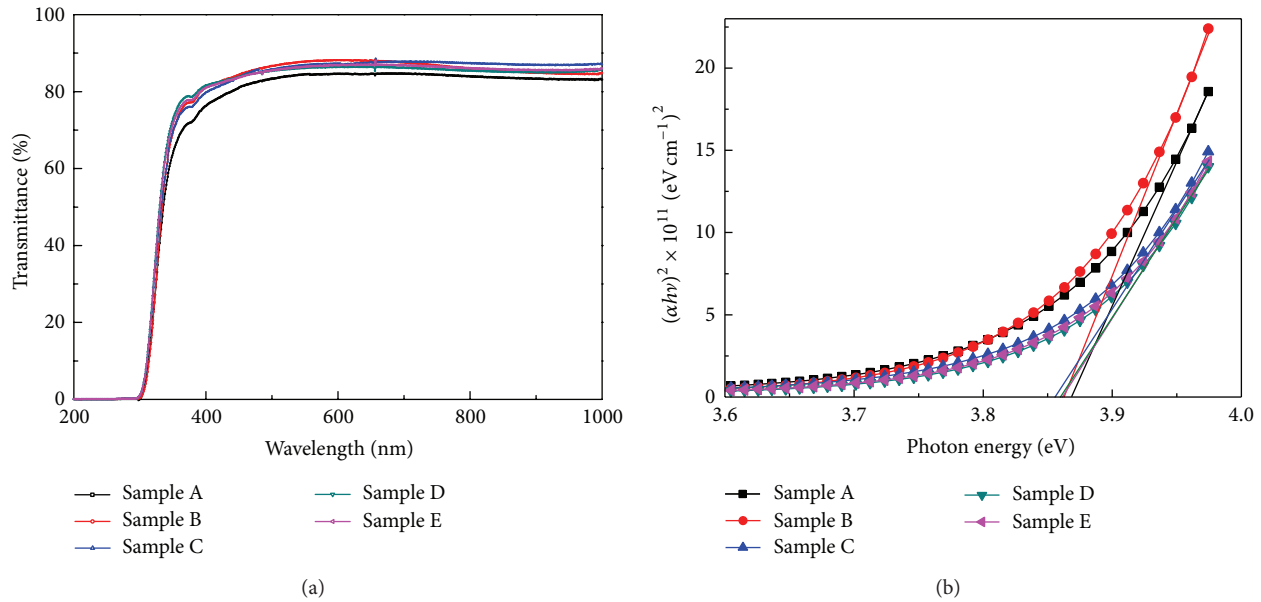
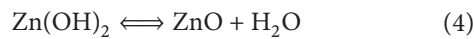
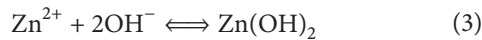


FIGURE 4: (a) Transmittance spectra with the measured wavelength ranging from 200 to 1000 nm and (b) the plots of $(\alpha h\nu)^2$ versus photon energy for samples A–E.

O and C appeared. Actually, there were probably a lot of oxygen existed in the ZnS layer via the formations of ZnO and Zn(OH)_2 by the following chemical reactions:



On the other hand, the carbon in ZnS films could be resulted from the initial precursor of thiourea. According to the past research [18], it demonstrated that some amount of ZnO and Zn(OH)_2 in the ZnS buffer was required, which can provide a good junction to the cell and create an efficient device. As a result, the XPS measurements were performed to check the existence of ZnO or Zn(OH)_2 in these ZnS films prepared using the precursors with various Zn/S molar ratios. Figures 5(a)–5(e) display the XPS results of O1s spectra for the samples A–E. All XPS spectra of the ZnS films were fitted well with Gaussian functions. The fitting results revealed that the O1s peaks centered at 531.3–531.8 eV, which was deconvoluted into three Gaussian peaks centered at 530.3 eV (Zn(OH)_2), 531.4 eV (ZnO), and 533.3 eV (C–O bond), respectively. Based on the quantitative analyses, we found only very few C–O bonds were formed in the ZnS films. It proved that the main formations of ZnS, Zn(OH)_2 , and ZnO were included in these films, leading to the assistance for cell device performance. On the other hand, it can be observed that the peak positions of O1s were 531.8, 531.5, 531.4, 531.3, and 531.3 eV, respectively, as the ZnS films were prepared using the precursors with Zn/S molar ratios of 1/50, 1/75, 1/100, 1/125, and 1/150. It is well known that the peak position of O1s can be used to determine the amount of oxygen atoms in the film. From our results, a shift of O1s binding energy in the direction toward lower energy side was found with decreasing the Zn/S molar ratio in the precursor, which indicated that the number of oxygen

atom in the ZnS film was decreased. Obviously, the lower the Zn/S molar ratio in precursor, the more the ZnS nucleation could be. This will induce the less Zn atoms provided for oxygen atoms to form the ZnO compound, resulting in the reduction of oxygen content in the ZnS film.

To investigate the chemical bonding states of these films, the FTIR analyses in a transmittance mode were applied for ZnS films grown on the Si substrates with high resistance. Figure 6 shows the FTIR spectra measured for samples A–E. The absorption band located at 615 cm^{-1} can be attributed to the formation of ZnS phase [19]. Due to the choice of Si substrate, it caused the weak peak at 799.5 cm^{-1} related to the Si–O bond. The absorption band appeared at 1086 cm^{-1} was resulted from the Zn–OH vibrations. The band at 1600 cm^{-1} and broad peak in the region of $3000\text{--}3600 \text{ cm}^{-1}$ were induced by the stretching and bending vibrations of hydroxyl groups, respectively, indicating that the ZnS could absorb the water on the film surface during the CBD process [20]. Moreover, the band at 2926 cm^{-1} can be ascribed to the C–H stretching vibrations [21]. Because the corresponded wavenumber of Zn–O bond is outside the measured range, there is no Zn–O peak formed in the FTIR spectra. Based on the FTIR results, it proves the ZnS phase is certainly formed in these films. Furthermore, the oxygen and carbon are also found in these films by FTIR measurement. This agrees with the result from XPS spectra, as displayed in Figure 5.

4. Conclusion

In summary, the technique of chemical bath deposition was performed to grow the ZnS thin films. As the concentration of ZnSO_4 solution was fixed, the Zn/S molar ratio of precursor was varied from 1/50 to 1/150 by changing the concentration

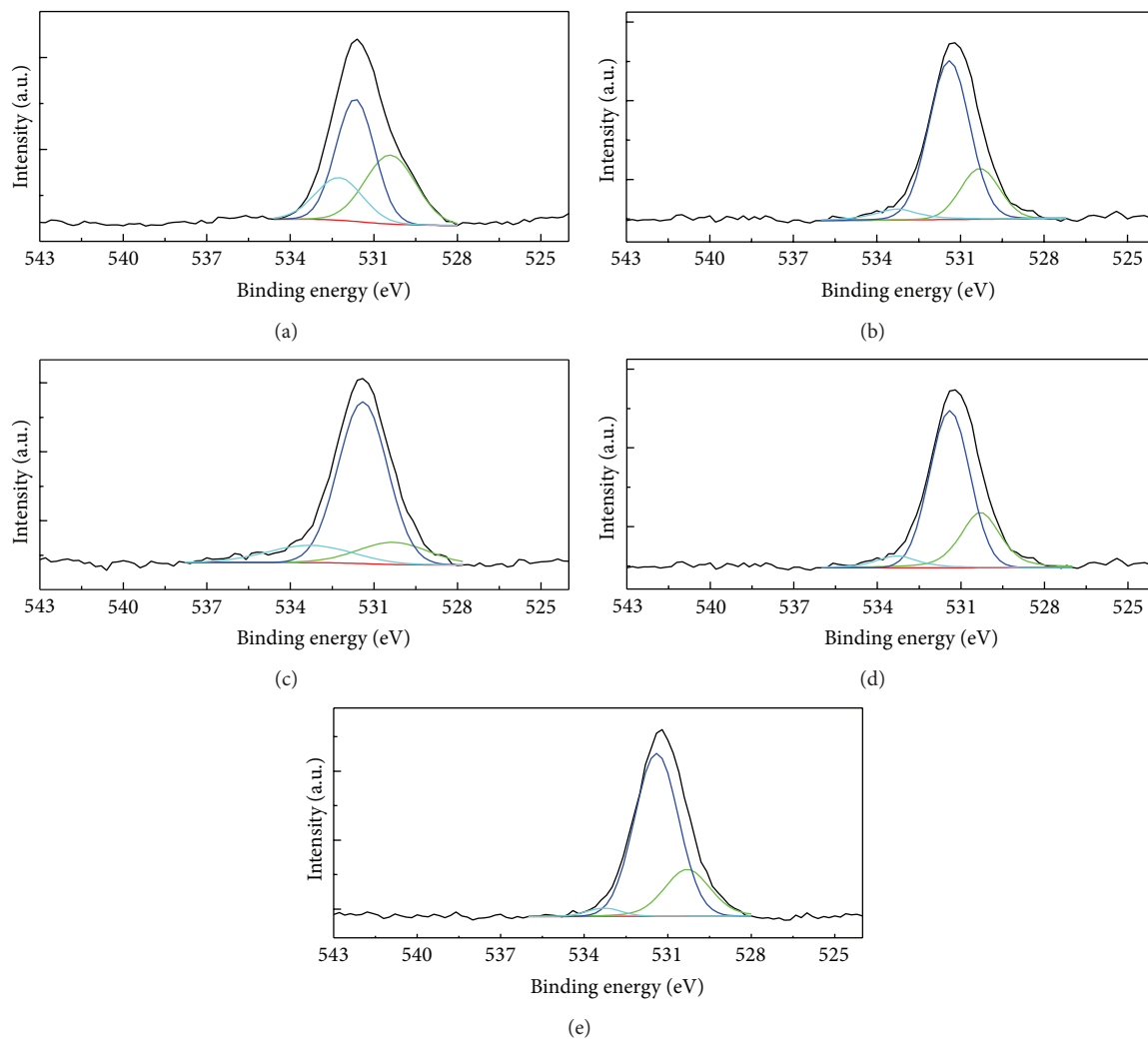


FIGURE 5: ((a)–(e)) XPS spectra of O1s core level for samples A–E.

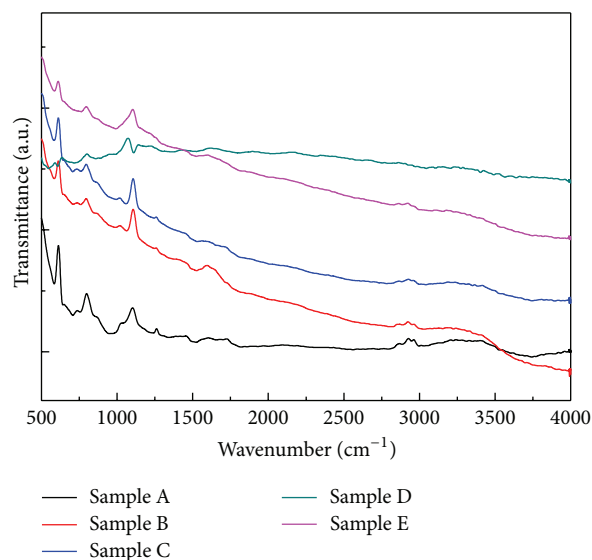


FIGURE 6: FTIR spectra using a transmittance mode for samples A–E.

of $\text{SC}(\text{NH}_2)_2$ solution. The ZnS , ZnO , and $\text{Zn}(\text{OH})_2$ were all found in these films. Because of the surface absorption of water in the films growth, it led to the formations of ZnO and $\text{Zn}(\text{OH})_2$. At the Zn/S molar ratio of 1/75–1/150, the ZnS films presented a high transmittance of 75–88% in the range of visible wavelength (360–1000 nm), and their optical band gaps were measured to be about 3.85–3.86 eV. Based on the results of film adhesion and optical transmittance, it reveals that the ZnS film with Zn/S molar ratio of 1/75 is most suitable as the buffer layers in the photovoltaic device.

Conflict of Interests

The authors declare that there is no conflict of interests regarding the publication of this paper.

Acknowledgment

This research was supported by the National Science Council of Taiwan, Republic of China, under Contract no. NSC 99-2221-E-005-101-MY3.

References

- [1] K. Ahn, J. H. Jeon, S. Y. Jeong et al., “Chemical bonding states and atomic distribution within $\text{Zn}(\text{S},\text{O})$ film prepared on CIGS/Mo/glass substrates by chemical bath deposition,” *Current Applied Physics*, vol. 12, no. 6, pp. 1465–1469, 2012.
- [2] D. H. Hwang, J. H. Ahn, K. N. Hui, K. S. Hui, and Y. G. Son, “Structural and optical properties of ZnS thin films deposited by RF magnetron sputtering,” *Nanoscale Research Letters*, vol. 7, article 26, pp. 1–13, 2012.
- [3] J. P. Bosco, S. B. Demers, G. M. Kimball, N. S. Lewis, and H. A. Atwater, “Band alignment of epitaxial $\text{ZnS}/\text{Zn}_3\text{P}_2$ heterojunctions,” *Journal of Applied Physics*, vol. 112, no. 9, Article ID 093703, 2012.
- [4] S. Yano, R. Schroeder, H. Sakai, and B. Ullrich, “High-electric-field photocurrent in thin-film ZnS formed by pulsed-laser deposition,” *Applied Physics Letters*, vol. 82, no. 13, pp. 2026–2028, 2003.
- [5] M. W. Huang, Y. W. Cheng, K. Y. Pan, C. C. Chang, F. S. Shieu, and H. C. Shih, “The preparation and cathodoluminescence of ZnS nanowires grown by chemical vapor deposition,” *Applied Surface Science*, vol. 261, pp. 665–670, 2012.
- [6] G. Xu, S. Ji, C. Miao, G. Liu, and C. Ye, “Effect of ZnS and CdS coating on the photovoltaic properties of CuInS_2 -sensitized photoelectrodes,” *Journal of Materials Chemistry*, vol. 22, no. 11, pp. 4890–4896, 2012.
- [7] K. Nagamani, N. Revathi, P. Prathap, Y. Lingappa, and K. T. R. Reddy, “Al-doped ZnS layers synthesized by solution growth method,” *Current Applied Physics*, vol. 12, no. 2, pp. 380–384, 2012.
- [8] G. L. Agawane, S. W. Shin, M. S. Kim et al., “Green route fast synthesis and characterization of chemical bath deposited nanocrystalline ZnS buffer layers,” *Current Applied Physics*, vol. 13, no. 5, pp. 850–856, 2013.
- [9] P. O’Brien and J. McAleese, “Developing an understanding of the processes controlling the chemical bath deposition of ZnS and CdS ,” *Journal of Materials Chemistry*, vol. 8, no. 11, pp. 2309–2314, 1998.
- [10] F. A. Cotton and G. Wilkinson, *Advanced Inorganic Chemistry*, John Wiley & Sons, New York, NY, USA, 4th edition, 1980.
- [11] P. Roy, J. R. Ota, and S. K. Srivastava, “Crystalline ZnS thin films by chemical bath deposition method and its characterization,” *Thin Solid Films*, vol. 515, no. 4, pp. 1912–1917, 2006.
- [12] B. Gilbert, B. H. Frazer, H. Zhang et al., “X-ray absorption spectroscopy of the cubic and hexagonal polytypes of zinc sulfide,” *Physical Review B—Condensed Matter and Materials Physics*, vol. 66, no. 24, Article ID 245205, 2002.
- [13] A. Goudarzi, G. M. Aval, R. Sahraei, and H. Ahmadpoor, “Ammonia-free chemical bath deposition of nanocrystalline ZnS thin film buffer layer for solar cells,” *Thin Solid Films*, vol. 516, no. 15, pp. 4953–4957, 2008.
- [14] J. Cheng, D. F. Fan, H. Wang, B. W. Liu, Y. Zhang, and H. Yan, “Chemical bath deposition of crystalline ZnS thin films,” *Semiconductor Science and Technology*, vol. 18, no. 7, pp. 676–679, 2003.
- [15] F. Göde, “Annealing temperature effect on the structural, optical and electrical properties of ZnS thin films,” *Physica B: Condensed Matter*, vol. 406, no. 9, pp. 1653–1659, 2011.
- [16] J. D. J. Ingle and S. R. Crouch, *Spectrochemical Analysis*, Prentice Hall, New Jersey, NJ, USA, 1988.
- [17] A. Antony, K. V. Murali, R. Manoj, and M. K. Jayaraj, “The effect of the pH value on the growth and properties of chemical-bath-deposited ZnS thin films,” *Materials Chemistry and Physics*, vol. 90, no. 1, pp. 106–110, 2005.
- [18] R. N. Bhattacharya, M. A. Contreras, and G. Teeter, “18.5% Copper indium gallium diselenide (CIGS) device using single-layer, chemical-bath-deposited $\text{ZnS}(\text{O},\text{OH})$,” *Japanese Journal of Applied Physics: Letters B*, vol. 43, no. 11, pp. L1475–L1476, 2004.
- [19] H. Yang, J. Zhao, L. Song et al., “Photoluminescent properties of $\text{ZnS}:\text{Mn}$ nanocrystals prepared in inhomogeneous system,” *Materials Letters*, vol. 57, no. 15, pp. 2287–2291, 2003.
- [20] B. Mokili, Y. Charreire, R. Cortes, and D. Lincot, “Extended X-ray absorption fine structure studies of zinc hydroxo-sulphide thin films chemically deposited from aqueous solution,” *Thin Solid Films*, vol. 288, no. 1-2, pp. 21–28, 1996.
- [21] M. L. Larsson, A. Holmgren, and W. Forsling, “Xanthate adsorbed on ZnS studied by polarized FTIR-ATR spectroscopy,” *Langmuir*, vol. 16, no. 21, pp. 8129–8133, 2000.

Research Article

Investigation of Low-Frequency Noise Characterization of 28-nm High-k pMOSFET with Embedded SiGe Source/Drain

Shih-Chang Tsai,¹ San-Lein Wu,² Jone-Fang Chen,¹ Bo-Chin Wang,¹ Po Chin Huang,¹ Kai-Shiang Tsai,² Tsung-Hsien Kao,¹ Chih-Wei Yang,³ Cheng-Guo Chen,³ Kun-Yuan Lo,³ Osbert Cheng,³ and Yean-Kuen Fang¹

¹ Institute of Microelectronics and Department of Electrical Engineering, Advanced Optoelectronic Technology Center, Center for Micro/Nano Science and Technology, National Cheng Kung University, Tainan City 701, Taiwan

² Department of Electronic Engineering, Cheng Shiu University, Kaohsiung City 833, Taiwan

³ Central R&D Division, United Microelectronics Corporation (UMC), Tainan City 744, Taiwan

Correspondence should be addressed to Po Chin Huang; pchuang@mail.ncku.edu.tw

Received 10 December 2013; Revised 19 February 2014; Accepted 20 February 2014; Published 30 March 2014

Academic Editor: Sheng-Po Chang

Copyright © 2014 Shih-Chang Tsai et al. This is an open access article distributed under the Creative Commons Attribution License, which permits unrestricted use, distribution, and reproduction in any medium, provided the original work is properly cited.

We have studied the low-frequency noise characterizations in 28-nm high-k (HK) pMOSFET with embedded SiGe source/drain (S/D) through $1/f$ noise and random telegraph noise measurements simultaneously. It is found that uniaxial compressive strain really existed in HK pMOSFET with embedded SiGe S/D. The compressive strain induced the decrease in the tunneling attenuation length reflecting in the oxide trap depth from Si/SiO₂ interface to the HK layer, so that the oxide traps at a distance from insulator/semiconductor interface cannot capture carrier in the channel. Consequently, lower $1/f$ noise level in HK pMOSFET with embedded SiGe S/D is observed, thanks to the less carrier fluctuations from trapping/detrapping behaviors. This result represents an intrinsic benefit of HK pMOSFET using embedded SiGe S/D in low-frequency noise characteristics.

1. Introduction

Low-frequency noise is an important issue for analog, digital, mixed signal, and RF application. Nowadays, complementary metal-oxide-semiconductor (CMOS) technology has intruded into RF and/or analog circuits, and hence the excessive low-frequency noise will lead to a limitation of the functionality for related circuits [1, 2]. Low-frequency noise, including flicker ($1/f$) noise and random telegraph noise (RTN), is increasingly attracting much interest in the CMOS device and technology community. In metal-oxide-semiconductor field-effect transistor (MOSFET) devices, the origin of $1/f$ noise and RTN is considered stemming from the carrier behaviors related to the oxide traps. $1/f$ noise is most often due to fluctuations in carrier number and/or carrier scattering [3, 4]. RTN is another special kind of noise, which

also appears in a low-frequency spectrum and originates from the trapping/detrapping behavior of a single or few traps [5, 6].

On the other hand, the continued shrinking of conventional CMOS to enhance device performance has revealed limitations. The mobility enhancement has emerged as a key technology for improving drive current [7]. Ways of optimizing channel mobility had been proposed to overcome the limitations on the scaling down of devices and to further improve the speed of CMOS circuits. The introduction of channel strain engineering in the state-of-the-art CMOS technology is recognized as an indispensable performance booster in producing next generation CMOS devices [8, 9]. For p-type MOSFET (pMOSFET), using embedded SiGe in the recessed source/drain (S/D) region can efficiently provide uniaxial compressive strain in the channel and

improve hole mobility, bringing the enhancement of device performance [10–12]. In addition, high-k (HK) materials are also adopted into advanced CMOS process for solving the increased gate leakage current. This is because HK dielectrics are the promising candidate for gate insulator to achieve low equivalent oxide thickness as required for the advanced CMOS technology nodes [13]. However, a fabricated pMOSFET with SiGe S/D is possibly accompanied by the extra amount of process-induced defects, and a gate insulator that is replaced from conventional SiO₂ to HK materials usually causes the changes of trap properties in MOSFET, resulting in the influence on low-frequency noise characterizations. Though low-frequency noise characterizations in pMOSFET with SiGe S/D had been reported [12, 14], low-frequency noise in HK pMOSFET with SiGe S/D is still unclear and needs to be addressed to improve the understanding. In this study, the low-frequency noise characterizations of HK pMOSFET with embedded SiGe S/D are investigated through $1/f$ noise and RTN measurements simultaneously.

2. Experimental

Apart from the S/D engineering, a 28-nm HK first/meta gate last technology was used to prepare the pMOSFET samples for this work. The thickness of the SiO₂ interfacial layer was approximately 1.0–1.1 nm. A total of 20 atomic layer deposition cycles for HfO₂ were deposited on the top of the SiO₂ interfacial layer, and the thickness of all gate stacks was approximately 1.6–1.7 nm. A thin TiN layer was deposited on HfO₂ layer as a capping layer for selective removal of the dummy poly-Si gate [15]. After the S/D activation is annealed, the dummy poly-Si gate was removed and then other metals were deposited to tune the work function and achieve the idea value (5.0–5.2) [16]. The strained-Si HK pMOSFET structure features improvement by optimizing S/D recess shape following an epitaxially grown B-doped SiGe film embedded in the S/D regions with about 30% Ge concentration. Finally, the devices were completed with standard backend processes. The HK device without embedded SiGe was also fabricated and called as control device for comparison. The values of oxide capacitance derived from the equivalent oxide thickness of the CVC program [17] are 2.801×10^{-6} and 2.746×10^{-6} F/cm² for the control and the SiGe S/D devices, respectively. All the pMOSFETs with the gate dimension of $0.25 \mu\text{m} \times 0.04 \mu\text{m}$ (width \times length) were used in this work. Prior to low-frequency noise measurements, the dc characteristics were measured using an Agilent B1500 semiconductor parameter analyzer. The $1/f$ noise measurements were carried out using SR570 low-noise current preamplifiers and an Agilent 35670A dynamic signal analyzer. The pMOSFETs were biased in linear operation ($V_D = -50$ mV) while varying the gate overdrive voltage ($V_G - V_T$) from the subthreshold regime (0.2 V) to the inversion regime (-0.3 V). The RTN measurements were made by waveform generator/fast measurement unit modules based on Agilent B1500 semiconductor parameter analyzer.

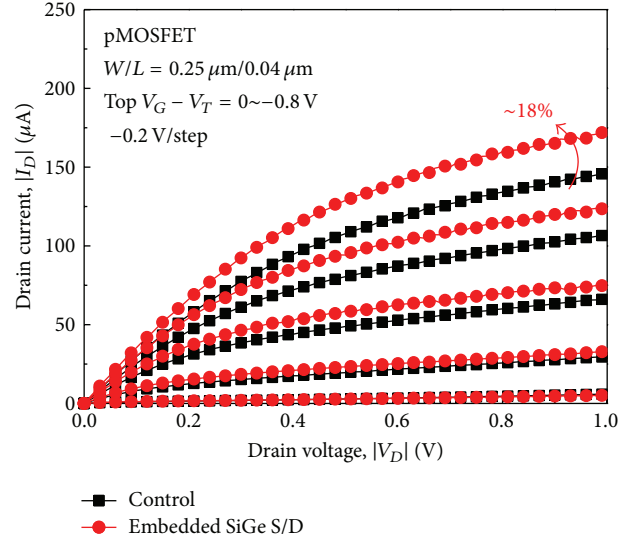


FIGURE 1: The $I_D - V_D$ characteristics for HK pMOSFET with and without embedded SiGe S/D.

3. Results and Discussion

Figure 1 shows the drain current (I_D) as a function of the drain voltage (V_D) for both pMOSFETs. Around 18% I_D enhancement for SiGe S/D device is observed as compared to the control device at the same, $V_G - V_T = -0.8$ V and $V_D = -1.0$ V, which clearly indicates that the embedded SiGe S/D process can efficiently induce compressive strain in the channel. Figure 2 presents the drain current noise spectral density (S_{ID}) versus the frequency for both pMOSFETs taken from the average of six devices biased at different $V_G - V_T$. Both devices show typical $1/f_\gamma$ noise types with the frequency exponent (γ) close to unity. It means that the fluctuations of $1/f$ noise can be attributed to the carrier-number, mobility, or source-drain series-resistance fluctuations. In our devices, the S_{ID} was found to be independent of the V_D , indicating that the $1/f$ noise source is not due to the contact or source-drain series resistance. The normalized drain current noise spectral density (LS_{ID}/I_D^2) and the transconductance to the drain current squared ($(g_m/I_D)^2$) as functions of the I_D are plotted in Figure 3. The LS_{ID}/I_D^2 curves of both devices show fairly good proportionality with $(g_m/I_D)^2$ at the low I_D level, indicating that the carrier number fluctuation dominates the $1/f$ noise, which caused by trapping and releasing of the carrier in the gate stacks [4, 5]. However, the LS_{ID}/I_D^2 curves cannot follow this trend at the high I_D level, which implies a correlated mobility fluctuation was involved [6, 18]. In order to further evaluate the dominant mechanism and parameters of the $1/f$ noise model for both devices, the normalized input-referred voltage noise spectral density (LS_{VG}) as a function of ($V_G - V_T$) is shown in Figure 4. Both devices show two distinct regions in the associated LS_{VG} . In region I ($V_G - V_T \leq -0.1$ V), LS_{VG} is independent of ($V_G - V_T$), which indicates a signature of number fluctuations. In region II ($V_G - V_T > -0.1$ V), a parabolic dependence of LS_{VG} on ($V_G - V_T$) is observed, further confirming that correlated mobility

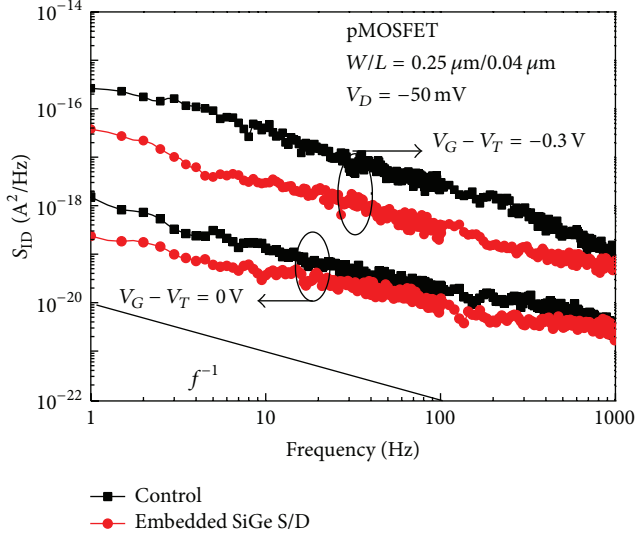


FIGURE 2: Drain current noise spectral density (S_{ID}) versus frequency for HK pMOSFET with and without embedded SiGe S/D.

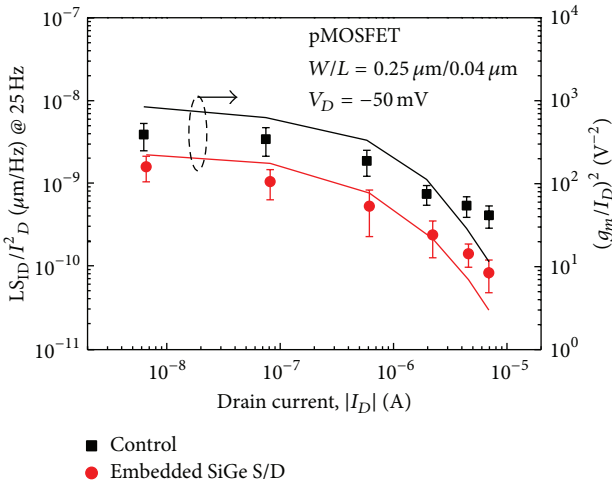


FIGURE 3: Normalized drain current noise spectral density (LS_{ID}/I_D^2) and the transconductance to the drain current squared ($(g_m/I_D)^2$) as functions of drain current for HK pMOSFET with and without embedded SiGe S/D.

fluctuations was involved. These results mean that the main source of $1/f$ noise for both devices can be ascribed to the unified model, which incorporates both the carrier number and the correlated mobility fluctuations. Furthermore, the LS_{VG} can be expressed as [19]

$$LS_{VG} = \frac{q^2 KT}{WC_{ox}^2 f} \lambda N_t [1 + \alpha \mu_0 C_{ox} (V_G - V_T)]^2, \quad (1)$$

where λ is the tunneling attenuation length for channel carriers penetrating into the gate dielectric, N_t is the oxide trap density, α is a scattering coefficient, and μ_0 is the low field mobility. The first term in the parentheses in (1) determines the base LS_{VG} level in our region I and can be described

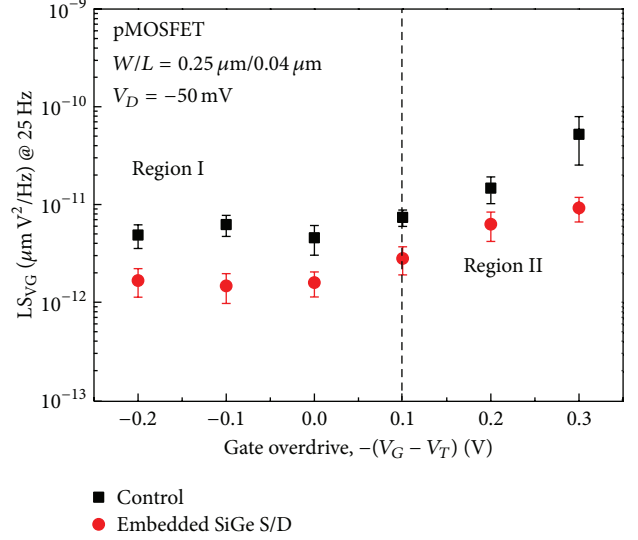


FIGURE 4: Normalized input-referred voltage noise spectral density (LS_{VG}) versus gate overdrive for HK pMOSFET with and without embedded SiGe S/D.

by number fluctuations, in which the LS_{VG} is independent on $V_G - V_T$. The λN_t product is an important parameter related to the base LS_{VG} level. The second term presents the curvature of LS_{VG} versus $V_G - V_T$ in region II and can be described by correlated mobility fluctuations. The curvature of parabola is determined by the $\alpha \mu_0$ product. First, as compared with control device, the reduced LS_{VG} level of the embedded SiGe S/D device implies the reduction of λ or N_t . However, previous literature had reported that SiGe S/D process may lead higher N_t [20, 21]. In other words, it can only be assumed that the reduced λ mainly contributed to the decreased LS_{VG} of SiGe S/D device. The possible mechanism of reduced λ of SiGe S/D device is explained as follows. The uniaxial compressive stress-induced valence band offset and more holes tend to exist in top band. Therefore, the out-of-plane effective mass (m_Z^*) and tunneling barrier height for holes (φ_B) of SiGe S/D device are both larger than those of control one. As shown in Figure 5, an observed smaller gate current density (J_g) in SiGe S/D device confirmed the strain-induced increased m_Z^* and φ_B [22]. The λ is also related to m_Z^* and φ_B by [19, 20]

$$\lambda = \sqrt{\frac{\hbar^2}{2m_Z^* \varphi_B}}, \quad (2)$$

where \hbar is reduced Planck's constant. It suggests that strain-increased m_Z^* and φ_B bring a smaller λ in SiGe S/D device. The relation between the trap depth (X_T) in insulator and λ can be revealed according to an equation as $X_T = \lambda \ln(1/2\pi f \tau_0)$ [23]. The RTN measurement is a useful tool for probing the trap location in MOSFET [24–26]. It will be applied to confirm our observation and assumption of reduced LS_{VG} in the $1/f$ noise measurement. The I_D RTN characteristics of both devices as a function of the time show themselves in the form

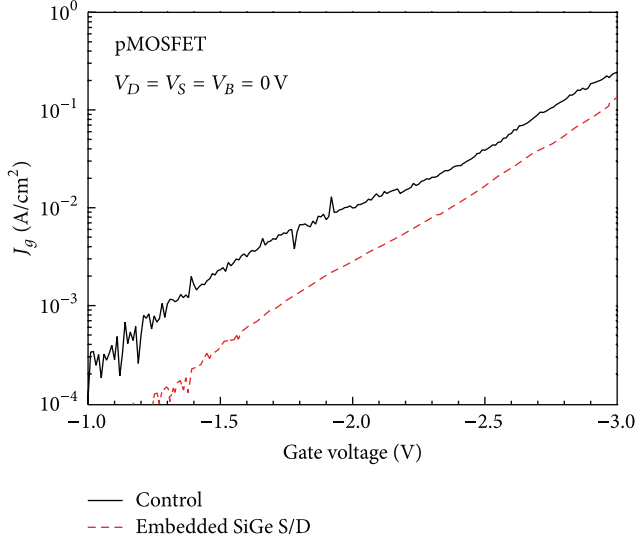


FIGURE 5: The gate current density (J_g) versus gate voltage for HK pMOSFET with and without embedded SiGe S/D.

of switching events between two states (not shown here). These switching events are attributed to trapping/detrapping caused by an individual interface defect. The times in the high- and low-current states correspond to carrier capture and emission, respectively. The extracted mean capture time (τ_c) and mean emission time constant (τ_e) versus ($V_G - V_T$) are both presented in Figure 6. It can be found that the SiGe S/D device has the lower values of τ_c and τ_e and the weak dependence of τ_e on $V_G - V_T$, indicating that the trap position is closer to the insulator/semiconductor interface. Figure 7 shows the dependence of τ_c/τ_e on ($V_G - V_T$) for both devices. From the data obtained for $\ln(\tau_c/\tau_e)$ dependence on gate voltage, the position of the trap into the oxide (X_T) is determined using (3) as follows [14, 25]:

$$\frac{\partial \ln(\tau_c/\tau_e)}{\partial V_{GS}} = \frac{q}{KT} \left(\frac{X_T}{t_{ox}} \right) \left[1 - \frac{KT}{q} \frac{G_m}{|I_{DS}|} \right], \quad (3)$$

where t_{ox} is the oxide thickness, and K is the Boltzmann constant. As expectation, the extracted X_T is 1.68 nm and 1.14 nm for the control device and the SiGe S/D device, respectively. The reduced X_T in SiGe S/D device is in well agreement on the analysis of $1/f$ noise (i.e., reduced λ) and can be ascribed to the strain-induced higher ϕ_B for hole. Therefore, though the gate dielectric quality may be degraded by the SiGe S/D process, the traps far away from insulator/semiconductor interface cannot act for capturing carriers, thanks to the reduced λ , which stemmed from uniaxial compressive strain increasing m_Z^* and ϕ_B . Consequently, the improvement of LS_{VG} level was observed. On the other hand, in region II, the smaller curvature of LS_{VG} of SiGe S/D device indicates the product of $\alpha\mu_0$ is smaller than that of control device, which can be attributed to the strain-induced lower carrier scattering and higher hole mobility at the same time [27, 28]. However, it should be noted that the $1/f$ performance of our HK pMOSFETs will be probably worse than counterparts with traditional SiO_2 insulator [14]. This is owing to the

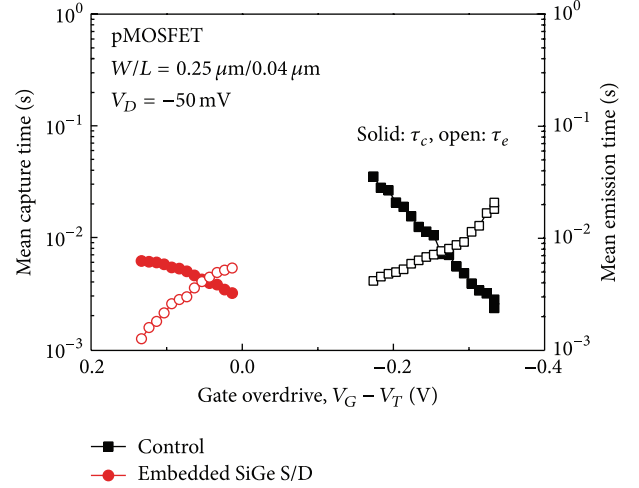


FIGURE 6: Comparison of the capture time (solid) and emission time (open) for HK pMOSFET with and without embedded SiGe S/D.

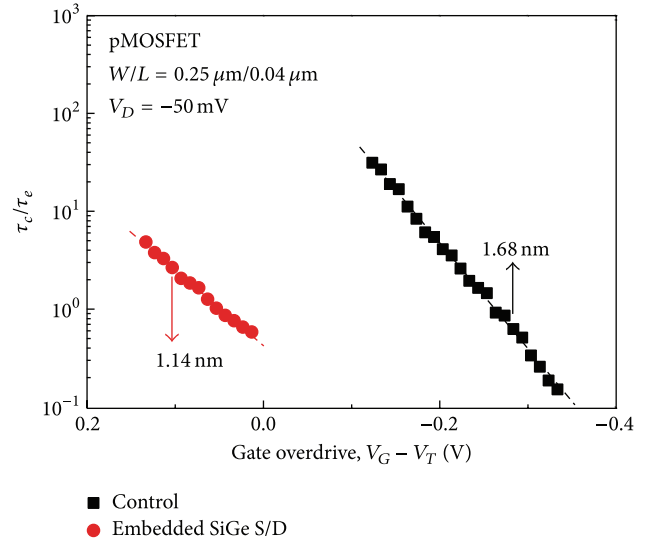


FIGURE 7: Plot of capture time (τ_c) over emission time (τ_e) versus gate overdrive for HK pMOSFET with and without embedded SiGe S/D.

complexity of HK process that led to the higher volume trap densities in gate stacks [29].

4. Conclusions

In this paper, we have investigated the effect of compressive strain on low-frequency noise in HK pMOSFET. Through RTN measurement, we found that the HK pMOSFET with the embedded SiGe S/D has a shorter distance of the oxide trap position from the insulator/semiconductor interface. This is ascribed to the higher ϕ_B and smaller λ for hole stemmed from uniaxial compressive strain-induced bandgap offset. As a result, the improvement of $1/f$ noise is observed. It is clear that the better performance of low-frequency noise

in HK MOSFET device with strain technologies can be expected.

Conflict of Interests

The authors declare that there is no conflict of interests regarding the publication of this paper.

Acknowledgments

The authors would like to thank the Advanced Optoelectronic Technology Center of NCKU for the financial support under Contract HUA103-3-15-051, the National Science Council of Taiwan for the financial support under Contract numbers NSC102-2221-E-006-259 and NSC102-2221-E-230-015, the Bureau of Energy, Ministry of Economic Affairs of Taiwan for the financial support under Contract number 102-E0603, and UMC staffs for their helpful support.

References

- [1] Y. Nemirovsky, I. Brouk, and C. G. Jakobson, "1/f noise in CMOS transistors for analog applications," *IEEE Transactions on Electron Devices*, vol. 48, no. 5, pp. 921–927, 2001.
- [2] Y. Yasuda and C. Hu, "Effect of fluorine incorporation on 1/f noise of HfSiON FETs for future mixed-signal CMOS," in *Proceedings of the International Electron Devices Meeting (IEDM '06)*, pp. 1–4, 2006.
- [3] K. K. Hung, P. K. Ko, C. Hu, and Y. C. Cheng, "Unified model for the flicker noise in metal-oxide-semiconductor field-effect transistors," *IEEE Transactions on Electron Devices*, vol. 37, no. 3, pp. 654–665, 1990.
- [4] L. K. J. Vandamme, X. Li, and D. Rigaud, "1/f noise in MOS devices, mobility or number fluctuations?" *IEEE Transactions on Electron Devices*, vol. 41, no. 11, pp. 1936–1945, 1994.
- [5] G. Ghibaudo and T. Bouchacha, "Electrical noise and RTS fluctuations in advanced CMOS devices," *Microelectronics Reliability*, vol. 42, no. 4–5, pp. 573–582, 2002.
- [6] L. K. J. Vandamme and F. N. Hooge, "What do we certainly know about 1/f noise in MOSTs?" *IEEE Transactions on Electron Devices*, vol. 55, no. 11, pp. 3070–3085, 2008.
- [7] C. Hu, "Device challenges and opportunities," *Dig. Tech. Pap. Symp. VLSI Technology*, p. 4, 2004.
- [8] T.-J. Wang, C.-H. Ko, H.-N. Lin et al., "Investigation of metallized source/drain extension for high-performance strained NMOSFETs," *IEEE Transactions on Electron Devices*, vol. 55, no. 11, pp. 3221–3226, 2008.
- [9] S. E. Thompson, G. Sun, Y. S. Choi, and T. Nishida, "Uniaxial-process-induced Strained-Si: extending the CMOS roadmap," *IEEE Transactions on Electron Devices*, vol. 53, no. 5, pp. 1010–1020, 2006.
- [10] E. Simoen, P. Verheyen, A. Shickova, R. Loo, and C. Claeys, "On the low-frequency noise of pMOSFETs with embedded SiGe source/drain and fully silicided metal gate," *IEEE Electron Device Letters*, vol. 28, no. 11, pp. 987–989, 2007.
- [11] C. W. Kuo, S. L. Wu, S. J. Chang, H. Y. Lin, Y. P. Wang, and S. C. Hung, "Investigation of interface characteristics in strained-Si nMOSFETs," *Solid-State Electronics*, vol. 53, no. 8, pp. 897–900, 2009.
- [12] B. C. Wang, S. L. Wu, C. W. Huang et al., "Correlation between random telegraph noise and 1/f noise parameters in 28-nm pMOSFETs with tip-shaped SiGe source/drain," *IEEE Electron Device Letters*, vol. 33, no. 7, pp. 928–930, 2012.
- [13] H.-S. Jung, J.-H. Lee, S. K. Han et al., "A highly manufacturable MIIPS (Metal Inserted Poly-Si Stack) technology with novel threshold voltage control," in *Proceedings of the Symposium on VLSI Technology*, pp. 232–233, June 2005.
- [14] B. C. Wang, S. L. Wu, C. W. Huang et al., "Characterization of oxide traps in 28nm p-type metal-oxide-semiconductor field-effect transistors with tip-shaped SiGe source/drain based on random telegraph noise," *Japanese Journal of Applied Physics*, vol. 51, Article ID 02BC11, 2012.
- [15] L.-Å. Ragnarsson, Z. Li, J. Tseng et al., "Ultra low-EOT (5 Å) gate-first and gate-last high performance CMOS achieved by gate-electrode optimization," in *Proceedings of the International Electron Devices Meeting (IEDM '09)*, pp. 1–4, December 2009.
- [16] J. K. Schaeffer, S. B. Samavedam, D. C. Gilmer et al., "Physical and electrical properties of metal gate electrodes on HfO₂ gate dielectrics," *Journal of Vacuum Science and Technology B*, vol. 21, no. 1, pp. 11–17, 2003.
- [17] J. R. Hauser and K. Ahmed, "Characterization of ultra-thin oxides using electrical C-V and I-V measurements," in *Proceedings of the International Conference on Characterization and Metrology for ULSI Technology*, p. 235, 1998.
- [18] P. C. Huang, S. L. Wu, S. J. Chang et al., "Characteristics of Si/SiO₂ interface properties for CMOS fabricated on hybrid orientation substrate using Amorphization/Templated Recrystallization (ATR) method," *IEEE Transactions on Electron Devices*, vol. 58, no. 6, pp. 1635–1642, 2011.
- [19] C. W. Kuo, S. L. Wu, S. J. Chang, Y. T. Huang, Y. C. Cheng, and O. Cheng, "Impact of stress-memorization technique induced-tensile strain on low frequency noise in n-channel metal-oxide-semiconductor transistors," *Applied Physics Letters*, vol. 97, no. 12, Article ID 123501, 2010.
- [20] J. J. Y. Kuo, W. P. N. Chen, and P. Su, "Impact of uniaxial strain on low-frequency noise in nanoscale PMOSFETs," *IEEE Electron Device Letters*, vol. 30, no. 6, pp. 672–674, 2009.
- [21] C. Y. Cheng, Y. K. Fang, J. C. Hsieh et al., "Investigation and localization of the SiGe source/drain (S/D) strain-induced defects in PMOSFET with 45-nm CMOS technology," *IEEE Electron Device Letters*, vol. 28, no. 5, pp. 408–411, 2007.
- [22] X. Yang, Y. Choi, T. Nishida, and S. E. Thompson, "Gate direct tunneling currents in uniaxial stressed MOSFETs," in *Proceedings of the International Workshop on Electron Dev and Semiconductor Technology*, pp. 149–152, 2007.
- [23] M. V. Haartman and M. Östling, *Low-Frequency Noise in Advanced MOS Devices*, Springer, Heidelberg, Germany, 2007.
- [24] H. F. Chiu, S. L. Wu, Y. S. Chang et al., "Low surface traps induced noise ZrZnO thin-film transistor using field-plate metal technology," *Japanese Journal of Applied Physics*, vol. 52, no. 9, Article ID 04CC22, 2013.
- [25] B. C. Wang, S. L. Wu, Y. Y. Lu et al., "Characterization of oxide traps in 28nm n-type metal-oxide-semiconductor field-effect transistors with different uniaxial tensile stresses utilizing Random telegraph noise," *Japanese Journal of Applied Physics*, vol. 52, Article ID 04CC24, 2013.
- [26] S. C. Tsai, S. L. Wu, P. C. Huang et al., "Investigation of Trap Properties of Hf_{0.83}Zr_{0.17}O₂ High-k Gate Stack pMOSFETs by Low-frequency (1/f) Noise and RTN Analyses," in *International Workshop on Dielectric Thin Films for Future Electron Devices Science and Technology*, p. 87, 2013.

- [27] V. Vartanian, S. Zollner, A. V.-Y. Thean et al., "Metrology challenges for 45-nm strained-Si device technology," *IEEE Transactions on Semiconductor Manufacturing*, vol. 19, no. 4, pp. 381–388, 2006.
- [28] S. I. Takagi, J. Koga, and A. Toriumi, "Subband structure engineering for processing-induced uniaxial vs. substrate-induced biaxial stressed Si and Ge channel MOSFETs," in *Proceedings of the International Electron Devices Meeting (IEDM '97)*, p. 219, 1997.
- [29] P. Srinivasan, E. Simoen, L. Pantisano, C. Claeys, and D. Misra, "Low-frequency (1f) noise performance of n- and p-MOSFETs with poly-SiHf-based gate dielectrics," *Journal of the Electrochemical Society*, vol. 153, no. 4, pp. G324–G329, 2006.

Research Article

Texture-Etched SnO₂ Glasses Applied to Silicon Thin-Film Solar Cells

Bing-Rui Wu,¹ Sin-Liang Ou,¹ Shih-Yung Lo,¹ Hsin-Yuan Mao,¹
Jhen-Yu Yang,¹ and Dong-Sing Wu^{1,2}

¹ Department of Materials Science and Engineering, National Chung Hsing University, 250 Kuo Kuang Road, Taichung 40227, Taiwan

² Department of Materials Science and Engineering, Da-Yeh University, Changhua 51591, Taiwan

Correspondence should be addressed to Dong-Sing Wu; dsw@dragon.nchu.edu.tw

Received 13 December 2013; Revised 8 February 2014; Accepted 9 February 2014; Published 18 March 2014

Academic Editor: Sheng-Po Chang

Copyright © 2014 Bing-Rui Wu et al. This is an open access article distributed under the Creative Commons Attribution License, which permits unrestricted use, distribution, and reproduction in any medium, provided the original work is properly cited.

Transparent electrodes of tin dioxide (SnO₂) on glasses were further wet-etched in the diluted HCl:Cr solution to obtain larger surface roughness and better light-scattering characteristic for thin-film solar cell applications. The process parameters in terms of HCl:Cr mixture ratio, etching temperature, and etching time have been investigated. After etching process, the surface roughness, transmission haze, and sheet resistance of SnO₂ glasses were measured. It was found that the etching rate was increased with the additions in etchant concentration of Cr and etching temperature. The optimum texture-etching parameters were 0.15 wt.% Cr in 49% HCl, temperature of 90°C, and time of 30 sec. Moreover, silicon thin-film solar cells with the p-i-n structure were fabricated on the textured SnO₂ glasses using hot-wire chemical vapor deposition. By optimizing the texture-etching process, the cell efficiency was increased from 4.04% to 4.39%, resulting from the increment of short-circuit current density from 14.14 to 15.58 mA/cm². This improvement in cell performances can be ascribed to the light-scattering effect induced by surface texturization of SnO₂.

1. Introduction

Owing to the advantages consisting of low cost, easy fabrication, and environmental friendliness, silicon (Si) is a very promising material for the photovoltaic applications [1, 2]. Thin-film solar cells based on amorphous silicon (a-Si) or microcrystalline silicon (μ c-Si) are the most popular products applied to the building-integrated photovoltaics and consumer electronics. Transparent conductive oxide (TCO) films are usually used as the front electrode of thin-film solar cells. For a transparent electrode, the requirements of TCO films are a low sheet resistance (R_{sheet}) to minimize the current loss, a low contact resistance to semiconductor layers, and a high transmission of incident light. To completely utilize the incident light, an important technique of the so-called light trapping has been developed using a TCO with suitable surface texture. Schematic diagrams of the light-scattering effects in roughened and smooth TCO glasses are shown in Figure 1. It was indicated that a specific design of TCO films plays an important role in enhancing the performances of

thin-film solar cells. A surface-textured TCO can scatter the light greatly and increase the effective optical path length within the active layers [3–6]. A rough TCO film also ensures that the roughness is copied by the film deposited on it, so that the back metal electrode produces an increased scattering of reflected light. Therefore, this would improve both the optical absorption and current density in thin-film solar cells. After that, various randomly textured TCO substrates have been proposed to increase the light scattering. As-deposited and postchemical textured TCOs are both useful to achieve the rough substrates. The common TCO materials applied to thin-film solar cells consist of tin dioxide (SnO₂) [6] and zinc oxide (ZnO) [7, 8]. The great majority of glass-based Si thin-film modules are prepared on the fluorine-doped SnO₂ (SnO₂:F) glasses due to their intrinsic rough surface [4, 5]. Moreover, the directly deposited or texture-etched ZnO is another attractive method for the fabrication of rough TCO substrate [9–12]. By using the texture-etched ZnO, the quantum efficiency of thin-film solar cells over the whole spectral range can be increased [11, 12]. A further

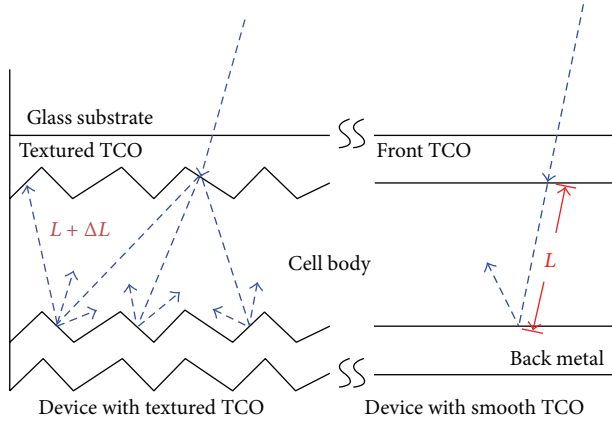
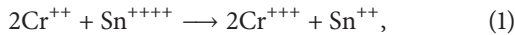


FIGURE 1: Schematic diagrams of the light-scattering effects in roughened and smooth TCO glasses.

improvement in the reduction of free carrier absorption losses in the red/IR and absorption around the optical edge of ZnO in the blue/UV region can be achieved [13].

SnO_2 , one of the most common TCO films, is usually prepared by atmospheric pressure chemical vapor deposition (APCVD) with a natively textured surface [14]. Asahi type-U glass is a worldwide TCO substrate for thin-film solar cell industry, which is a natively textured SnO_2 glass with the great light scattering of 10% in transmission haze ratio. A method to create a pattern or to remove the SnO_2 layer by wet etching has been reported [15]. The etchant of this method includes 3 liters of 50% HCl and 20 g of chromium metal (Cr). The mixture is heated to 90°C with constant stirring to dissolve the Cr. The overall reaction sequence of the etching treatment is given by the following equation:



where the SnO_2 is stannic oxide (Sn^{++++}) and is transferred to stannous oxide (Sn^{++}) after the etching reaction. The stannous oxide can be soluble in the acid solution to complete the etching reaction.

In this study, we choose the mass-produced SnO_2 soda glasses as substrates which were usually used for the building-integrated photovoltaic applications. Then the wet chemical texturization was performed by using the diluted HCl:Cr solution to reach larger surface roughness and better light-scattering properties for thin-film solar cell applications. The etching parameters, such as etchant concentration, etching temperature, and etching time (t_{etch}), were investigated. Moreover, Si thin-film solar cells with p-i-n structure on various textured SnO_2 glasses were fabricated and their characteristics were also studied.

2. Experimental Procedure

The 3-mm thick soda glasses with APCVD-deposited 600 nm thick SnO_2 films were chosen as the substrates. These SnO_2 glasses showed the high conductivity of 12–14 Ω/\square and high transparency of >85% in the 400–800 nm wavelength range.

The roughness and transmission haze of SnO_2 films were about 260 nm and 7%, respectively. To obtain the textured surface, the SnO_2 glasses were etched in a SnO_2 etchant. Various Cr concentrations from 0.05 to 1 wt.% were mixed into the diluted HCl (49%) to prepare the SnO_2 etchants. The etching temperature was varied from room temperature to 100°C . Moreover, the t_{etch} was increased from 1 to 300 sec. By changing these parameters, the effects of etching conditions on the optoelectronic performances of SnO_2 films were investigated in detail. The ability of the textured SnO_2 films to scatter light can be expressed by the transmission haze ratio (H_t):

$$\text{Transmission haze } (H_t) = \frac{\text{Diffuse transmittance}}{\text{Total transmittance}}, \quad (2)$$

where the transmission haze is defined as the percentage of transmitted light deviated from the incident beam by more than 2.5° from the normal incident beam. In this study, the total transmittance was measured by using an integrating sphere. The diffuse transmittance was calculated by the difference between the total and direct transmittance. Considering the rough surface of SnO_2 , the etching depth was measured repeatedly by an α -step surface profiler to determine the average etching rate. Field-emission scanning electron microscope (FE-SEM, JEOL JSM-6700F) was used to observe the SnO_2 morphology. An atomic force microscopy (AFM, Agilent 5400) was applied for the measurement of surface roughness. The R_{sheet} of textured SnO_2 film was investigated by using the four-point probe method.

Subsequently, Si thin-film solar cells were fabricated on the textured SnO_2 films. The fabrication process can be divided into three main steps: SnO_2 texture etching, deposition of the Si p-i-n structure, and formation of the back electrode. The p-type, intrinsic and n-type Si layers in this study were prepared in a single chamber hot-wire chemical vapor deposition (HWCVD) system. The HWCVD technique is widely employed as the fabrication of Si-based thin films consisting of a-Si [16], $\mu\text{c-Si}$ [17], doped Si [18], and silicon carbide (SiC) [19]. Due to the unique advantages including crystalline film deposition at low substrate temperature, high deposition rate, and high gas utilization in HWCVD [20], it has attracted great attention for its potential applications in thin-film solar cells [21, 22] and transistors [23, 24]. In our previous studies, HWCVD was used to deposit the Si-based films for various purposes, such as aluminum induced crystallization [25], n-type $\mu\text{c-Si}$ [26], p-type window layers (nanocrystalline Si [27] and SiC [28]), and heterojunction solar cells [29]. Before loading the SnO_2 substrate into HWCVD system, the chamber was firstly treated using the atomic H generated from H_2 gas [30]. Table 1 summarizes the process parameters of HWCVD-deposited p-, i-, and n-type Si and buffer layers. The key parameters of Si film deposition include a wire temperature of 1700°C , a substrate temperature of 300°C , and the working pressure of 100 mTorr. Silane (SiH_4) was applied to the source gas with flow rate (Φ_{SiH_4}) of 2 sccm. Phosphine (PH_3 , 1% in H_2) and diborane (B_2H_6 , 1% in H_2) were used as the dopant gases with flow rates (Φ_{dopant}) of 18 and 20 sccm, respectively, to prepare n-type and p-type microcrystalline Si layers, which were reported

TABLE 1: Deposition parameters and properties of p-, i-, n-type Si and buffer layers by HWCVD.

Film	Unit	p-layer	Buffer	i-layer	n-layer
Filament temperature	°C	1700	1700	1700	1700
Substrate temperature	°C	300	300	300	300
Pressure	mTorr	100	100	100	100
Gas flow rate (Φ)	sccm	$\Phi_{\text{SiH}_4} = 2$ $\Phi_{\text{B}_2\text{H}_6} = 20$	$\Phi_{\text{SiH}_4} = 1$ $\Phi_{\text{CH}_4} = 1$ $\Phi_{\text{B}_2\text{H}_6} = 3$ $\Phi_{\text{H}_2} = 20$	$\Phi_{\text{SiH}_4} = 2$	$\Phi_{\text{SiH}_4} = 2$ $\Phi_{\text{PH}_3} = 18$
Energy gap	eV	1.97	2.18	1.68	1.78
Crystalline fraction	%	67	59	Amorphous	57
Deposition rate	nm/sec	0.201	0.208	0.262	0.213
Hall concentration	cm^{-3}	1×10^{20}	5×10^{19}	—	4×10^{19}

elsewhere [25, 27–29]. Some characteristics consisting of energy gap (by Tauc plot), crystalline fraction (by Raman spectroscopy), deposition rate (by profilometer), and Hall concentration (by Hall measurement) of these films were also exhibited in Table 1. The detailed experimental procedures and similar discussions in these films characteristics were presented in our previous works [25, 27–29]. Between the p- and i-layers, a 10 nm thick p-type microcrystalline SiC buffer layer with energy gap of 2.18 eV was deposited for better band structure. The main benefit of this buffer layer originated from its effect on the electric field distribution, which minimized the recombination near the p/i interface [31]. Compared to the literatures [32, 33], the energy gap of our buffer was in good agreement with that of crystalline cubic silicon carbide (3C-SiC). Details of the HWCVD-deposited SiC were reported in our previous work [28]. The thicknesses of p-, i-, and n-layers were 30, 500, and 50 nm, respectively. Such an insufficient i-layer thickness of 500 nm was used to induce an incomplete absorption. It can provide an investigation of the light-scattering and absorption effects in a limited thickness of absorber layer. After depositing the p-i-n structure, the 500 nm thick Ag and 1- μm thick Al layers were grown sequentially as the back electrode by electron-beam evaporation and then annealed at 500°C to achieve an ohmic contact. Finally, Si thin-film solar cells were fabricated with the structure of glass/textured SnO_2 /p-i-n Si layers/Ag-Al and the cell size was $5 \times 5 \text{ mm}^2$. Device performances consisting of current density voltage (J - V) and external quantum efficiency (EQE) of solar cells were measured by Keithley 2400 SourceMeter (Sciencetech, model SS150W) with a one-sun AM1.5G light source (100 mW/cm^2) at room temperature.

3. Results and Discussion

This study investigated the improvement in optical characterization of SnO_2 films with the optimized textured surface to enhance the spectral response and efficiency of thin-film solar cells. In order to control the etching rate, various SnO_2 etchants and etching temperatures were used. As mentioned above, the etchants with various Cr concentrations from 0.05 to 1 wt.% were employed to etch the SnO_2 films. When the

Cr concentration was less than 0.15 wt.%, a poor etching rate approaching to no etching was found on the film surface. On the other hand, the etching reaction was violent for the Cr concentration more than 0.45 wt.%, leading to a low reproduction in the textured surface. The stable and high reproducible etching reactions have taken place by using the etchants with Cr concentration of 0.15–0.45 wt.%. Therefore, the etchants with Cr concentrations of 0.15, 0.3, and 0.45 wt.% denoted as etchants A, B, and C, respectively, were chosen to further etch the SnO_2 films with various etching conditions (temperature and time). Figure 2 shows the average etching rates of these etchants at various etching temperatures. It was found that the etching reaction appeared when the process temperature was higher than 60°C. Etching rates of these three etchants were all increased with increasing the temperature. As the temperature was increased from 60 to 100°C, the etching rates of etchants A, B, and C rose from 31.4, 74.5, and 89.2 to 121, 158, and 188.6 nm/min, respectively. The higher Cr concentration and temperature would result in a higher etching rate.

Various temperatures and t_{etch} were carried out for etchants A, B, and C to optimize the roughness and H_t properties of SnO_2 films. After comparing all etching results, the higher root-mean-square (RMS) roughnesses and H_t values were observed at 90, 80, and 80°C for etchants A, B, and C, respectively. The RMS roughnesses of SnO_2 films etched in these three etchants with their optimum temperatures at various t_{etch} were shown in Figure 3. Several t_{etch} of 1, 5, 15, 30, 60, 120, and 300 sec were used in the etching treatments. From the results, the RMS roughness of SnO_2 with these three etchants showed the similar trend to each other. In the range of 1–120 sec, the RMS roughness of SnO_2 was firstly increased and then decreased. Because the etching reaction was started at the grain boundaries of film, it induced an increment in RMS in the beginning. The following decrease in RMS with increasing the t_{etch} to 120 sec was probably ascribed to the isotropic etching in some sharp regions of the grains, causing a smoother surface. After etching for 300 sec, we found that the RMS was increased again. It could result from the severe damage on SnO_2 surface during long-time etching. For the changes in surface morphology mentioned above, it will be displayed later in SEM images. The highest roughness value

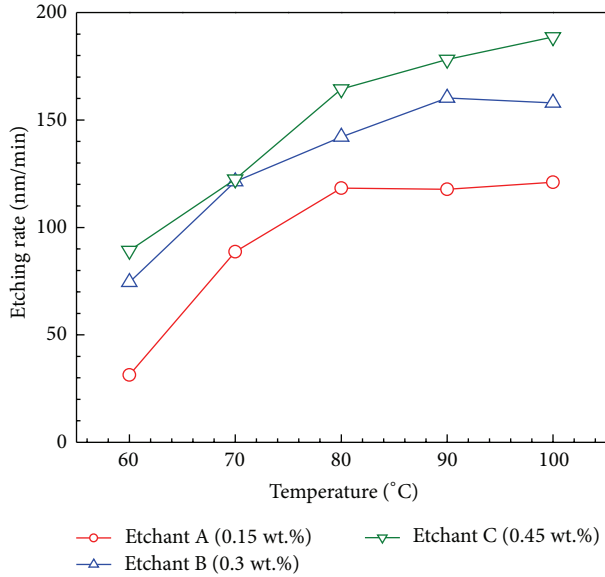


FIGURE 2: Etching rates for SnO₂ films in etchants A, B, and C as a function of the etching temperature.

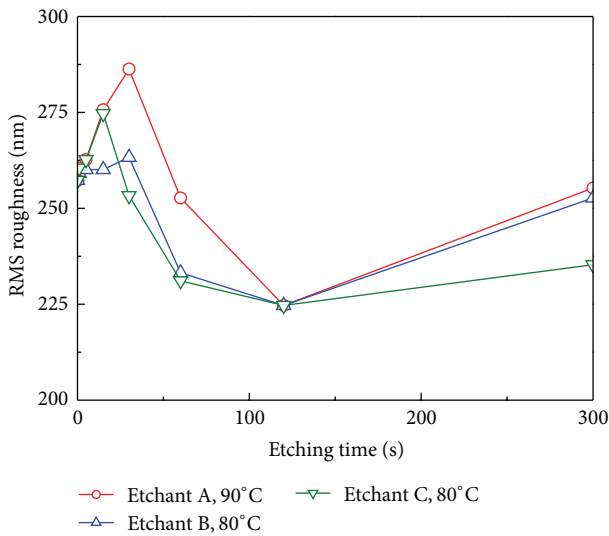


FIGURE 3: Surface RMS roughnesses of etched SnO₂ glasses in etchants A, B, and C with their optimum temperatures as a function of etching time.

of 286.3 nm was obtained using the etchant A for 30 sec. For etchants B and C, the highest roughness values of 263.3 and 274.7 nm were found after etching for 30 and 15 sec, respectively.

The average H_t values (@ 550 nm) of SnO₂ glasses etched by various etchants as a function of t_{etch} were shown in Figure 4. It was found that the H_t curves exhibited the similar trends to the results of RMS roughness displayed in Figure 3. In the case of sample treated with etchant A, the H_t increased with an increment of t_{etch} from 1 to 30 sec. Further, increasing the t_{etch} from 30 to 300 sec, the H_t firstly decreased and then increased. Two relatively high H_t values of 8.38% and 9.13%

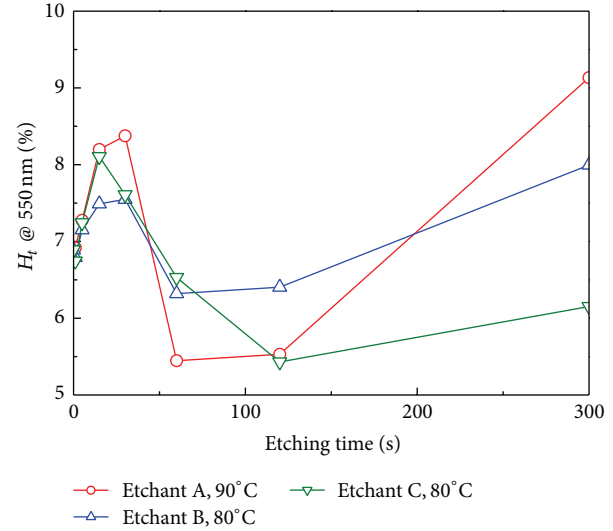


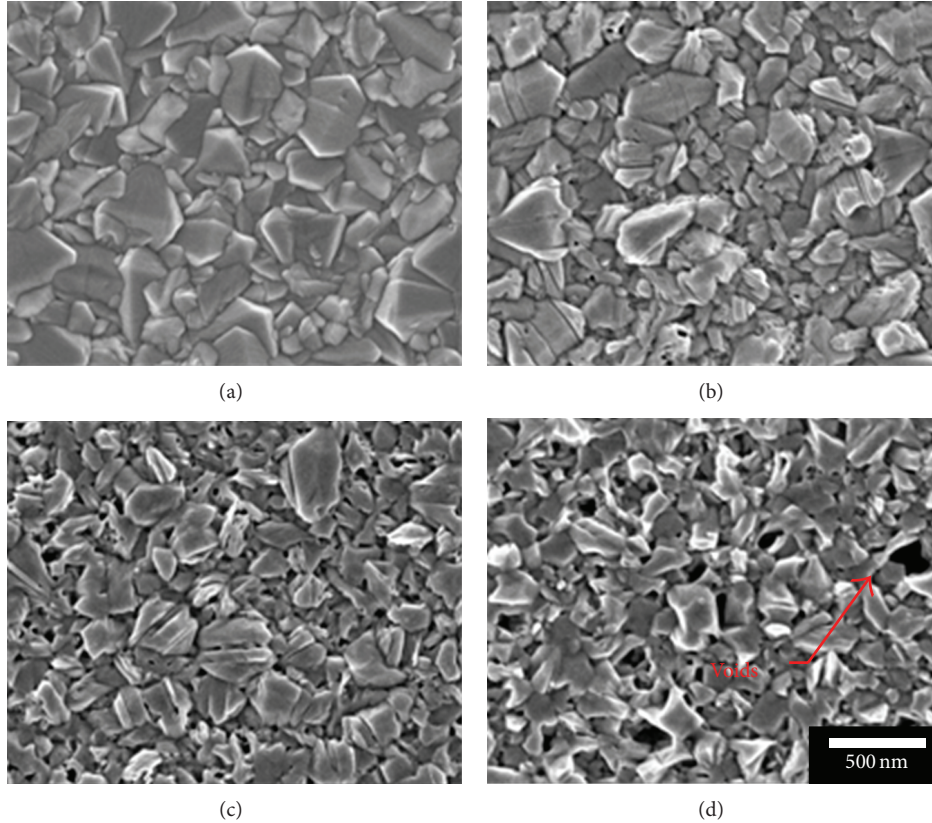
FIGURE 4: Transmission haze (@ 550 nm) of etched SnO₂ glasses in etchants A, B, and C as a function of etching time.

were observed at the t_{etch} of 30 and 300 sec, respectively. Moreover, for the uses of etchants B and C to our samples, the results demonstrated the similar tendency to each other. The highest H_t of samples treated with etchants B and C were 7.55 and 8.1% after etching for 30 and 15 sec, respectively.

The etched SnO₂ surface was visualized by the FE-SEM and AFM. Figures 5(a), 5(b), 5(c), and 5(d) showed the SEM images of SnO₂ etched in the etchant A at 90 °C for 0, 30, 120, and 300 sec, respectively. The AFM images of same samples were shown in Figures 6(a)–6(d). The RMS and R_{sheet} of original SnO₂ are measured to be 260 nm and 13.2 Ω/□, respectively. As displayed in Figures 5(c) and 6(c), some small holes appeared in the SnO₂ grains as the t_{etch} was increased to 120 sec. For the 300 sec etching sample, the size of holes was grown up to several hundreds of nanometers as shown in Figures 5(d) and 6(d). In comparison to the nonetching sample, the grain shapes of SnO₂ with etching for 30 sec were clearer because the etching usually started at the grain boundaries. After etching for 120 sec, the grains became smoother owing to the isotropic nature of wet etching. Nevertheless, with increasing the t_{etch} to 300 sec, the formation of voids can be observed. This indicated that the SnO₂ suffered long-time damage by wet chemical etching. These voids may lead to more large-angle scattering light. This could be the reason why these samples with the t_{etch} of 300 sec exhibited a larger increment in H_t than that in RMS roughness. These surface morphologies of SnO₂ films with the t_{etch} from 0 to 300 sec can reflect the various degrees of surface roughness, which is in good agreement with the results shown in Figure 3. The R_{sheet} values of SnO₂ etched for 30, 120, and 300 sec were 13.9, 15.1, and 27.6 Ω/□, respectively. Apparently, the R_{sheet} increased with increasing the t_{etch} and hence induced a detrimental effect on the application of thin-film solar cells. As the etching process was performed for 300 sec, there existed a rapid increase in R_{sheet} due to the chemical damages caused by the long-time etching, as shown

TABLE 2: Light J - V parameters of silicon p-i-n thin-film solar cells deposited on texture-etched SnO_2 with various t_{etch} .

t_{etch} (s)	H_{t550} (%)	R_{sheet} (Ω/\square)	η (%)	V_{oc} (V)	J_{sc} (mA/cm^2)	FF (%)	R_s (Ω)
Original	6.9	13.2	4.04	0.52	14.14	54.94	11.06
30	8.38	13.9	4.39	0.52	15.58	54.24	10.88
120	5.53	15.1	4.04	0.50	16.22	49.78	11.76
300	9.13	27.6	3.48	0.49	14.99	47.41	17.66

FIGURE 5: FE-SEM images of SnO_2 etched in the etchant A at 90°C for (a) 0, (b) 30, (c) 120, and (d) 300 sec.

in Figures 5(d) and 6(d). Based on the H_t , R_{sheet} , and surface roughness of etched SnO_2 , the t_{etch} of 30 sec could be an optimum condition in this study.

In order to investigate the improvement in light scattering, the 500 nm thick a-Si films were deposited upon SnO_2 glasses with and without texture etching. For the measurements of total transmittance (T) and total reflectance (R) by the integrating sphere, the samples were illuminated from the glass side. A calculated value of $1-R-T$ represented the absorbance of this SnO_2 glass with a 500 nm thick a-Si layer. The value indicated the real quantity of light trapping or light harvesting ability for 500 nm thick a-Si on a rough SnO_2 substrate. It also revealed that the effect of light scattering was modified by wet texturization. The $1-R-T$ and H_t values of original and etched SnO_2 glasses were shown in Figure 7. We found that both $1-R-T$ and H_t of etched SnO_2 for 30 sec were higher than those of the other samples in the visible range of 400–800 nm. It proved that there was an increment in diffuse transmittance for surface-roughened SnO_2 glass. In

addition, the absorbance of 500 nm thick a-Si for incident light was improved via the scattering effect. The effects of texturization on optical characteristics were similar to the results of previous research [34]. From our observation, the sample which used etched SnO_2 with etchant A at 90°C for 30 sec has higher $1-R-T$ value than that of the others. Thus, we chose the etchant A with the optimum conditions (etching temperature of 90°C and t_{etch} of 30 sec) as the standard texture-etching process.

To demonstrate the suitability of textured SnO_2 glasses for thin-film solar cell applications, p-i-n solar cells have been fabricated by HWCVD on original and etched SnO_2 glasses with a 500 nm thick intrinsic absorber layer. Table 2 summarizes the performances of the p-i-n solar cells deposited on SnO_2 glasses etched with various t_{etch} . From the measurements shown in Table 2, there existed an increment in R_{sheet} of TCO from 13.2 to 27.6 Ω/\square as the t_{etch} was increased from 0 to 300 sec. It can be expected that the series resistance of cell would increase with increasing the R_{sheet} of TCO, further

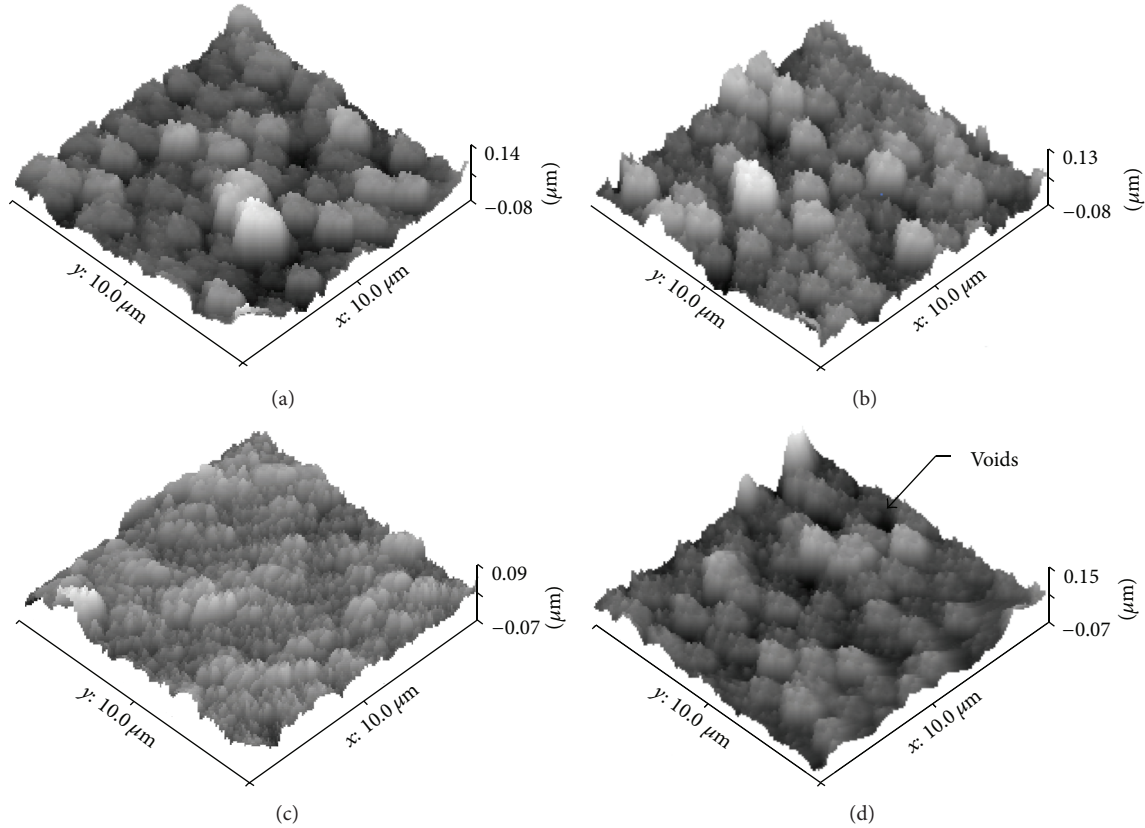


FIGURE 6: AFM images of SnO₂ etched in the etchant A at 90°C for (a) 0, (b) 30, (c) 120, and (d) 300 sec.

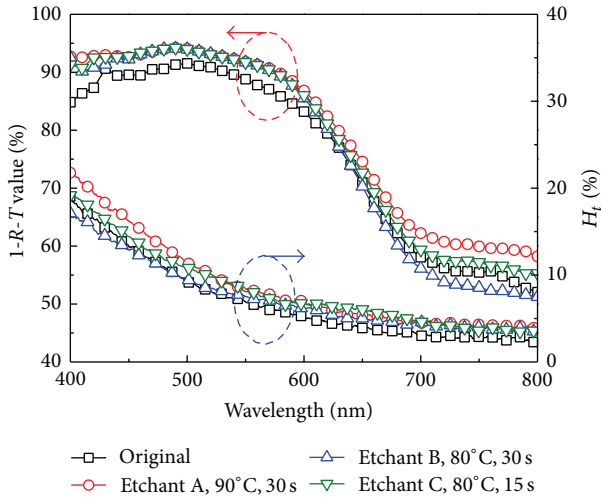


FIGURE 7: Transmission haze and 1-R-T values of original and etched SnO₂ glasses in the visible range of 400–800 nm.

leading to the decreases in fill factor (FF) and conversion efficiency (η). In fact, the cell performances in our work are mainly influenced by both R_{sheet} and roughness of TCO. Generally, the short-circuit current density (J_{sc}) of cell can be enhanced by using textured TCO substrate because of the

light scattering generated from the rough surface. However, it also results in the deteriorations in open-circuit voltage (V_{oc}) and FF of cell [35]. Therefore, it is important to control an acceptable degree of substrate texturization, which can both improve the J_{sc} and induce the minimum deteriorations in V_{oc} and FF of cell. As shown in Table 2, the V_{oc} and FF values of cell with substrate etching for 30 sec were similar to those with nonetched substrate. Nevertheless, with the assistance of etching process for 30 sec to the SnO₂ substrate, the J_{sc} was increased from 14.14 to 15.58 mA/cm², while the cell efficiency was increased from 4.04% to 4.39%. It confirmed that the t_{etch} of 30 sec was indeed the optimum parameter for substrate texturization in our study. On the other hand, although the J_{sc} of the samples with substrate etching for 30 and 120 sec were close to each other, there was a considerable difference in their FF values. It can be seen that the cell using long-time (120 sec) etched substrate had the worse FF value of 49.78% than that with substrate etching for 30 sec (54.24%). The deteriorated FF value in the sample with substrate etching for 120 sec could be attributed to the higher R_{sheet} and lower surface roughness of TCO. This revealed that the better light trapping which resulted from the rougher SnO₂ surface (wet etching for 30 sec) can lead to the highest current density of cell device. Moreover, the series resistances (R_{s}) of 11.06, 10.88, 11.76, and 17.66 Ω were also given in Table 2 for the samples with non-, 30 sec, 120 sec, and 300 sec etched SnO₂ substrates, respectively. It was obvious that the much higher

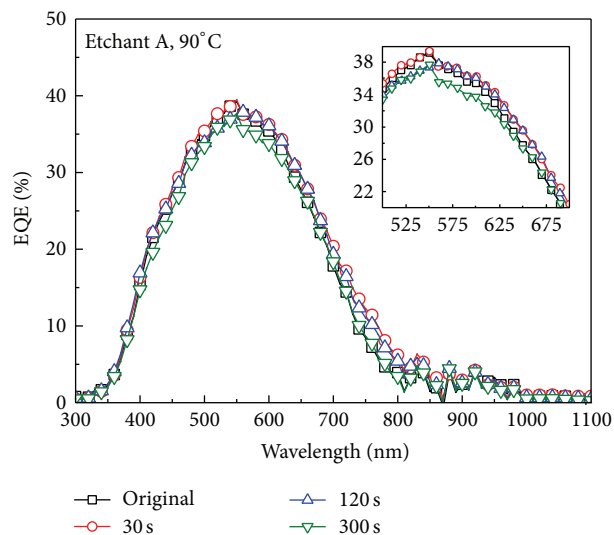


FIGURE 8: EQE characteristics of Si p-i-n solar cells deposited on SnO₂ glasses with original and textured (etched in etchant A at 90°C for 30–300 sec) surfaces as a function of measured wavelength. The inset is an enlarged view of Figure 8 focused on the measured wavelength region of 500–700 nm.

R_s in the sample with the t_{etch} of 300 sec was attributed to the long-time etching, resulting in more severe damage on SnO₂ surface.

Figure 8 shows the EQE characteristics of solar cells deposited on the original and textured SnO₂ glasses. As compared with the solar cell on original SnO₂ glass, the device prepared on the 30 sec etched SnO₂ exhibited an increase in EQE for almost full range from 300 to 1100 nm. As can be known, the elevation in EQE can enhance the J_{sc} performance directly. An enlarged view of Figure 8 focused on the measured wavelength region of 500–700 nm was displayed in the inset. We can find that the cell with 30 sec etched substrate presented a higher EQE value in almost full wavelength ranging from 300 to 900 nm. However, based on the previous study, a-Si solar cell has a low absorption around the wavelength of 800 nm [36]. Therefore, it can be assumed that the main contribution in EQE for textured cell happened from near-ultraviolet region to red region (300–750 nm), which was in good agreement with previous research [37]. This appearance was similar to the $1-R-T$ value shown in Figure 7. This proved again that the enhancement in J_{sc} mainly resulted from the light-scattering effect inside of absorber layer by using the textured SnO₂ substrate. Furthermore, the η of cell devices can be improved from 4.04% to 4.39% as the t_{etch} was increased from 0 to 30 sec.

4. Conclusion

A wet chemical etching technique using a diluted HCl:Cr mixture was applied to the surface texturization of SnO₂ glass to enhance the light scattering. It was found that the etchant concentration, etching temperature, and etching time can influence the optoelectronic properties of SnO₂

films. From our measurement, the etching rate was increased with increasing the etchant concentration of Cr and etching temperature. The etchant with appropriate Cr concentration and etching parameters would lead to the good textured surface and optical characterization. The optimum etching parameters in this work were 0.15 wt.% Cr in 49% HCl, temperature of 90°C, and time of 30 sec. With increasing the etching time, the resistance of SnO₂ was increased because of the excessive damage to film surface. Moreover, as the optimum etching parameters were used for the surface texturization, the SnO₂ glass showed a better transmission haze of 8.38% as compared to that of original SnO₂ (7%). Meanwhile, by employing the optimum textured surface, the J_{sc} of 15.58 mA/cm², the V_{oc} of 0.52 V, the FF of 54.24%, and the η of 4.39% can be obtained in the thin-film solar cell with a 500 nm thick absorber. It presented about 8.7% increment in cell efficiency as compared with that using the original SnO₂ glass ($\eta = 4.04\%$). According to the EQE result, this improvement was mainly due to the light absorption in red and infrared regions. It was confirmed that the roughness of APCVD-deposited-SnO₂ surface can be moderately increased using wet chemical etching in a HCl:Cr solution. Additionally, with the employment of optimum textured parameters to SnO₂ surface, there is a positive influence on the light scattering. This can lead to the enhancements in current density and conversion efficiency of thin-film solar cell.

Conflict of Interests

The authors declare that there is no conflict of interests regarding the publication of this paper.

Acknowledgment

This research was supported by the National Science Council of Taiwan, under Contract no. NSC 99-2221-E-005-101-MY3.

References

- [1] C. M. Lee, S. P. Chang, S. J. Chang, and C. I. Wu, "High-efficiency si solar cell fabricated by ion implantation and inline backside rounding process," *International Journal of Photoenergy*, vol. 2012, Article ID 670981, 7 pages, 2012.
- [2] C. M. Lee, S. P. Chang, S. J. Chang, and C. I. Wu, "p-type quasi-mono silicon solar cell fabricated by ion implantation," *International Journal of Photoenergy*, vol. 2013, Article ID 171390, 8 pages, 2013.
- [3] B. Rech, T. Repmann, M. N. van den Donker et al., "Challenges in microcrystalline silicon based solar cell technology," *Thin Solid Films*, vol. 511-512, pp. 548–555, 2006.
- [4] J. Müller, B. Rech, J. Springer, and M. Vanecek, "TCO and light trapping in silicon thin film solar cells," *Solar Energy*, vol. 77, no. 6, pp. 917–930, 2004.
- [5] K. Yamamoto, A. Nakajima, M. Yoshimi et al., "A high efficiency thin film silicon solar cell and module," *Solar Energy*, vol. 77, no. 6, pp. 939–949, 2004.

- [6] T. Matsui, M. Tsukiji, H. Saika, T. Toyama, and H. Okamoto, "Influence of substrate texture on microstructure and photovoltaic performances of thin film polycrystalline silicon solar cells," *Journal of Non-Crystalline Solids*, vol. 299–302, no. 2, pp. 1152–1156, 2002.
- [7] T. Söderström, F.-J. Haug, V. Terrazoni-Daudrix, and C. Ballif, "Optimization of amorphous silicon thin film solar cells for flexible photovoltaics," *Journal of Applied Physics*, vol. 103, no. 11, Article ID 114509, 2008.
- [8] M. Berginski, J. Hüpkes, M. Schulte et al., "The effect of front ZnO:Al surface texture and optical transparency on efficient light trapping in silicon thin-film solar cells," *Journal of Applied Physics*, vol. 101, no. 7, Article ID 074903, 2007.
- [9] J. Müller, G. Schöpe, O. Kluth et al., "Upscaling of texture-etched zinc oxide substrates for silicon thin film solar cells," *Thin Solid Films*, vol. 392, no. 2, pp. 327–333, 2001.
- [10] Y. C. Lin, Y. C. Jian, and J. H. Jiang, "A study on the wet etching behavior of AZO (ZnO:Al) transparent conducting film," *Applied Surface Science*, vol. 254, no. 9, pp. 2671–2677, 2008.
- [11] O. Kluth, B. Rech, L. Houben et al., "Texture etched ZnO:Al coated glass substrates for silicon based thin film solar cells," *Thin Solid Films*, vol. 351, no. 1-2, pp. 247–253, 1999.
- [12] Y. Wang, X. Zhang, L. Bai, Q. Huang, C. Wei, and Y. Zhao, "Effective light trapping in thin film silicon solar cells from textured Al doped ZnO substrates with broad surface feature distributions," *Applied Physics Letters*, vol. 100, no. 26, Article ID 263508, 2012.
- [13] J. Springer, B. Rech, W. Reetz, J. Müller, and M. Vanecek, "Light trapping and optical losses in microcrystalline silicon pin solar cells deposited on surface-textured glass/ZnO substrates," *Solar Energy Materials and Solar Cells*, vol. 85, no. 1, pp. 1–11, 2005.
- [14] R. G. Gordon, J. Proscia, F. B. Ellis Jr., and A. E. Delahoy, "Textured tin oxide films produced by atmospheric pressure chemical vapor deposition from tetramethyltin and their usefulness in producing light trapping in thin film amorphous silicon solar cells," *Solar Energy Materials*, vol. 18, no. 5, pp. 263–281, 1989.
- [15] P. W. Simon, "Etchant and method of etching tin oxide film," Burroughs Corporation, U.S. Patent 4,009,061, 1977.
- [16] A. H. Mahan, J. Carapella, B. P. Nelson, R. S. Crandall, and I. Balberg, "Deposition of device quality, low H content amorphous silicon," *Journal of Applied Physics*, vol. 69, no. 9, pp. 6728–6730, 1991.
- [17] R. O. Dusane, S. R. Dusane, V. G. Bhide, and S. T. Kshirsagar, "Hydrogenated microcrystalline silicon films produced at low temperature by the hot wire deposition method," *Applied Physics Letters*, vol. 63, no. 16, pp. 2201–2203, 1993.
- [18] J. P. Conde, P. Alpuim, M. Boucinha, J. Gaspar, and V. Chu, "Amorphous and microcrystalline silicon deposited by hot-wire chemical vapor deposition at low substrate temperatures: application to devices and thin-film microelectromechanical systems," *Thin Solid Films*, vol. 395, no. 1-2, pp. 105–111, 2001.
- [19] T. Wu, H. Shen, B. Cheng, Y. Pan, C. Gao, and J. Shen, "Effect of filament temperature on properties of hot wire CVD deposited nc-3C-SiC films from SiH₄-C₂H₂-H₂ mixture," *Materials Research Innovations*, vol. 16, no. 3, pp. 165–169, 2012.
- [20] S. K. Soni, A. Phatak, and R. O. Dusane, "High deposition rate device quality a-Si:H films at low substrate temperature by HWCVD technique," *Solar Energy Materials and Solar Cells*, vol. 94, no. 9, pp. 1512–1515, 2010.
- [21] B. Schroeder, "Status report: solar cell related research and development using amorphous and microcrystalline silicon deposited by HW(Cat)CVD," *Thin Solid Films*, vol. 430, no. 1-2, pp. 1–6, 2003.
- [22] T. Chen, Y. Huang, D. Yang, R. Carius, and F. Finger, "Microcrystalline silicon thin film solar cells with microcrystalline silicon carbide window layers and silicon absorber layers both prepared by Hot-Wire CVD," *Physica Status Solidi: Rapid Research Letters*, vol. 4, no. 3-4, pp. 61–63, 2010.
- [23] M. Fonrodona, D. Soler, J. Escarré et al., "Low temperature amorphous and nanocrystalline silicon thin film transistors deposited by Hot-Wire CVD on glass substrate," *Thin Solid Films*, vol. 501, no. 1-2, pp. 303–306, 2006.
- [24] B. Stannowski, J. K. Rath, and R. E. I. Schropp, "Thin-film transistors deposited by hot-wire chemical vapor deposition," *Thin Solid Films*, vol. 430, no. 1-2, pp. 220–225, 2003.
- [25] B. R. Wu, S. Y. Lo, D. S. Wu et al., "Direct growth of large grain polycrystalline silicon films on aluminum-induced crystallization seed layer using hot-wire chemical vapor deposition," *Thin Solid Films*, vol. 520, no. 18, pp. 5860–5866, 2012.
- [26] S.-Y. Lien, D.-S. Wu, B.-R. Wu, R.-H. Horng, M.-C. Tseng, and H.-H. Yu, "Hot-wire CVD deposited n-type μ c-Si films for μ c-Si/c-Si heterojunction solar cell applications," *Thin Solid Films*, vol. 516, no. 5, pp. 765–769, 2008.
- [27] H.-Y. Mao, S.-Y. Lo, D.-S. Wu et al., "Hot-wire chemical vapor deposition and characterization of p-type nanocrystalline Si films for thin film photovoltaic applications," *Thin Solid Films*, vol. 520, no. 16, pp. 5200–5205, 2012.
- [28] H.-Y. Mao, D.-S. Wu, B.-R. Wu, S.-Y. Lo, H.-Y. Hsieh, and R.-H. Horng, "Hot-wire chemical vapor deposition and characterization of p-type nanocrystalline SiC films and their use in Si heterojunction solar cells," *Thin Solid Films*, vol. 520, no. 6, pp. 2110–2114, 2012.
- [29] S.-Y. Lien, B.-R. Wu, J.-C. Liu, and D.-S. Wu, "Fabrication and characteristics of n-Si/c-Si/p-Si heterojunction solar cells using hot-wire CVD," *Thin Solid Films*, vol. 516, no. 5, pp. 747–750, 2008.
- [30] A. Masuda and H. Matsumura, "Guiding principles for device-grade hydrogenated amorphous silicon films and design of catalytic chemical vapor deposition apparatus," *Thin Solid Films*, vol. 395, no. 1-2, pp. 112–115, 2001.
- [31] R. R. Arya, A. Catalano, and R. S. Oswald, "Amorphous silicon p-i-n solar cells with graded interface," *Applied Physics Letters*, vol. 49, no. 17, pp. 1089–1091, 1986.
- [32] A. Tabata, T. Nakajima, T. Mizutani, and Y. Suzuoki, "Preparation of wide-gap hydrogenated amorphous silicon carbide thin films by hot-wire chemical vapor deposition at a low tungsten temperature," *Japanese Journal of Applied Physics, Part 2: Letters*, vol. 42, no. 1, pp. L10–L12, 2003.
- [33] S. Miyajima, A. Yamada, and M. Konagai, "Characterization of undoped, N- and P-type hydrogenated nanocrystalline silicon carbide films deposited by hot-wire chemical vapor deposition at low temperatures," *Japanese Journal of Applied Physics, Part 1: Regular Papers and Short Notes and Review Papers*, vol. 46, no. 4, pp. 1415–1426, 2007.
- [34] J. I. Owen, J. Hüpkes, H. Zhu, E. Bunte, and S. E. Pust, "Novel etch process to tune crater size on magnetron sputtered ZnO:Al," *Physica Status Solidi (A) Applications and Materials Science*, vol. 208, no. 1, pp. 109–113, 2011.
- [35] H. Sai, H. Fujiwara, M. Kondo, and Y. Kanamori, "Enhancement of light trapping in thin-film hydrogenated microcrystalline Si solar cells using back reflectors with self-ordered dimple pattern," *Applied Physics Letters*, vol. 93, no. 14, Article ID 143501, 2008.

- [36] A. V. Shah, H. Schade, M. Vanecek et al., "Thin-film silicon solar cell technology," *Progress in Photovoltaics: Research and Applications*, vol. 12, no. 2-3, pp. 113–142, 2004.
- [37] M. L. Addonizio and A. Antonaia, "Surface morphology and light scattering properties of plasma etched ZnO:B films grown by LP-MOCVD for silicon thin film solar cells," *Thin Solid Films*, vol. 518, no. 4, pp. 1026–1031, 2009.

Research Article

Resistive Switching Characteristics of a SiO_x Layer with CF₄ Plasma Treatment

Chih-Yi Liu,¹ Yueh-Ying Tsai,¹ Wen-Tsung Fang,² and Hung-Yu Wang¹

¹ Department of Electronic Engineering, National Kaohsiung University of Applied Sciences, Kaohsiung 807, Taiwan

² Department of Physics, National Kaohsiung Normal University, Kaohsiung 824, Taiwan

Correspondence should be addressed to Chih-Yi Liu; cyluu@cc.kuas.edu.tw

Received 9 December 2013; Revised 8 February 2014; Accepted 8 February 2014; Published 11 March 2014

Academic Editor: Sheng-Po Chang

Copyright © 2014 Chih-Yi Liu et al. This is an open access article distributed under the Creative Commons Attribution License, which permits unrestricted use, distribution, and reproduction in any medium, provided the original work is properly cited.

A 20 nm SiO_x layer is deposited using radio-frequency sputtering to form the resistive switching layer of a Cu/SiO_x/Pt memory device. The SiO_x-based device demonstrates the resistive switching characteristics with an electrochemical reaction. CF₄ plasma treatment was used to modify the SiO_x layer and incorporate fluorine atoms into the SiO_x layer. The bombardment damage and fluorine incorporation caused the SiO_x film to form a stack-like structure. This reduced the operating voltage and improved switching dispersion. The fluorine repaired the Cu/SiO_x interface, thus increasing the barrier height of the Cu/SiO_x interface and the resistance of the high resistance state. A statistical analysis of the conducting filament formation was performed in order to evaluate the number of formation/rupture sites. The resistive switching of the CF₄-treated sample had higher possibility to use the same filament sites; thus, the CF₄-treated sample had stable resistive switching behavior.

1. Introduction

Recently, nonvolatile memory (NVM) has become an important device for portable products. Several novel technologies have been proposed to develop an advanced device as the next generation of NVM. Resistive random access memory (RRAM) has attracted significant interest due to its simple structure, high switching speed, and low operating voltage [1]. RRAM devices can be reversibly switched between a high resistance state (HRS) and a low resistance state (LRS) by DC voltages or voltage pulses. The resistance change can be used to store information for NVM applications. The resistive switching behavior is primarily influenced by the material groups [2, 3], electrodes [4], and interface status [5, 6]. In general, the switching mechanisms of these resistive switching behaviors can be divided into three groups: thermochemical reactions [7], electrochemical reactions [8–10], and the valence change effect [11]. However, a detailed switching mechanism is still lacking. Several studies [12–14] proposed the surface effect on the resistive switching behaviors, which indicated that oxygen or humidity may influence the redox reaction in the interface or resistive layer. Although a RRAM

device has many promising advantages, the resistive switching behavior is unstable and may cause operation failure. Therefore, several methods such as nanoparticle [15], stacked layers [16], and process optimization [17] have been proposed to improve the switching dispersion. Plasma treatments have also been proposed to improve switching dispersion [18, 19]. Wang et al. proposed the CF₄ plasma treatment to improve the resistive switching properties with the valence change effect [19]. The CF₄ plasma treatment changed the Schottky barrier height to reduce the operating voltages. However, the effect of plasma treatment on an electrochemical-based RRAM has not been studied.

This study adopted Cu and SiO_x materials to fabricate a RRAM device in order to integrate them with the complementary metal-oxide-semiconductor (CMOS) process. In this study, a Cu/SiO_x/Pt structure was fabricated to investigate the resistive switching behavior of an electrochemical RRAM device. CF₄ is a common molecule used in the CMOS etching process. CF₄ plasma treatment has been used previously to improve the Si/SiO₂ interface of a MOS structure [20]. In this study we adopted the CF₄ plasma treatment to modify the SiO_x layer and investigated its effect

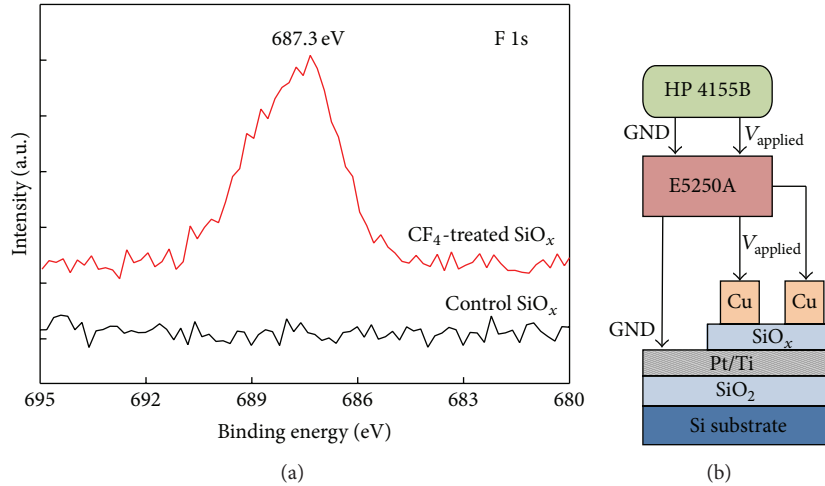


FIGURE 1: (a) The XPS results of the control and CF_4 -treated films and (b) the measurement configuration of the conducting filament formation.

on the resistive switching behavior of a $\text{Cu}/\text{SiO}_x/\text{Pt}$ device. The CF_4 plasma treatment reduces the operating voltage and improves the switching dispersion. The bombardment damage and fluorine incorporation should be responsible for the switching dispersion improvement.

2. Experimental Procedure

A 20 nm SiO_x film was deposited on a Pt-coated substrate (Pt/Ti/ SiO_2/Si) in a pure Ar ambient using a radio-frequency sputter at room temperature. The related information of the SiO_x film can be found in our previous study [21]. A 200 nm Cu top electrode was deposited using a thermal evaporation technique to form a $\text{Cu}/\text{SiO}_x/\text{Pt}$ structure (control sample). The top electrode area, as defined by the metal mask, was $5 \times 10^{-5} \text{ cm}^2$. A 30 nm SiO_x film was also deposited on a Pt-coated substrate. CF_4 plasma treatment of 25 W was used to etch the SiO_x film back to a 20 nm SiO_x film and incorporate fluorine atoms into the SiO_x film. Next, a 200 nm Cu film was deposited to form the Cu/CF_4 -treated SiO_x/Pt structure (CF_4 -treated sample). As shown in Figure 1(a), the result of X-ray photoelectron spectroscopy (XPS, JAMP-9500F, JEOL) spectra of the CF_4 -treated SiO_x film indicates that fluorine atoms were incorporated into the SiO_x layer. The electrical measurements were performed using an HP 4155B semiconductor parameter analyzer and an Agilent E5250A low-leakage switch mainframe at room temperature. The bias voltage was applied on the Cu top electrode of a single device and the bottom electrode was grounded in order to measure the current-voltage characteristics. To prevent the influence of surface effect, all electrical measurements were performed in the air ambient with 60% relative humidity. In Figure 1(b) the measurement configuration of the conducting filament formation is shown. Two devices were connected in parallel forming a single pair and were stimulated by the same electrical signal at the same time. A small read voltage (0.05 V) was used to measure each device's resistance. The formation statistics and reuse probability were calculated

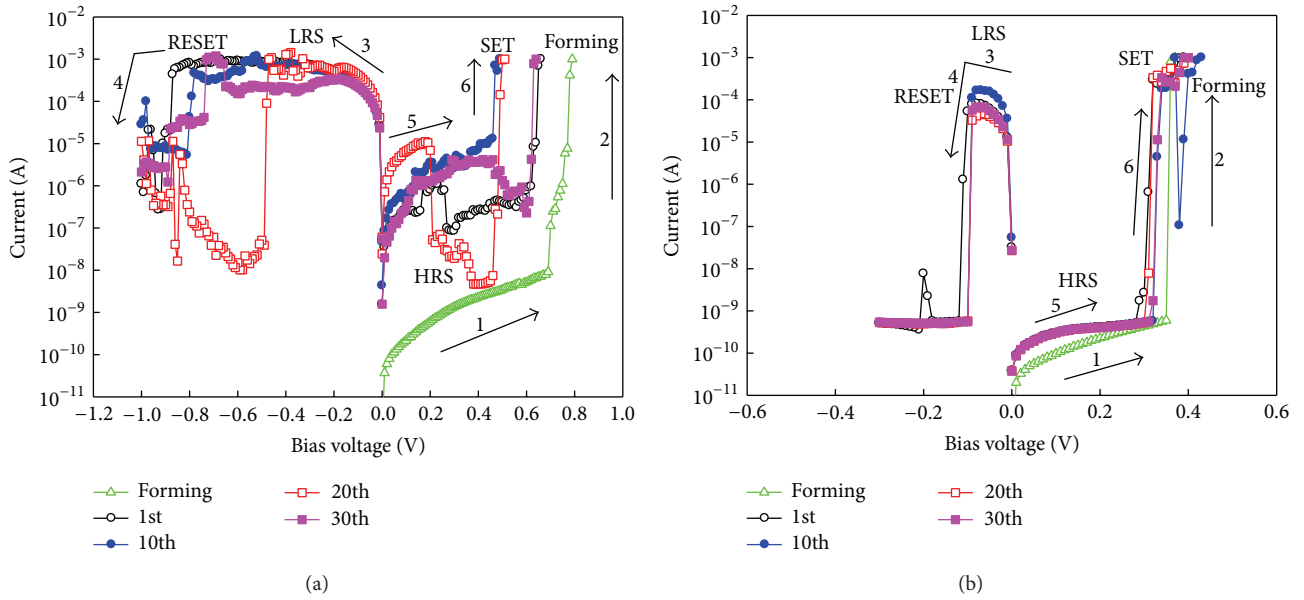
with 10 pairs, with each pair having 100 successive switching cycles.

3. Results and Discussion

In Figure 2(a) 30 successive resistive switching cycles of the control sample are shown. The device current abruptly increases by a forming process in the positive polarity stage. The device current is abruptly decreased by a RESET voltage when the polarity is negative and increases again by a SET voltage in the positive polarity. The device current can reversibly switch between a HRS and a LRS by DC voltages in various polarities. A compliance current of 1 mA was used to prevent permanent damage during the forming and SET processes. The current-voltage characteristics were unstable during the voltage sweeping. The resistance states and the operating voltages showed a large dispersion. Figure 2(b) shows 30 successive resistive switching cycles of the CF_4 -treated sample. Its resistive switching was more stable than that of the control sample. Compared with the control sample, the SET and RESET voltages of the CF_4 -treated sample were almost identical. According to the switching mechanism of the conducting filament model with the electrochemical reaction, a positive voltage is applied to the Cu electrode during the SET process. The Cu metal is dissolved into Cu ions, and then Cu ions drift across the SiO_x film to the Pt electrode. Then, the Cu ions reduce and electrodeposit on the Pt electrode. Next, a Cu conducting filament grows to connect the Cu and Pt electrodes, and thus the resistive state is switched to the LRS. A negative voltage is applied to the Cu electrode during the RESET process, and the part of the conducting filament near the Cu/SiO_x interface is dissolved to rupture the conducting filament and thus the resistive state is switched to the HRS. Fitting curves of ohmic conduction for the LRS current-voltage characteristics of the control sample and the CF_4 -treated sample indicate that the LRS exhibited linearly ohmic behaviors with slopes of 0.982 and 0.981, respectively [22]. The LRS conduction mechanisms of

TABLE 1: The statistical results of the conducting filament formation for the control and CF₄-treated samples.

	After forming process		SET process		
	Type	Percentage	Multiple filament	Reuse difference	Reuse sum
Control sample	Single	50%	1.5%	94.8%	97.7%
	Multiple	50%	7.9%	49.3%	88.9%
	Total	100%	4.7%	72.0%	93.3%
CF ₄ -treated sample	Single	100%	0.4%	95.4%	96.8%

FIGURE 2: (a) Resistive switching behaviors of the control sample and (b) resistive switching behavior of the CF₄-treated sample. Numbers and arrows denote the sequence.

the two samples were consistent with the conducting filament model.

In Figure 3(a), the statistical analysis of the operating voltages of the two samples is shown. The magnitudes of the operating voltages of the CF₄-treated sample were smaller than those of the control sample. In addition, the CF₄-treated sample had smaller voltage dispersion than the control sample. This improvement in voltage dispersion can simplify circuit design and prevent operation failure. Figure 3(b) shows the statistical results of the device resistance of the control and CF₄-treated samples. The LRS resistance of the two samples was almost identical due to the same compliance current [23]. The XPS result from Figure 1(a) indicates that fluorine atoms were incorporated into the SiO_x film. Fluorine can repair the dangling bonds within the SiO_x film; thus, the Cu/SiO_x interface status improves. To prevent the disturbance of Cu dissolution into the SiO_x layer, the current-voltage characteristics of the HRS were measured at negative polarity. The formula of the Schottky emission [21] can be expressed as

$$J = A^* * T^2 * \exp\left(\frac{q\sqrt{qE}/4\pi\epsilon_i}{kT} - \frac{q\Phi_B}{kT}\right), \quad (1)$$

where J is the current density, A^* is the effective Richardson constant, T is the temperature, q is the elementary charge, k

is the Boltzmann constant, E is the electric field, Φ_B is the barrier height, and ϵ_i is the insulator dynamic permittivity. According to the fitting results, the HRS conduction mechanism of the two samples was dominated by the Schottky emission. The Schottky barriers of the control and CF₄-treated samples were 0.77 eV and 0.81 eV, respectively. Hence, the HRS resistance of the CF₄-treated sample was larger than that of the control sample. In addition, the HRS of the CF₄-treated sample had smaller dispersion than that of the control sample. Therefore, the CF₄-treated sample had a much higher switching margin than the control sample. Figure 4 shows the endurance characteristics of the two samples. The control sample showed large switching dispersion. Many soft errors could be found during successive switching cycles. The endurance cycle of the control sample was less than 1000, while the CF₄-treated sample showed stable switching cycles and an endurance cycle of over 2500.

To further understand the formation of conducting filaments within the SiO_x film, two devices had the same sweep voltage applied at the same time (Figure 1(b)), while their resistance was recorded. Table 1 shows the statistical results of the conducting filament formation. In some situations, the conducting filament can be found in only one device, which is known as single-filament switching. In another case, the conducting filament can be found in

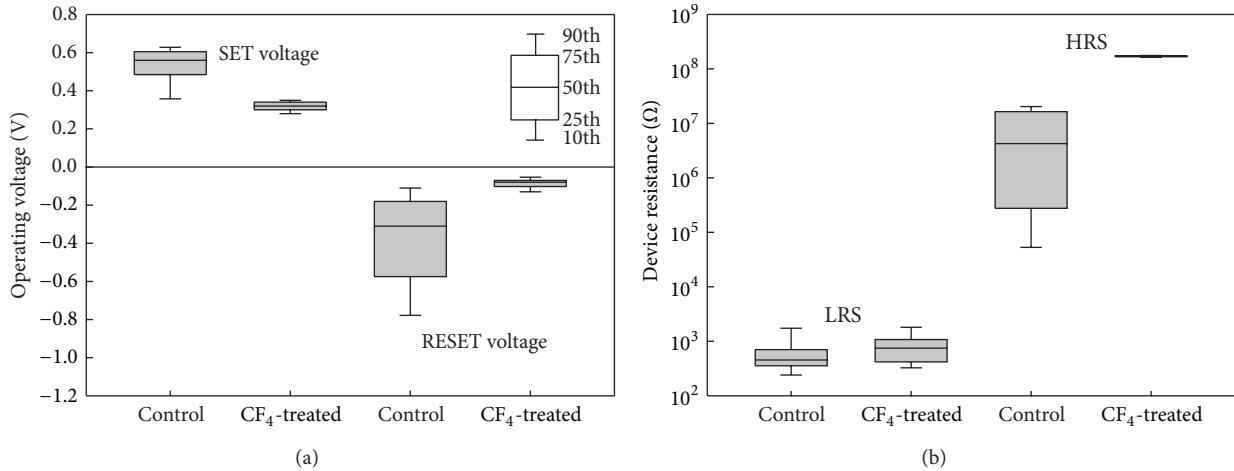


FIGURE 3: (a) The operating voltage of the control and CF₄-treated samples and (b) the device resistances of the control and CF₄-treated samples.

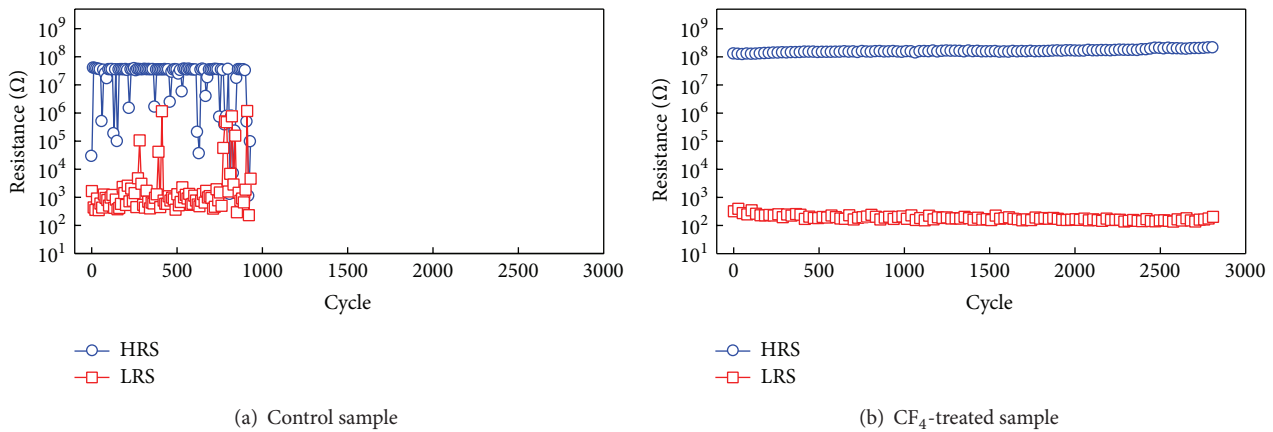


FIGURE 4: The endurance characteristics of the control and CF₄-treated samples.

both devices at the same time. Based on logical reasoning, there should be more than two conducting filaments in this pair, which was called multiple-filament switching. After the forming process, the control sample had 50% single-filament and 50% multiple-filament cases. In comparison, the CF₄-treated sample had 100% single-filament cases. Multiple-filament switching means that the device may switch via different conducting filaments. The control sample had 4.7% multiple-filament switching during the successive switching cycles, which indicated that multiple conducting filaments existed, which could cause complex formation/rupture of conducting filaments. In comparison, the CF₄-treated sample only had 0.4% multiple-filament switching, which showed a more stable switching behavior. The definition of reuse is the conducting filament formed in the same device as the previous cycle. The reuse difference is the difference of the reuse in the two devices. The reuse sum is the total reuse in the pair. The CF₄-treated sample had a larger reuse difference and reuse sum than the control sample, which indicated that the conducting filaments within the CF₄-treated sample had higher possibility to be formed at the same sites. Therefore,

the CF₄-treated sample displayed a more stable resistive switching behavior.

The CF₄-treated SiO_x film was bombarded with ions, which may cause more traps in the near-surface of the SiO_x film than in the lower region [24]. The traps within the SiO_x layer would increase the Cu diffusion coefficient. In Figure 1(a) it can be seen that the fluorine atoms were incorporated into the SiO_x film. Fluorine incorporation could decrease the dielectric constant of the SiO₂ layer [20]. Therefore, the dielectric constant of the near surface was smaller than that of the lower region. According to Gauss' law, the electrical field in the near surface was larger than that in the lower region. Therefore, the formation/rupture of the Cu filament would be confined within the near surface, which decreased the operating voltage and improved the switching dispersion. In addition, the HRS and LRS retention times of the CF₄-treated sample were more than 10⁴ s at room temperature. The CF₄-treated sample had a small operating voltage, stable resistive switching, high resistance ratio, high endurance, and long retention time. These factors mean that the device is an ideal candidate for the next-generation of NVM.

4. Conclusions

The influence of CF_4 plasma treatment on the resistive switching behavior of a $\text{Cu}/\text{SiO}_x/\text{Pt}$ structure was investigated. The ion bombardment and fluorine incorporation in the near-surface of the SiO_x film caused the SiO_x film to become a stack-like structure, which confines the formation/rupture in the near surface. Therefore, the CF_4 plasma treatment decreased the operating voltage and improved the switching dispersion. A statistical analysis of conducting filament formation was calculated to explain the resistive switching behavior using single-filament or multiple-filament switching. The CF_4 -treated sample had a larger probability of single-filament switching than the control sample. Therefore, resistive switching of the CF_4 -treated sample almost always occurred through the same filament, giving rise to the smaller switching dispersion.

Conflict of Interests

The authors declare that they have no conflict of interests regarding the publication of this paper.

Acknowledgments

The authors thank the National Science Council of R.O.C. for their financial supports under Project no. NSC 101-2221-E-151-044 and the facility support from National Nano Device Laboratories.

References

- [1] A. Beck, J. G. Bednorz, C. Gerber, C. Rossel, and D. Widmer, "Reproducible switching effect in thin oxide films for memory applications," *Applied Physics Letters*, vol. 77, no. 1, pp. 139–141, 2000.
- [2] A. Sawa, "Resistive switching in transition metal oxides," *Materials Today*, vol. 11, no. 6, pp. 28–36, 2008.
- [3] C.-H. Lai and T.-Y. Tseng, "Preparation and properties of perovskite thin films for resistive nonvolatile memory applications," *Ferroelectrics*, vol. 357, no. 1, pp. 17–27, 2007.
- [4] L. Goux, K. Opsomer, R. Degraeve et al., "Influence of the Cu-Te composition and microstructure on the resistive switching of Cu-Te/ $\text{Al}_2\text{O}_3/\text{Si}$ cells," *Applied Physics Letters*, vol. 99, no. 5, Article ID 053502, 2011.
- [5] P. Zhou, M. Yin, H. J. Wan, H. B. Lu, T. A. Tang, and Y. Y. Lin, "Role of TaON interface for Cu_xO resistive switching memory based on a combined model," *Applied Physics Letters*, vol. 94, no. 5, Article ID 053510, 2009.
- [6] C. H. Lai, C. H. Chen, and T. Y. Tseng, "Resistive switching behavior of sol-gel deposited TiO_2 thin films under different heating ambience," *Surface and Coatings Technology*, vol. 231, pp. 399–402, 2013.
- [7] C. Cagli, F. Nardi, and D. Ielmini, "Modeling of set/reset operations in NiO-based resistive-switching memory devices," *IEEE Transactions on Electron Devices*, vol. 56, no. 8, pp. 1712–1720, 2009.
- [8] C.-Y. Liu, Y.-H. Huang, J.-Y. Ho, and C.-C. Huang, "Retention mechanism of Cu-doped SiO_2 -based resistive memory," *Journal of Physics D*, vol. 44, no. 20, Article ID 205103, 2011.
- [9] I. Valov, R. Waser, J. R. Jameson, and M. N. Kozicki, "Electrochemical metallization memories: fundamentals, applications, prospects," *Nanotechnology*, vol. 22, no. 25, Article ID 254003, 2011.
- [10] S. Yu and H.-S. P. Wong, "Modeling the switching dynamics of Programmable-Metallization-Cell (PMC) memory and its application as synapse device for a neuromorphic computation system," in *Proceedings of the IEEE International Electron Devices Meeting (IEDM '10)*, pp. 520–523, December 2010.
- [11] R. Waser, R. Dittmann, C. Staikov, and K. Szot, "Redox-based resistive switching memories nanoionic mechanisms, prospects, and challenges," *Advanced Materials*, vol. 21, no. 25–26, pp. 2632–2663, 2009.
- [12] P. K. Yang, W. Y. Chang, P. Y. Teng, and S. F. Jeng, "Fully transparent resistive memory employing graphene electrodes for eliminating undesired surface effects," *Proceedings of the IEEE*, vol. 101, no. 7, pp. 1732–1739, 2013.
- [13] J. J. Ke, Z. J. Liu, C. F. Kang, and S. J. Lin, "Surface effect on resistive switching behaviors of ZnO," *Apply Physics Letters*, vol. 99, Article ID 192106, 3 pages, 2011.
- [14] T. H. Huang, P. K. Yang, W. Y. Chang et al., "Eliminating surface effects via employing nitrogen doping to significantly improve the stability and reliability of ZnO resistive memory," *Journal of Materials Chemistry C*, vol. 1, no. 45, pp. 7593–7597, 2013.
- [15] Y.-T. Tsai, T.-C. Chang, C.-C. Lin et al., "Influence of nanocrystals on resistive switching characteristic in binary metal oxides memory devices," *Electrochemical and Solid-State Letters*, vol. 14, no. 3, pp. H135–H138, 2011.
- [16] Q.-Q. Sun, J.-J. Gu, L. Chen et al., "Controllable filament with electric field engineering for resistive switching uniformity," *IEEE Electron Device Letters*, vol. 32, no. 9, pp. 1167–1169, 2011.
- [17] R. Jung, M.-J. Lee, S. Seo et al., "Decrease in switching voltage fluctuation of PtNi O_x Pt structure by process control," *Applied Physics Letters*, vol. 91, no. 2, Article ID 022112, 2007.
- [18] C. Vallée, P. Gonon, C. Mannequin et al., "Plasma treatment of HfO_2 -based metalinsulator-metal resistive memories," *Journal of Vacuum Science and Technology A*, vol. 29, no. 4, Article ID 041512, 2011.
- [19] J. C. Wang, Y. R. Ye, C. S. Lai et al., "Characterization of gadolinium oxide thin films with CF_4 plasma treatment for resistive switching memory applications," *Applied Surface Science*, vol. 276, pp. 497–501, 2013.
- [20] Y.-H. Kim, M. S. Hwang, H. J. Kim, J. Y. Kim, and Y. Lee, "Infrared spectroscopy study of low-dielectric-constant fluorine-incorporated and carbon-incorporated silicon oxide films," *Journal of Applied Physics*, vol. 90, no. 7, pp. 3367–3370, 2001.
- [21] C. Y. Liu, Y. R. Shih, and S. J. Huang, "Unipolar resistive switching in a transparent ITO/ SiO_x /ITO sandwich fabricated at room temperature," *Solid State Communications*, vol. 159, pp. 13–17, 2013.
- [22] S. M. Sze, *Physics of Semiconductor Devices*, Wiley, New York, NY, USA, 2nd edition, 1981.
- [23] S. Menzel, U. Böttger, and R. Waser, "Simulation of multilevel switching in electrochemical metallization memory cells," *Journal of Applied Physics*, vol. 111, no. 1, Article ID 014501, 2012.
- [24] N. Yuan and J. Li, "Improve the charge stability of SiO_2 films by plasma treatment and ion implantation," in *5th International Conference on Thin Film Physics and Applications*, vol. 5774 of *Proceedings of SPIE*, p. 78, December 2004.

Research Article

Enhanced Performance of $\text{Mg}_{0.1}\text{Zn}_{0.9}\text{O}$ UV Photodetectors Using Photoelectrochemical Treatment and Silica Nanospheres

Hsin-Ying Lee,¹ Yu-Chang Lin,¹ Meng-Ju Lee,² Wu-Yih Uen,² and Kondepudy Sreenivas³

¹ Department of Photonics, Advanced Optoelectronic Technology Center, National Cheng Kung University, Tainan 701, Taiwan

² Department of Electronic Engineering, Chung Yuan Christian University, Chung Li 320, Taiwan

³ Department of Physics and Astrophysics, University of Delhi, Delhi110007, India

Correspondence should be addressed to Hsin-Ying Lee; hylee@ee.ncku.edu.tw

Received 11 December 2013; Revised 24 January 2014; Accepted 24 January 2014; Published 5 March 2014

Academic Editor: Sheng-Po Chang

Copyright © 2014 Hsin-Ying Lee et al. This is an open access article distributed under the Creative Commons Attribution License, which permits unrestricted use, distribution, and reproduction in any medium, provided the original work is properly cited.

The $\text{Mg}_{0.1}\text{Zn}_{0.9}\text{O}$ films were grown using atomic layer deposition (ALD) system and applied to metal-semiconductor-metal ultraviolet photodetectors (MSM-UPDs) as an active layer. To suppress the dangling bonds on the $\text{Mg}_{0.1}\text{Zn}_{0.9}\text{O}$ surface, the photoelectrochemical (PEC) treatment was used to passivate the $\text{Mg}_{0.1}\text{Zn}_{0.9}\text{O}$ surface, which could reduce the dark current of the MSM-UPDs about one order. Beside, to increase more incident light into the $\text{Mg}_{0.1}\text{Zn}_{0.9}\text{O}$ active layer of the MSM-UPDs, the 500-nm-diameter silica nanospheres were spin-coated on the $\text{Mg}_{0.1}\text{Zn}_{0.9}\text{O}$ active layer to improve the antireflection capability at the wavelength of 340 nm. The reflectivity of the $\text{Mg}_{0.1}\text{Zn}_{0.9}\text{O}$ films with silica nanospheres antireflection layer decreased about 7.0% in comparison with the $\text{Mg}_{0.1}\text{Zn}_{0.9}\text{O}$ films without silica nanospheres. The photocurrent and UV-visible ratio of the passivated $\text{Mg}_{0.1}\text{Zn}_{0.9}\text{O}$ MSM-UPDs with antireflection layer were enhanced to 5.85 μA and 1.44×10^4 , respectively, at the bias voltage of 5 V. Moreover, the noise equivalent power and the specific detectivity of the passivated $\text{Mg}_{0.1}\text{Zn}_{0.9}\text{O}$ MSM-UPDs with antireflection layer were decreased to 2.60×10^{-13} W and increased to 1.21×10^{12} $\text{cmHz}^{1/2}\text{W}^{-1}$, respectively, at the bias voltage of 5 V. According to the above mentions, the PEC treatment and silica nanospheres antireflection layer could effectively enhance the performance of $\text{Mg}_{0.1}\text{Zn}_{0.9}\text{O}$ MSM-UPDs.

1. Introduction

Ultraviolet (UV) photodetectors have received more attention due to their wide applications, such as flame detection, chemical agent detection, space communications, and solar astronomy [1–3]. Different kinds of UV photodetectors have been developed to fit the requirements for various applications. To fabricate UV and deep UV photodetectors, the ternary magnesium zinc oxide ($\text{Mg}_x\text{Zn}_{1-x}\text{O}$) with the wide bandgap is a promising candidate. Owing to the fact that the ionic radius of Mg^{2+} (0.57 Å) is very close to that of Zn^{2+} (0.6 Å), the $\text{Mg}_x\text{Zn}_{1-x}\text{O}$ alloy with Mg content $x = 0.36$ remains a single phase wurtzite structure [4]. Recently, several researches reported that $\text{Mg}_x\text{Zn}_{1-x}\text{O}$ films were prepared by various techniques, such as molecular beam epitaxy (MBE) [5, 6], metal organic chemical vapor deposition (MOCVD) [7, 8], magnetron radio frequency (RF) sputtering [9, 10], vapor cooling condensation system

[11], and pulsed laser deposition (PLD) [12, 13]. In this work, the high quality $\text{Mg}_{0.1}\text{Zn}_{0.9}\text{O}$ films were deposited using an atomic layer deposition (ALD) and applied in the metal-semiconductor-metal ultraviolet photodetectors (MSM-UPDs). Since the surface states on the $\text{Mg}_x\text{Zn}_{1-x}\text{O}$ surface seriously affected the performance of the MSM-UPDs, how to improve the surface states was the primary issue. There were some methods, such as hydrogen peroxide treatment [14], $(\text{NH}_4)_2\text{S}_x$ treatment [15], and photoelectrochemical (PEC) treatment [16] that were used to passivate the $\text{Mg}_x\text{Zn}_{1-x}\text{O}$ surface. In this work, the PEC treatment was used to passivate the $\text{Mg}_{0.1}\text{Zn}_{0.9}\text{O}$ surface to decrease the dangling bond on the $\text{Mg}_{0.1}\text{Zn}_{0.9}\text{O}$ surface, which could reduce the surface states and improve the performance of the MSM-UPDs. Moreover, to further enhance the performance of the detectors, the antireflection technique was applied to increase the amount of light incident into the active layer of the MSM-UPDs. Many approaches were used to deposit

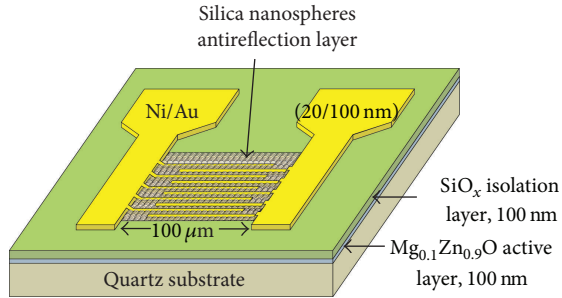


FIGURE 1: The schematic configuration of $\text{Mg}_{0.1}\text{Zn}_{0.9}\text{O}$ MSM-UPDs with silica nanospheres antireflection layer.

the antireflection layers, such as magnetron RF sputtering [17], electron-beam evaporator [18], lithography technologies [19], phase-separation [20], and self-assembled technology [21]. Among these, the self-assembled technology had some advantages: low cost, easier preparation, and low deposition temperature. In this work, the self-assembled technology was used to form a self-assembled silica nanosphere layer as an antireflection layer for the $\text{Mg}_{0.1}\text{Zn}_{0.9}\text{O}$ MSM-UPDs. The performance enhancement of the $\text{Mg}_{0.1}\text{Zn}_{0.9}\text{O}$ MSM-UPDs using PEC treatment and an antireflection nanosphere layer was investigated.

2. Experimental Procedures

Figure 1 shows the schematic configuration of the $\text{Mg}_{0.1}\text{Zn}_{0.9}\text{O}$ MSM-UPDs with silica nanospheres antireflection layer. The 100 nm-thick $\text{Mg}_{0.1}\text{Zn}_{0.9}\text{O}$ films were deposited on the quartz substrates using an ALD system. The precursors of diethylzinc (DEZn), bis (cyclopentadienyl) magnesium (Cp_2Mg), and water (H_2O) were used as zinc (Zn), magnesium (Mg), and oxygen (O) sources, respectively. The chamber pressure and the substrate temperature were fixed at 0.6 torr and 100°C , respectively. The pulse time of DEZn, Cp_2Mg , and H_2O was 0.5 s, 2 s, and 1 s, respectively. After each step of reactant, argon (Ar) gas was utilized as the carrier gas for 3 s. In the ALD system, the Mg content of the $\text{Mg}_x\text{Zn}_{1-x}\text{O}$ film was varied by changing the cycle ratio of ZnO to MgO. In this work, the $\text{Mg}_{0.1}\text{Zn}_{0.9}\text{O}$ film was repeatedly deposited by stacking nine ZnO cycles and one MgO cycle. In the deposited procedure, the ZnO cycle was the end cycle. The composition of $\text{Mg}_x\text{Zn}_{1-x}\text{O}$ film was measured by the energy dispersive spectrometer (EDS), and the content (x) of Mg was estimated to be 0.1. The optical energy bandgap of the resultant $\text{Mg}_{0.1}\text{Zn}_{0.9}\text{O}$ film was estimated to be 3.65 eV using the transmission spectrum. To fabricate MSM-UPDs, the active region of $100 \times 100 \mu\text{m}^2$ was defined by conventional photolithography and lift-off technique, and then a 100 nm-thick SiO_x isolation layer was deposited by a magnetron RF sputtering. Prior to the interdigital metal deposition, the surface of active region was passivated using the PEC treatment to decrease surface states and dangling bonds. In the PEC treatment processes, the MSM-UPDs were dipped in the ammonia (NH_4OH) electrolytic solution with a pH value of 8.6 and illuminated

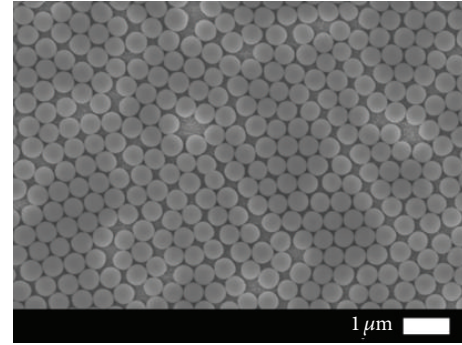


FIGURE 2: The surface morphology of the 500 nm-diameter silica nanospheres antireflection layer.

by He-Cd laser with the wavelength of 325 nm and power density of $10 \text{ mW}/\text{cm}^2$ for 90 s. The interdigital Schottky metals Ni/Au (20 nm/100 nm) were immediately deposited on the $\text{Mg}_{0.1}\text{Zn}_{0.9}\text{O}$ active layer with PEC treatment using an electron-beam evaporator. Both the width and spacing of the metal fingers were $2 \mu\text{m}$. Finally, the silica nanospheres with 500 nm diameter were coated on the surface of MSM-UPDs as the antireflection layer using a self-assembled technology. The coating procedure of silica nanospheres included that the rotational speed was 300 rpm for 60 s and then the rotational speed immediately increased to 3000 rpm for 30 s. The surface morphology of the 500 nm-diameter silica nanospheres coated layer on $\text{Mg}_{0.1}\text{Zn}_{0.9}\text{O}$ films deposited on the quartz substrates was observed by scanning electron microscopy (SEM) and is shown in Figure 2. It can be seen that the silica nanoparticles coated layer was a uniform single layer. The electrical characteristics of the $\text{Mg}_{0.1}\text{Zn}_{0.9}\text{O}$ MSM-UPDs were characterized by Agilent 4156 C semiconductor parameter analyzer. The photoresponsivity spectra of the $\text{Mg}_{0.1}\text{Zn}_{0.9}\text{O}$ MSM-UPDs were measured using a monochromator and an Xe lamp source.

3. Results and Discussion

To understand the function of the PEC treatment, the current-voltage (I - V) characteristic of the $\text{Mg}_{0.1}\text{Zn}_{0.9}\text{O}$ MSM-UPDs with and without PEC treatment was measured and is shown in Figure 3. At bias voltage of 5 V, the dark current of the resultant MSM-UPDs with and without PEC treatment was 0.15 nA and 1.66 nA, respectively. The dark current of the passivated $\text{Mg}_{0.1}\text{Zn}_{0.9}\text{O}$ MSM-UPDs was lower than that of the unpassivated $\text{Mg}_{0.1}\text{Zn}_{0.9}\text{O}$ MSM-UPDs for all applied voltages. In general, the dark current was probably influenced by the surface condition. Since the $\text{Mg}_{0.1}\text{Zn}_{0.9}\text{O}$ film deposited using ALD system, some dangling bonds remained on the $\text{Mg}_{0.1}\text{Zn}_{0.9}\text{O}$ surface. In the previous publish [22], the PEC treatment technique have used to treat the ZnO surface, which could form the $\text{Zn}(\text{OH})_2$ thin film on the ZnO surface. Therefore, the reduction of dark current was attributed to the fact that the PEC treatment could effectively diminish the number of dangling bonds on the $\text{Mg}_{0.1}\text{Zn}_{0.9}\text{O}$ surface. The photocurrent of the $\text{Mg}_{0.1}\text{Zn}_{0.9}\text{O}$ MSM-UPDs

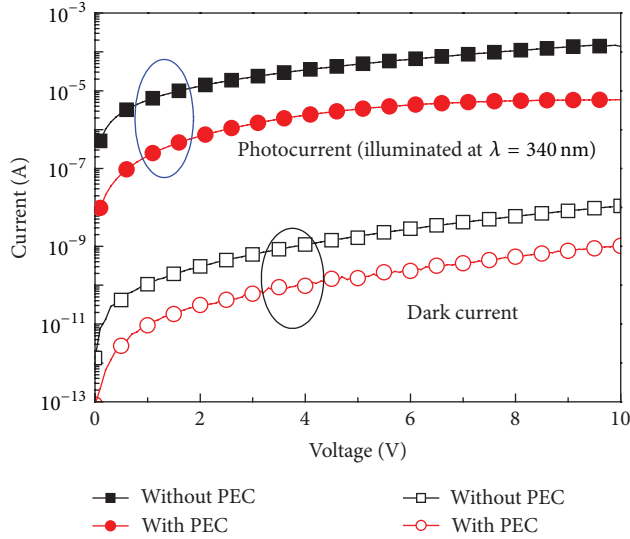


FIGURE 3: The current-voltage characteristics of the $\text{Mg}_{0.1}\text{Zn}_{0.9}\text{O}$ MSM-UPDs with and without PEC treatment.

with and without PEC treatment illuminated by a UV light with a wavelength of 340 nm was also measured and is shown in Figure 3. The photocurrent of the unpassivated $\text{Mg}_{0.1}\text{Zn}_{0.9}\text{O}$ MSM-UPDs was larger than the passivated $\text{Mg}_{0.1}\text{Zn}_{0.9}\text{O}$ MSM-UPDs for all applied voltages. The photoinduced holes were trapped and accumulated between the active layer and cathode of the photodetectors due to the presence of defects on the active layer surface [23, 24]. Therefore, the internal gain of the unpassivated $\text{Mg}_{0.1}\text{Zn}_{0.9}\text{O}$ MSM-UPDs was caused by photoinduced holes accumulation, which reduced the Schottky barrier height between metal and $\text{Mg}_{0.1}\text{Zn}_{0.9}\text{O}$ film. Consequently, the higher photocurrent was attributed to the internal gain caused in the unpassivated $\text{Mg}_{0.1}\text{Zn}_{0.9}\text{O}$ MSM-UPDs.

To enhance the amount of incident light upon the $\text{Mg}_{0.1}\text{Zn}_{0.9}\text{O}$ MSM-UPDs, the 500 nm-diameter silica nanospheres were spin-coated to form a single layer as the antireflection layer on the $\text{Mg}_{0.1}\text{Zn}_{0.9}\text{O}$ MSM-UPDs. The optimal effective refractive index of the antireflection layer (n_{AR}) was estimated by the formula $n_{\text{AR}} = \sqrt{n_{\text{air}} \times n_{\text{Mg}_{0.1}\text{Zn}_{0.9}\text{O}}}$, where n_{air} of 1.00 and $n_{\text{Mg}_{0.1}\text{Zn}_{0.9}\text{O}}$ of 2.30 were the refractive indices of air and $\text{Mg}_{0.1}\text{Zn}_{0.9}\text{O}$ at wavelength of 340 nm, respectively. The solution of the optimal effective refractive index of the antireflection layer was 1.51. In this work, the effective refractive index of the silica nanospheres was measured by an ellipsometer and the value was about 1.48 which was similar to the optimal effective refractive index of the antireflection layer. Figure 4 shows the reflectivity of the $\text{Mg}_{0.1}\text{Zn}_{0.9}\text{O}$ films with and without silica nanospheres antireflection layer. As shown in Figure 4, the reflectivity of the $\text{Mg}_{0.1}\text{Zn}_{0.9}\text{O}$ films without and with silica nanospheres was 9.9% and 2.9% at the wavelength of 340 nm, respectively. Therefore, it was confirmed that the silica nanosphere was suitable to be used to form antireflection layer in the

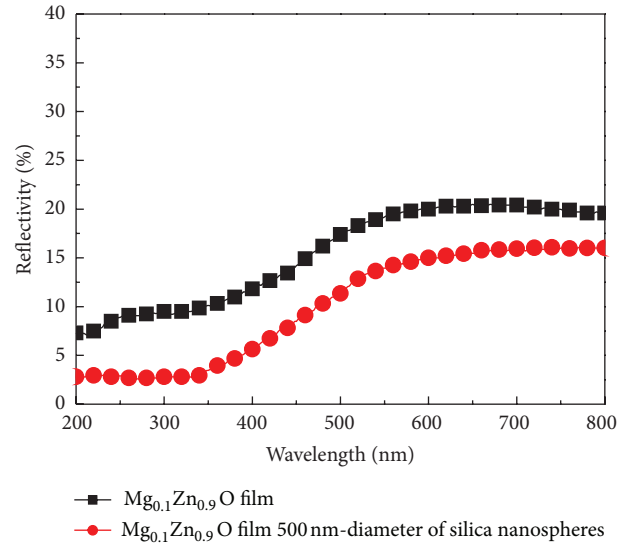


FIGURE 4: Reflectivity spectra of the $\text{Mg}_{0.1}\text{Zn}_{0.9}\text{O}$ films with and without 500 nm-diameter silica nanospheres.

$\text{Mg}_{0.1}\text{Zn}_{0.9}\text{O}$ MSM-UPDs, which led more UV light to incident into the $\text{Mg}_{0.1}\text{Zn}_{0.9}\text{O}$ MSM-UPDs.

To exhibit the effect of the silica nanospheres antireflection layer on the photoresponsivity of the MSM-UPDs, the spectral photoresponsivity of passivated $\text{Mg}_{0.1}\text{Zn}_{0.9}\text{O}$ MSM-UPDs without and with antireflection layer is shown in Figures 5(a) and 5(b), respectively. The I - V characteristics of passivated $\text{Mg}_{0.1}\text{Zn}_{0.9}\text{O}$ MSM-UPDs without and with antireflection layer are shown in the inset of Figures 5(a) and 5(b), respectively. At bias voltage of 5 V, the photocurrent of passivated $\text{Mg}_{0.1}\text{Zn}_{0.9}\text{O}$ MSM-UPDs with antireflection layer illuminated by the UV light (wavelength = 340 nm and power = 40 μW) increased from 3.37 μA to 5.85 μA in comparison with passivated $\text{Mg}_{0.1}\text{Zn}_{0.9}\text{O}$ MSM-UPDs without antireflection layer. Besides, the UV-visible rejection ratio (R_{340}/R_{450}) of passivated $\text{Mg}_{0.1}\text{Zn}_{0.9}\text{O}$ MSM-UPDs with antireflection layer was increased from 5.50×10^3 to 1.44×10^4 . The enhancements in the photocurrent and the UV-visible rejection ratio of the MSM-UPDs were attributed to that the amount of the incident light was enhanced by the antireflection layer, which could induce more electron-hole pairs in the active layer.

To investigate the detectivity performance of the $\text{Mg}_{0.1}\text{Zn}_{0.9}\text{O}$ MSM-UPDs without and with PEC passivation and antireflection layer, the noise power density of $\text{Mg}_{0.1}\text{Zn}_{0.9}\text{O}$ MSM-UPDs without and with PEC passivation and antireflection layer as a function of frequency is shown in Figures 6(a) and 6(b), respectively. The frequency range is from 1 Hz to 1000 Hz. Obviously, the fitting curve of noise power density spectra for both MSM-UPDs was similar to $1/f^2$, as shown in Figures 6(a) and 6(b). This result indicated that the dominant noise of the $\text{Mg}_{0.1}\text{Zn}_{0.9}\text{O}$ MSM-UPDs was the generation-recombination noise, which implied that the presence of generation-recombination centers is caused by the carrier trapping in the device [25]. Consequently,

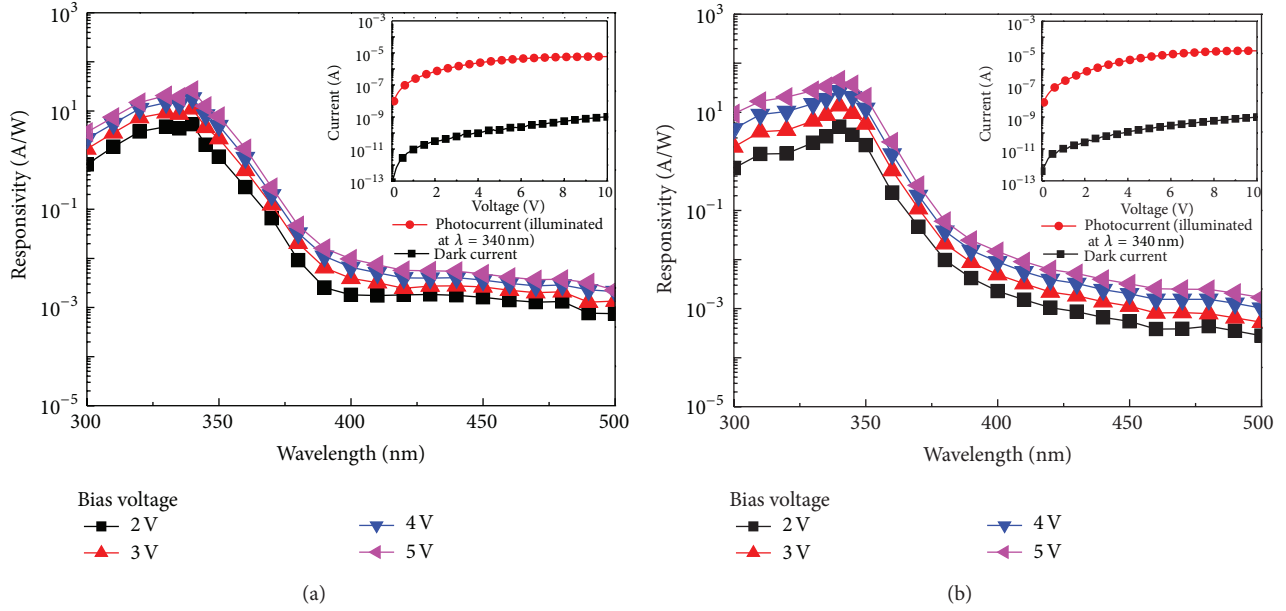


FIGURE 5: Photoresponsivity spectra of passivated $\text{Mg}_{0.1}\text{Zn}_{0.9}\text{O}$ MSM-UPDs (a) without and (b) with antireflection layer under various biases. The inset shows dark current and photocurrent versus bias voltage.

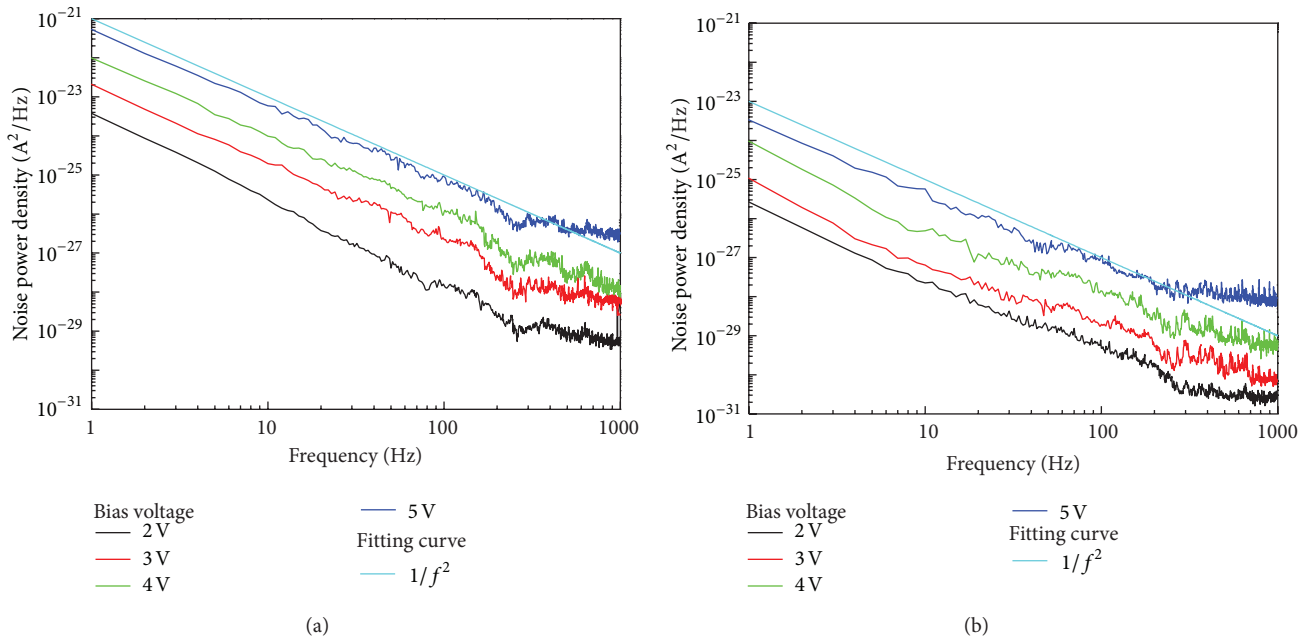


FIGURE 6: Noise power densities of the $\text{Mg}_{0.1}\text{Zn}_{0.9}\text{O}$ MSM-UPDs (a) without and (b) with PEC passivation and antireflection layer as a function of frequency for various bias voltages.

there was some generation-recombination centers existed in the $\text{Mg}_{0.1}\text{Zn}_{0.9}\text{O}$ films deposited by ALD system. In general, the noise equivalent power (NEP) and detectivity are commonly used to characterize the performance of the photodetector. The NEP was determined by the formula of $\text{NEP} = \sqrt{\langle I_n^2 \rangle} / R$, where $\langle I_n^2 \rangle$ is the mean square noise current and R is the photoresponsivity of MSM-UPDs. The

specific detectivity (D^*) is defined as $D^* = \sqrt{A\Delta f} / \text{NEP}$, where A is the optical sensitive area of the photodetectors and Δf is the bandwidth of 1000 Hz [25]. As shown in Figures 6(a) and 6(b), at bias voltage of 5 V, the NEP of the $\text{Mg}_{0.1}\text{Zn}_{0.9}\text{O}$ MSM-UPDs without and with PEC passivation and antireflection layer was 6.18×10^{-13} W and 2.60×10^{-13} W and the corresponding D^* was 5.11×10^{11} $\text{cmHz}^{1/2}\text{W}^{-1}$

and $1.21 \times 10^{12} \text{ cmHz}^{1/2}\text{W}^{-1}$, respectively. These results mentioned above confirmed that the PEC treatment and antireflection layer improved the performances of the $\text{Mg}_{0.1}\text{Zn}_{0.9}\text{O}$ MSM-UPDs. The improvement mechanism can be attributed to the excellent antireflection capability and effective passivation of dangling bonds on the surface of the $\text{Mg}_{0.1}\text{Zn}_{0.9}\text{O}$ films.

4. Conclusions

In this work, the PEC treatment and the antireflection layer were applied in the $\text{Mg}_{0.1}\text{Zn}_{0.9}\text{O}$ MSM-UPDs to enhance the performance. Since some dangling bonds remained on the $\text{Mg}_{0.1}\text{Zn}_{0.9}\text{O}$ surface after the ALD deposited process, the PEC treatment would passivate the $\text{Mg}_{0.1}\text{Zn}_{0.9}\text{O}$ surface by forming a $\text{Zn}(\text{OH})_2$ thin film and the dark current of the passivated $\text{Mg}_{0.1}\text{Zn}_{0.9}\text{O}$ MSM-UPDs decreased about one order in comparison with unpassivated $\text{Mg}_{0.1}\text{Zn}_{0.9}\text{O}$ MSM-UPDs. In addition, the antireflection layer was constructed by coating 500 nm-diameter silica nanospheres on the $\text{Mg}_{0.1}\text{Zn}_{0.9}\text{O}$ films. The reflectivity of the $\text{Mg}_{0.1}\text{Zn}_{0.9}\text{O}$ film with silica nanospheres antireflection layer decreased to about 7.0% at the wavelength of 340 nm. Besides, the passivated $\text{Mg}_{0.1}\text{Zn}_{0.9}\text{O}$ MSM-UPDs with antireflection layer were fabricated and characterized. Compared with the passivated $\text{Mg}_{0.1}\text{Zn}_{0.9}\text{O}$ MSM-UPDs without antireflection layer, the photocurrent and UV-visible ratio of passivated $\text{Mg}_{0.1}\text{Zn}_{0.9}\text{O}$ MSM-UPDs with antireflection layer were enhanced to $5.85 \mu\text{A}$ and 1.44×10^4 , respectively. The enhancements in the photocurrent and the UV-visible rejection ratio were attributed to the presence of the antireflection layer which effectively lead more UV light to incident into the active layer. Finally, the noise equivalent power of $2.60 \times 10^{-13} \text{ W}$ and the specific detectivity of $1.21 \times 10^{12} \text{ cmHz}^{1/2}\text{W}^{-1}$ for the passivated $\text{Mg}_{0.1}\text{Zn}_{0.9}\text{O}$ MSM-UPDs with antireflection layer had improved under a bias voltage of 5 V. The PEC passivation and silica nanospheres antireflection layer effectively enhanced the detectivity performance of $\text{Mg}_{0.1}\text{Zn}_{0.9}\text{O}$ MSM-UPDs, and it is promising the future application of UV photodetector.

Conflict of Interests

The authors declare that there is no conflict of interests regarding the publication of this paper.

Acknowledgments

This work was supported by the National Sciences Council of Taiwan under Grant NSC 101-2923-E-006-002-MY3 and NSC 102-2923-E-006-001-MY3 and the Advanced Optoelectronic Technology Center, National Cheng Kung University, Taiwan.

References

- [1] Q. Zheng, F. Huang, K. Ding et al., "MgZnO-based metal-semiconductor-metal solar-blind photodetectors on ZnO substrates," *Applied Physics Letters*, vol. 98, no. 22, Article ID 221112, pp. 221112-1-221112-3, 2011.
- [2] M. Liao and Y. Koide, "High-performance metal-semiconductor-metal deep-ultraviolet photodetectors based on homoepitaxial diamond thin film," *Applied Physics Letters*, vol. 89, no. 11, Article ID 113509, pp. 113509-1-113509-3, 2006.
- [3] L. Sun, J. Chen, J. Li, and H. Jiang, "AlGaIn solar-blind avalanche photodiodes with high multiplication gain," *Applied Physics Letters*, vol. 97, no. 19, Article ID 191103, pp. 191103-1-191103-3, 2010.
- [4] D. X. Zhao, Y. C. Liu, D. Z. Shen, Y. M. Lu, J. Y. Zhang, and X. W. Fan, "Photoluminescence properties of $\text{Mg}_x\text{Zn}_{1-x}\text{O}$ alloy thin films fabricated by the sol-gel deposition method," *Journal of Applied Physics*, vol. 90, no. 11, pp. 5561-5563, 2001.
- [5] S. Fujita, H. Tanaka, and S. Fujita, "MBE growth of wide band gap wurtzite MgZnO quasi-alloys with MgO/ZnO superlattices for deep ultraviolet optical functions," *Journal of Crystal Growth*, vol. 278, no. 1-4, pp. 264-267, 2005.
- [6] K. Ogata, K. Koike, T. Tanite et al., "ZnO and ZnMgO growth on *a*-plane sapphire by molecular beam epitaxy," *Journal of Crystal Growth*, vol. 251, no. 1-4, pp. 623-627, 2003.
- [7] T. Gruber, C. Kirchner, R. Kling, F. Reuss, and A. Waag, "ZnMgO epilayers and ZnO-ZnMgO quantum wells for optoelectronic applications in the blue and UV spectral region," *Applied Physics Letters*, vol. 84, no. 26, pp. 5359-1-5359-3, 2004.
- [8] K. Remashan, Y. S. Choi, S. J. Park, and J. H. Jang, "High performance MOCVD-grown ZnO thin-film transistor with a thin MgZnO layer at channel/gate insulator interface," *Journal of the Electrochemical Society*, vol. 157, no. 12, pp. H1121-H1126, 2010.
- [9] H. Y. Lee, M. Y. Wang, K. J. Chang, and W. J. Lin, "Ultraviolet photodetector based on $\text{Mg}_x\text{Zn}_{1-x}\text{O}$ thin films deposited by radio frequency magnetron sputtering," *IEEE Photonics Technology Letters*, vol. 20, no. 24, pp. 2108-2110, 2008.
- [10] H. Y. Lee, H. Y. Chang, L. R. Lou, and C. T. Lee, "P-i-n MgBeZnO-based heterostructured ultraviolet LEDs," *IEEE Photonics Technology Letters*, vol. 25, no. 18, pp. 1770-1773, 2013.
- [11] P. C. Wu, H. Y. Lee, and C. T. Lee, "Enhanced light emission of double heterostructured MgZnO/ZnO/MgZnO in ultraviolet blind light-emitting diodes deposited by vapor cooling condensation system," *Applied Physics Letters*, vol. 100, no. 13, Article ID 131116, pp. 131116-1-131116-3, 2012.
- [12] S. Choopun, R. D. Vispute, W. Yang, R. P. Sharma, T. Venkatesan, and H. Shen, "Realization of band gap above 5.0 eV in metastable cubic-phase $\text{Mg}_x\text{Zn}_{1-x}\text{O}$ alloy films," *Applied Physics Letters*, vol. 80, no. 9, pp. 1529-1531, 2002.
- [13] A. I. Belogorokhov, A. Y. Polyakov, N. B. Smirnov et al., "Lattice vibrational properties of ZnMgO grown by pulsed laser deposition," *Applied Physics Letters*, vol. 90, no. 19, Article ID 192110, pp. 192110-1-192110-3, 2007.
- [14] G. R. He and Y. J. Lin, "Current transport mechanism of heterojunction diodes based on the sol-gel p-type ZnO and n-type Si with H_2O_2 treatment," *Materials Chemistry and Physics*, vol. 136, no. 1, pp. 179-183, 2012.
- [15] C. L. Tsai, Y. J. Lin, P. H. Wu et al., "Induced increase in surface work function and surface energy of indium tin oxide-doped ZnO films by $(\text{NH}_4)_2\text{S}_x$ treatment," *Journal of Applied Physics*, vol. 101, no. 11, Article ID 113713, pp. 113713-1-113713-4, 2007.

- [16] C. T. Lee, Y. S. Chiu, S. C. Ho, and Y. J. Lee, "Investigation of a photoelectrochemical passivated ZnO-based glucose biosensor," *Sensors*, vol. 11, no. 5, pp. 4648–4655, 2011.
- [17] C. Y. Tseng, C. K. Lee, and C. T. Lee, "Performance enhancement of III–V compound multijunction solar cell incorporating transparent electrode and surface treatment," *Progress in Photovoltaics*, vol. 19, no. 4, pp. 436–441, 2011.
- [18] C. Y. Tseng, C. S. Lee, H. Y. Shin, and C. T. Lee, "Investigation of surface passivation on gas-based compound solar cell using photoelectrochemical oxidation method," *Journal of the Electrochemical Society*, vol. 157, no. 7, pp. H779–H782, 2010.
- [19] T. Glaser, A. Ihring, W. Morgenroth, N. Seifert, S. Schröter, and V. Baier, "High temperature resistant antireflective moth-eye structures for infrared radiation sensors," *Microsystem Technologies*, vol. 11, no. 2-3, pp. 86–90, 2005.
- [20] M. Ibn-Elhaj and M. Schadt, "Optical polymer thin films with isotropic and anisotropic nano-corrugated surface topologies," *Nature*, vol. 410, no. 6830, pp. 796–799, 2001.
- [21] B. T. Liu and W. D. Yeh, "Antireflective surface fabricated from colloidal silica nanoparticles," *Colloids and Surfaces A*, vol. 356, no. 1–3, pp. 145–149, 2010.
- [22] H. Y. Lee, C. T. Lee, and J. T. Yan, "Emission mechanisms of passivated single n-ZnO:In/i-ZnO/p-GaN- heterostructured nanorod light-emitting diodes," *Applied Physics Letters*, vol. 97, no. 11, Article ID 111111, pp. 111111-1–111111-3, 2010.
- [23] M. Klingenstein, J. Schneider, C. Moglestue et al., "Photocurrent gain mechanisms in metal-semiconductor-metal photodetectors," *Solid-State Electronics*, vol. 37, no. 2, pp. 333–340, 1994.
- [24] H. Jiang, N. Nakata, G. Y. Zhao et al., "Back-illuminated GaN metal-semiconductor-metal UV photodetector with high internal gain," *Japanese Journal of Applied Physics 2*, vol. 40, no. 5, pp. L505–L507, 2001.
- [25] C. H. Chen and C. T. Lee, "High detectivity mechanism of ZnO-based nanorod ultraviolet photodetectors," *IEEE Photonics Technology Letters*, vol. 25, no. 4, pp. 348–351, 2013.

Research Article

Performance Improvement of GaN-Based Flip-Chip White Light-Emitting Diodes with Diffused Nanorod Reflector and with ZnO Nanorod Antireflection Layer

Hsin-Ying Lee,¹ Yu-Chang Lin,¹ Yu-Ting Su,¹ Chia-Hsin Chao,² and Véronique Bardinal^{3,4}

¹ Department of Photonics, Advanced Optoelectronic Technology Center, National Cheng Kung University, Tainan 701, Taiwan

² Electronics and Optoelectronics Research Laboratories, Industrial Technology Research Institute, Hsinchu 300, Taiwan

³ CNRS, LAAS, 7 avenue du Colonel Roche, 31077 Toulouse, France

⁴ University of Toulouse, UPS, INSA, INP, ISAE, LAAS, 31077 Toulouse, France

Correspondence should be addressed to Hsin-Ying Lee; hylee@ee.ncku.edu.tw

Received 23 November 2013; Accepted 31 December 2013; Published 12 February 2014

Academic Editor: Sheng-Po Chang

Copyright © 2014 Hsin-Ying Lee et al. This is an open access article distributed under the Creative Commons Attribution License, which permits unrestricted use, distribution, and reproduction in any medium, provided the original work is properly cited.

The GaN-based flip-chip white light-emitting diodes (FCWLEDs) with diffused ZnO nanorod reflector and with ZnO nanorod antireflection layer were fabricated. The ZnO nanorod array grown using an aqueous solution method was combined with Al metal to form the diffused ZnO nanorod reflector. It could avoid the blue light emitted out from the Mg-doped GaN layer of the FCWLEDs, which caused more blue light emitted out from the sapphire substrate to pump the phosphor. Moreover, the ZnO nanorod array was utilized as the antireflection layer of the FCWLEDs to reduce the total reflection loss. The light output power and the phosphor conversion efficiency of the FCWLEDs with diffused nanorod reflector and 250 nm long ZnO nanorod antireflection layer were improved from 21.15 mW to 23.90 mW and from 77.6% to 80.1% in comparison with the FCWLEDs with diffused nanorod reflector and without ZnO nanorod antireflection layer, respectively.

1. Introduction

Recently, people have paid more and more attention to the problems of energy shortage and environment problems. Many research teams actively investigated how to improve energy saving and how to produce renewable energy. The white light-emitting diodes (WLEDs) are expected to be the promising green lighting sources and have been widely used in solid-state lighting and taken as the next generation lighting sources to replace the compact fluorescent lamp (CFL) and incandescent light. The WLEDs exhibit many superior advantages such as the long lifetime, high luminous intensity, energy saving, fast response, low heat dissipation, and high reliability. In general, there are three approaches that can be used to fabricate WLEDs: (1) using the blue light-emitting diodes (LEDs) to excite the yellow phosphor [1, 2], (2) using an ultraviolet (UV) LEDs to excite red, green, and blue phosphors [3, 4], and (3) mixing three primary colors of red, green, and blue LEDs [5]. The commercial WLEDs

were commonly integrated by the GaN-based blue LEDs with yellow phosphor ($Y_3Al_5O_{12} : Ce_3^+$ or $YAG : Ce_3^+$) layer. To augment the application of WLEDs, the development of high performance WLEDs is immediately needed. Since the properties of the GaN-based blue LEDs seriously affect the performances of WLEDs, how to improve the internal quantum efficiency and external quantum efficiency of the blue LEDs is a primary issue. In view of the significant progress of GaN-based epitaxial technology, the internal quantum efficiency of the GaN-based blue LEDs achieved the theoretical limit of 90%. However, the large difference of refractive index between the GaN-based semiconductor ($n_{GaN} = 2.4$) and the air ($n_{air} = 1$) led to the increase of total internal reflection and the Fresnel loss. Generally, several methods, such as die shape [6, 7], surface roughness [8, 9], photonic crystal [10, 11], reflector [12, 13], and antireflection coating layer [14], have been reported previously to overcome the undesired total internal reflection and Fresnel loss. Among these methods, the reflector exhibits

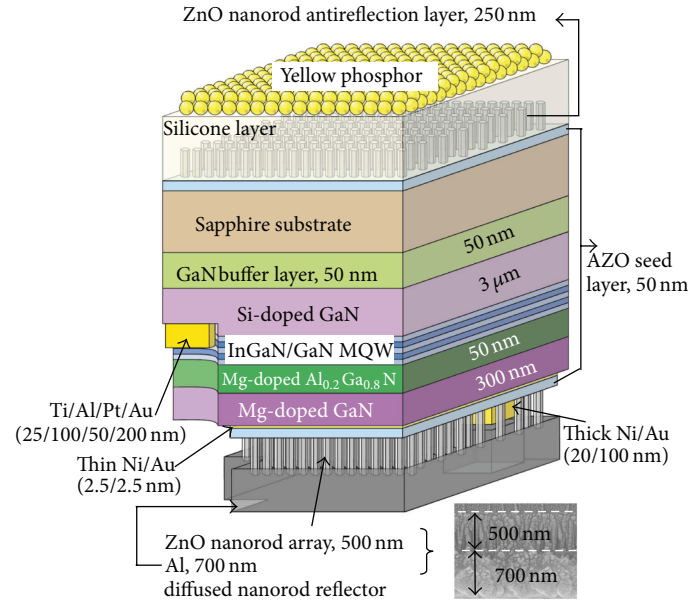


FIGURE 1: The schematic configuration of the GaN-based FCWLEDs with diffused nanorod reflector and with ZnO nanorod antireflection layer. The inset figure shows the morphology of diffused nanorod reflector.

several advantages including simple fabrication, low cost, and outstanding light extraction improvement of LEDs. In this work, to improve the light extraction efficiency of WLEDs, the designed diffused nanorod reflector constructed with the 700 nm thick Al metal and ZnO nanorod array with optimal rod length of 500 nm was used in the flip-chip white light-emitting diodes (FCWLEDs). The detail investigation of diffused nanorod reflector was shown in previous published paper [15]. The diffused nanorod reflector could effectively increase the reflection angle and enhance the light escaping probability from the semiconductor compared with the traditional flat reflector. Furthermore, to further improve the light extraction from the light-emitted side of the FCWLEDs, the ZnO nanorod arrays were also used as the antireflection layer. Finally, the yellow phosphor layer was coated on the ZnO nanorod antireflection layer by using the remote phosphor coating technique which possessed the uniformity and high color conversion efficiency.

2. Experiment Procedure

Figure 1 shows the schematic configuration of the GaN-based FCWLEDs with diffused nanorod reflector and with ZnO nanorod antireflection layer. A metal organic chemical vapor deposition (MOCVD) system was used to grow the epitaxial layers of the GaN-based blue LEDs. A 2.8 μm thick GaN buffer layer, a 4 μm thick Si-doped GaN layer ($n = 3 \times 10^{17} \text{ cm}^{-3}$), an undoped InGaN/GaN multiple quantum well (MQW) active layer, a 33 nm thick Mg-doped $\text{Al}_{0.2}\text{Ga}_{0.8}\text{N}$ layer ($p = 1 \times 10^{17} \text{ cm}^{-3}$), and a 150 nm thick Mg-doped GaN layer ($p = 3 \times 10^{17} \text{ cm}^{-3}$) were sequentially grown on the *c*-plane sapphire substrates. The InGaN/GaN MQW active layer was consisted of twelve pairs of 3 nm

thick $\text{In}_{0.2}\text{Ga}_{0.8}\text{N}$ well layer and 12.7 nm thick GaN barrier layer. The fabrication processes of the conventional GaN-based LEDs are as follows. The epitaxial layer with mesa ($300 \times 300 \mu\text{m}^2$) pattern protected by a 300 nm thick Ni metal mask was etched down to the Si-doped GaN layer by a reactive ion etching (RIE) system. After the mesa etching, the remaining Ni metal mask was removed using aqua regia. The *n*-electrode Ti/Al/Ti/Au (25/100/50/150 nm) was deposited using an electron-beam evaporator. Moreover, the *n*-electron was treated by a rapid thermal annealing (RTA) system with 850°C for 2 min in a pure N_2 ambient for obtaining the good ohmic contact performance [16]. Thin Ni/Au (2.5/2.5 nm) and thick Ni/Au (20/100 nm) metal contacts were deposited on Mg-doped GaN layer as the current spreading layer (CSL) and the *p*-electrode, respectively. Prior to thin Ni/Au metal deposition, a surface sulfurization treatment was performed to improve the contact performance between the thin Ni/Au metals and the Mg-doped GaN mesa region [17]. The *p*-type ohmic contact formation was carried out in an air ambient at 500°C for 10 min by a RTA system. When the conventional GaN-based LEDs were fabricated, and then the diffused nanorod reflector was sequentially fabricated. A 50 nm thick Al-doped ZnO (AZO) seed layer was deposited on the Ni/Au current spreading layer using a magnetron radio frequency sputtering system. A 500 nm long ZnO nanorod array was grown on the AZO seed layer using an aqueous solution method at 90°C. The chemical solution was mixed by 0.025 M zinc nitrate hexahydrate ($\text{Zn}(\text{NO}_3)_2 \cdot 6\text{H}_2\text{O}$) and 0.025 M hexamethylenetetramine ($\text{C}_6\text{H}_{12}\text{N}_4$). A 700 nm thick Al metal was then deposited on the top of the ZnO nanorod array using an electron-beam evaporator. The morphology of diffused nanorod reflector was carried out using scanning electron microscope (SEM) and is shown in the inset of Figure 1. Then a 50 nm thick AZO seed layer and

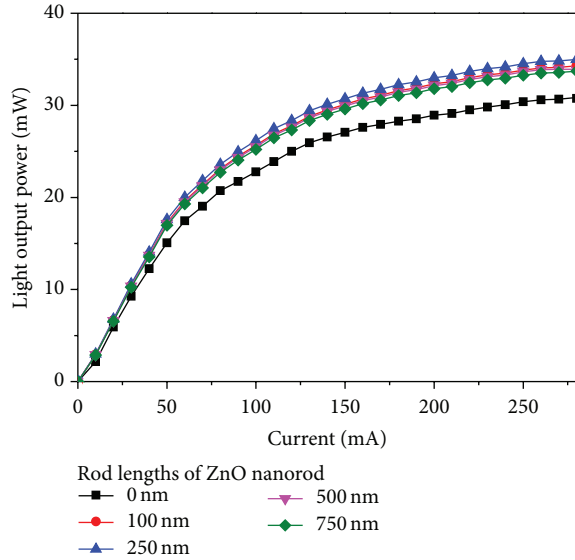


FIGURE 2: The light output power-current curves of the GaN-based FCLEDs with diffused nanorod reflector and with ZnO nanorod antireflection layers of various rod lengths.

ZnO nanorod arrays were sequentially deposited on the sapphire surface of the GaN-based FCLEDs with diffuse nanorod reflector. To find the optimal rod length of the ZnO nanorod in the array as the antireflection layer, the ZnO nanorods with various rod lengths of 0, 100, 250, 500, and 700 nm were grown. Finally, the remote phosphor coating technique was used to form the GaN-based FCWLEDs. A silicone layer was spread on the 250 nm long ZnO nanorod antireflection layer and a yellow phosphor layer was covered on the silicone layer to complete the fabrication process of the FCWLEDs with diffused nanorod reflector and with ZnO nanorod antireflection layer. The FCWLEDs with diffused nanorod reflector and 250 nm long ZnO nanorod antireflection layer were named FCWLED A, hereafter. The FCWLEDs with diffused nanorod reflector and without 250 nm long ZnO nanorod antireflection layer (named FCWLED B, hereafter) were also fabricated for comparison.

3. Result and Discussion

To find the optimal rod length of the ZnO nanorod in the antireflection layer, the performances of the GaN-based FCLEDs with diffused nanorod reflector and with 0, 100, 250, 500, and 750 nm long ZnO nanorod arrays were firstly investigated. Figure 2 shows the light output power-current ($L-I$) curves of the GaN-based FCLEDs with diffused nanorod reflector and with ZnO nanorod arrays of various rod lengths measured using an integrating sphere. As shown in Figure 2, the light output power of the FCLEDs with diffused nanorod reflector and with 250 nm long ZnO nanorod array was improved from 30.85 mW to 34.99 mW, compared with the FCLEDs with diffused nanorod reflector and without ZnO nanorod (i.e., 0 nm long ZnO nanorod) antireflection layer at an injection current of 280 mA. However, when the rod

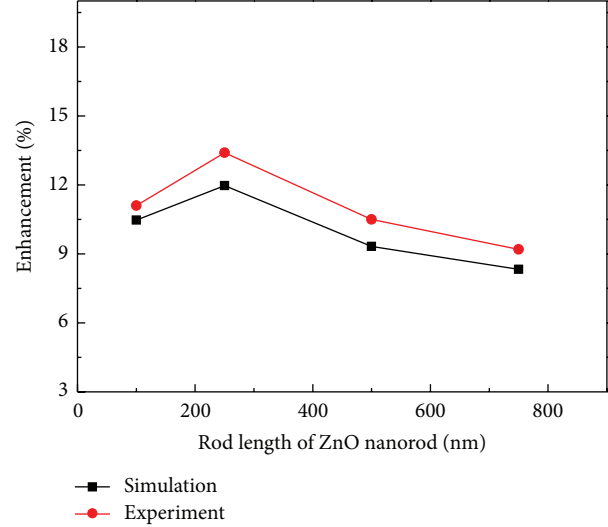


FIGURE 3: The simulating results and experimental results of the enhancement in the illumination efficiency and light output power for the resulting FCLEDs and FCWLEDs with ZnO nanorod antireflection layers of various rod lengths, in comparison with the resulting FCLEDs and FCWLEDs without ZnO nanorod antireflection layer, respectively.

length of the ZnO nanorod array was longer than 250 nm, the light output power decreased owing to the absorption of the ZnO nanorod array. To confirm the optimal rod length of the ZnO nanorod antireflection layer on the output side of the FCLEDs with diffused nanorod reflector, the standard optical software TracePro was also used to simulate the light propagated within the ZnO nanorod arrays of various rod lengths. Figure 3 shows the simulating results of an enhancement in the illumination efficiency for the FCLEDs with diffused nanorod reflector and with ZnO nanorod antireflection layer of various rod lengths, in comparison with the FCLEDs with diffused ZnO nanorod reflector and without ZnO nanorod antireflection layer. The illumination efficiency of the FCLEDs with diffused nanorod reflector and with 100, 250, 500, and 750 nm long ZnO nanorod antireflection layer showed an increase of 10.47%, 11.97%, 9.32%, and 8.33%, respectively. The experimental results of the enhanced proportion of the light output power for the resulted FCLEDs are also shown in Figure 3. The experimental results and the simulation results the similar tendency. In addition, the optimal effective refractive index of the antireflection layer can be determined by the formula of $(n_{\text{air}} \times n_{\text{GaN}})^{1/2}$, where n_{air} of 1.00 and n_{GaN} of 2.40 were the refractive indexes of air and n-GaN, respectively. The solution of the optimal effective refractive index of the antireflection layer was 1.55. In this work, the effective refractive index of the 250 nm long ZnO nanorod antireflection layer was measured by an ellipsometer and the value was about 1.57 which was similar to the optimal effective refractive index of the antireflection layer. Therefore, the rod length of 250 nm in the ZnO nanorod antireflection layer was the optimal length for the FCLEDs.

Figure 4 shows the electroluminescence (EL) spectra of the FCWLEDs with diffused nanorod reflector and with

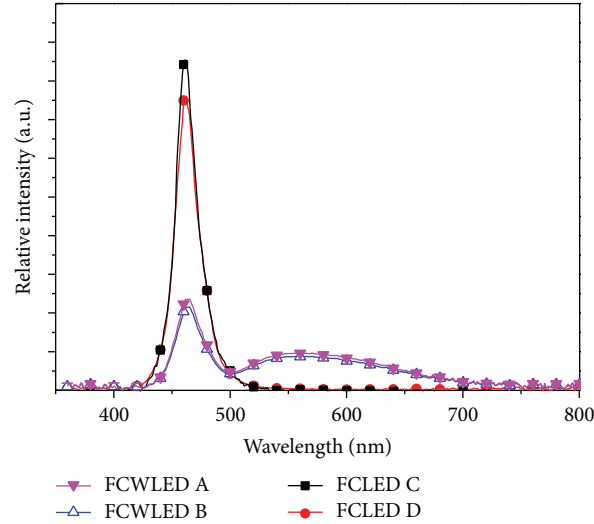


FIGURE 4: The electroluminescence spectra of the resulting FCWLEDs and FCLEDs with and without 250 nm long ZnO nanorod antireflection layer at an injection current of 20 mA.

and without 250 nm long ZnO nanorod antireflection layer (FCWLED A and FCWLED B) at an injection current of 20 mA. The EL spectra of the blue FCLEDs with diffused nanorod reflector and with 250 nm long ZnO nanorod antireflection layer (named FCLED C, hereafter) and the blue FCLEDs with diffused nanorod reflector and without 250 nm long ZnO nanorod antireflection layer (named FCLED D, hereafter) are also shown in Figure 4. As shown in Figure 4, the light-emission intensity of FCWLED A was larger than that of FCWLED B at the wavelength range from 400 nm to 700 nm. The light emission intensity of FCLED C and FCLED D had the same situation. The improvement of the light-emission intensity was attributed to the fact that the 250 nm long ZnO nanorod antireflection layer could effectively reduce the total reflection loss. The phosphor conversion efficiency η of the FCWLEDs was defined as

$$\eta = \frac{P_{\text{phosphor}}}{P_p - P_{\text{phosphor}}}, \quad (1)$$

where P_p is the optical power emitted from the blue FCLEDs without phosphor layer and P_{phosphor} is the optical power converted from the phosphor layer. Compared with the FCWLED B, the phosphor conversion efficiency of FCWLED A operated at an injection current of 20 mA was improved from 77.6% to 80.1%. The improvement was attributed to that the ZnO nanorod antireflection layer could reduce the light total reflection at the sapphire surface, which could guide more blue light to pump the phosphor layer. Generally, the phosphor conversion efficiency was varied by the injection current of the LEDs. Consequently, the EL spectra of the FCLED C and FCWLED A at various injection currents were measured and are shown in Figures 5(a) and 5(b), respectively. Figure 6 shows the phosphor conversion efficiency of FCWLED A at various injection currents which estimated by (1). The phosphor conversion efficiency of FCWLED A was enhanced with an increase of the injection current;

a maximum value of 92.5% was obtained as the FCWLED A operated at a current of 80 mA. This phenomenon was attributed to that the phosphor conversion efficiency reached saturation at an injection current of 80 mA. Therefore, when the injection current was more than 80 mA, the phosphor conversion efficiency decreased owing to the excess blue light directly emitted out the FCWLEDs or the excess photons multi scattered with the phosphor and were absorbed inside the FCWLEDs. The $L-I$ curves of FCWLED A and FCWLED B were also measured using an integrating sphere system. The light output power of FCWLED A and FCWLED B was 23.90 mW and 21.15 mW, respectively, at an injection current of 280 mA.

Figure 7 shows the chromaticity diagram of FCWLED A and FCWLED B at an injection current of 80 mA. As shown in Figure 7, the chromaticity coordinate of the emission of the corresponding LEDs exhibited the same coordinates of 0.335 and 0.333, which demonstrated that the emitted light was a white light.

4. Conclusions

The light output power and phosphor conversion efficiency of the FCWLEDs were successfully improved by using the diffused nanorod reflector and the ZnO nanorod antireflection layer. The diffused nanorod reflector constructed by the 500 nm long ZnO nanorod arrays and the high reflective Al metal could effectively enhance the probability of light reflectivity from the bottom of the FCWLEDs. Moreover, according to the experimental results and the simulation results, the optimal 250 nm long ZnO nanorods grown on the output side of the LEDs as the antireflection layer could guide more blue light and could excite more phosphor to enhance the phosphor conversion efficiency. The light output power of the FCWLEDs with diffused nanorod reflector and with ZnO nanorod antireflection layer was enhanced 13.0%

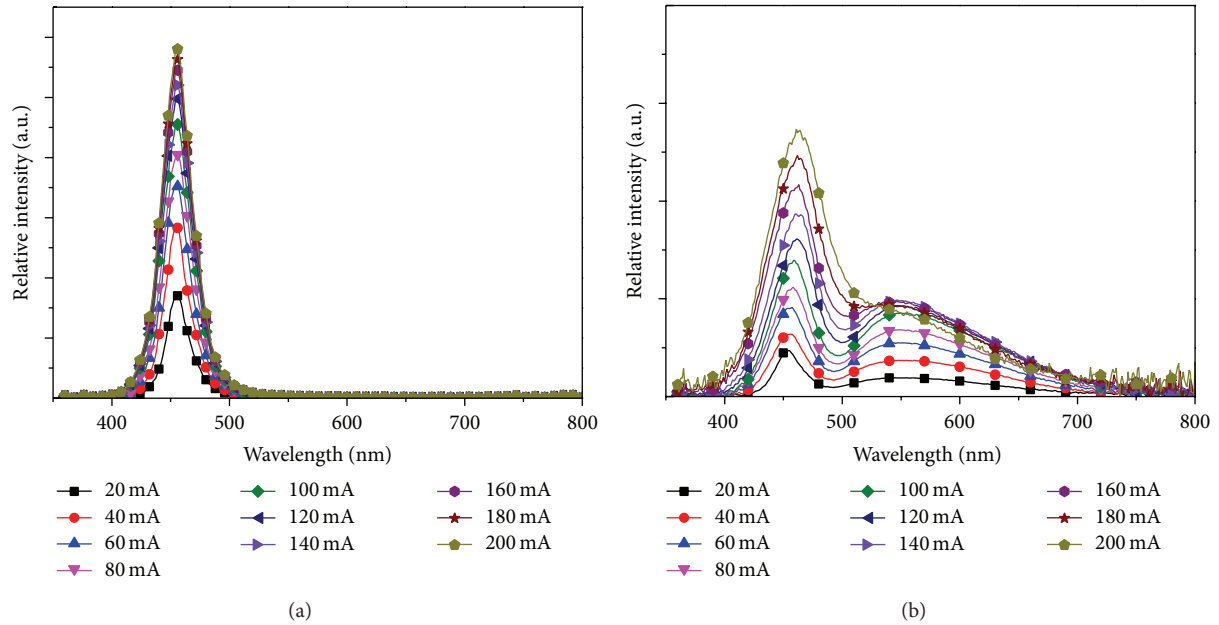


FIGURE 5: The electroluminescence spectra of (a) FCLED C and (b) FCWLED A at various injection currents.

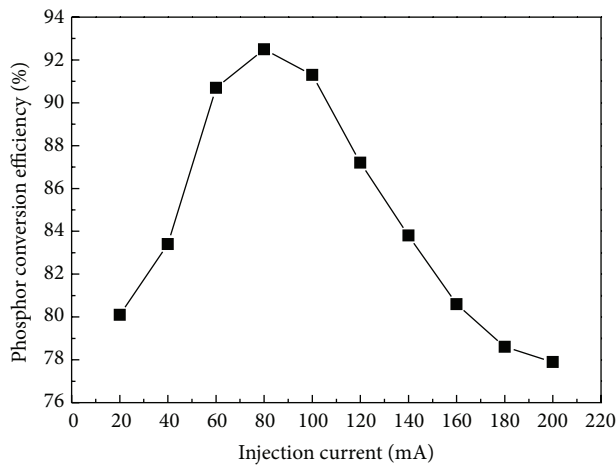


FIGURE 6: The phosphor conversion efficiency of FCWLED A at various injection currents.

in comparison with the FCWLEDs with diffused nanorod reflector and without with ZnO nanorod antireflection layer at injection current of 280 mA. The phosphor conversion efficiency was also improved by 2.5%.

Conflict of Interests

The authors declare that there is no conflict of interests regarding the publication of this paper.

Acknowledgments

This work was supported by the Industrial Technology Research Institute, Bureau of Energy, Ministry of Economic

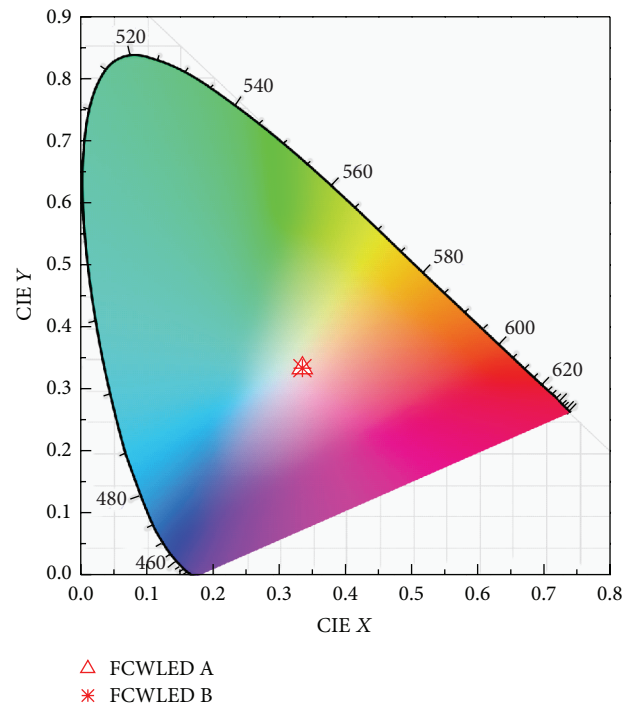


FIGURE 7: The chromaticity diagram of FCWLED A and FCWLED B.

Affairs of Taiwan, Contract no. 102-E0605, the National Sciences Council of Taiwan under Grant NSC-101-2923-E-006-004-MY2, and the Advanced Optoelectronic Technology Center, National Cheng Kung University, Taiwan.

References

- [1] H. Rao, W. Wang, X. L. Wan et al., "An improved slurry method of self-adaptive phosphor coating for white pc-LED packaging," *Journal of Display Technology*, vol. 9, no. 6, pp. 453–458, 2013.
- [2] C. T. Lee and T. J. Wu, "Light distribution and light extraction improvement mechanisms of remote GaN-based white light-emitting-diodes using ZnO nanorod array," *Journal of Luminescence*, vol. 137, no. 5, pp. 143–147, 2013.
- [3] Z. Y. Mao, Y. C. Zhu, L. Gan et al., "Tricolor emission $\text{Ca}_3\text{Si}_2\text{O}_7$: Ln (Ln = Ce, Tb, Eu) phosphors for near-UV white light-emitting-diode," *Journal of Luminescence*, vol. 134, no. 2, pp. 148–153, 2013.
- [4] S. H. Park, K. H. Lee, S. Unithrattil, H. S. Yoon, H. G. Jang, and W. B. Im, "Melilite-structure CaYAl_3O_7 : Eu^{3+} phosphor: structural and optical characteristics for near-UV LED based white light," *The Journal of Physical Chemistry*, vol. 116, no. 51, pp. 26850–26856, 2012.
- [5] S. Muthu, F. J. P. Schuurmans, and M. D. Pashley, "Red, green, and blue LEDs for white light illumination," *IEEE Journal on Selected Topics in Quantum Electronics*, vol. 8, no. 2, pp. 333–338, 2002.
- [6] D. S. Kuo, S. J. Chang, T. K. Ko, C. F. Shen, S. J. Hon, and S. C. Hung, "Nitride-based LEDs with phosphoric acid etched undercut sidewalls," *IEEE Photonics Technology Letters*, vol. 21, no. 8, pp. 510–512, 2009.
- [7] S. E. Brinkley, C. L. Keraly, J. Sonoda et al., "Chip shaping for light extraction enhancement of bulk *c*-plane light-emitting diodes," *Applied Physics Express*, vol. 5, no. 3, Article ID 032104, 3 pages, 2012.
- [8] H. Y. Lee, X. Y. Huang, and C. T. Lee, "Light output enhancement of GaN-based roughened LEDs using bias-assisted photo-electrochemical etching method," *Journal of the Electrochemical Society*, vol. 155, no. 10, pp. H707–H709, 2008.
- [9] C. C. Lin and C. T. Lee, "Enhanced light extraction of GaN-based light emitting diodes using nanorod arrays," *Electrochemical and Solid-State Letters*, vol. 13, no. 8, pp. H278–H280, 2010.
- [10] D. H. Kim, C. O. Cho, Y. G. Roh et al., "Enhanced light extraction from GaN-based light-emitting diodes with holographically generated two-dimensional photonic crystal patterns," *Applied Physics Letters*, vol. 87, no. 20, Article ID 203508, 3 pages, 2005.
- [11] H. K. Cho, J. Jang, J. H. Choi et al., "Light extraction enhancement from nanoimprinted photonic crystal GaN-based blue lightemitting diodes," *Optics Express*, vol. 14, no. 19, pp. 8654–8660, 2006.
- [12] Y. C. Chang, J. K. Liou, and W. C. Liu, "Improved light extraction efficiency of a high-power GaN-Based light-emitting diode with a three-dimensional-photonic crystal (3-D-PhC) backside reflector," *IEEE Electron Device Letters*, vol. 34, no. 6, pp. 777–779, 2013.
- [13] N. Lobo, H. Rodriguez, A. Knauer et al., "Enhancement of light extraction in ultraviolet light-emitting diodes using nanopixel contact design with Al reflector," *Applied Physics Letters*, vol. 96, no. 8, Article ID 081109, 3 pages, 2010.
- [14] X. Yan, M. Shatalov, T. Saxena, and M. S. Shur, "Deep-ultraviolet tailored- and low-refractive index antireflection coatings for light-extraction enhancement of light-emitting diodes," *Journal of Applied Physics*, vol. 113, no. 16, Article ID 163105, 5 pages, 2013.
- [15] C. T. Lee and C. Y. Chuang, "Light extraction enhancement of GaN-based flip-chip light-emitting diodes using diffused nanorod reflector," *Applied Physics Express*, vol. 5, no. 11, Article ID 112104, 3 pages, 2012.
- [16] C. T. Lee and H. W. Kao, "Long-term thermal stability of Ti/Al/Pt/Au Ohmic contacts to n-type GaN," *Applied Physics Letters*, vol. 76, no. 17, pp. 2364–2366, 2000.
- [17] C. S. Lee, Y. J. Lin, and C. T. Lee, "Investigation of oxidation mechanism for ohmic formation in Ni/Au contacts to p-type GaN layers," *Applied Physics Letters*, vol. 79, no. 23, pp. 3815–3817, 2001.

Research Article

P3HT:PCBM Incorporated with Silicon Nanoparticles as Photoactive Layer in Efficient Organic Photovoltaic Devices

Shang-Chou Chang,¹ Yu-Jen Hsiao,² and To-Sing Li¹

¹ Department of Electrical Engineering, Kun Shan University, Da-Wan Road, Tainan City 71003, Taiwan

² National Nano Device Laboratories, Tainan City 74147, Taiwan

Correspondence should be addressed to Shang-Chou Chang; jchang@mail.ksu.edu.tw

Received 17 October 2013; Revised 28 November 2013; Accepted 1 December 2013

Academic Editor: Sheng-Po Chang

Copyright © 2013 Shang-Chou Chang et al. This is an open access article distributed under the Creative Commons Attribution License, which permits unrestricted use, distribution, and reproduction in any medium, provided the original work is properly cited.

Silicon nanoparticles doped poly(3-hexylthiophene) and [6,6]-phenyl C61-butyric acid methyl ester blends (P3HT:PCBM: Si NP) have been produced as the photoactive layer of organic photovoltaic devices (OPVs). The silicon nanoparticles' size is between 80 and 100 nm checked by transmission electron microscope (TEM). The 0.35 wt% Si NP doping OPVs exhibit higher power conversion efficiency (PCE) than other OPVs. The PCE of the OPVs increases from 3.01% to 3.38% mainly due to increasing short-circuit current density from 8.38 to 9.48 mA/cm², while the open-circuit voltage remains the same. The Si NP can provide extra exciton separation and electron pathways in hybrid solar cells.

1. Introduction

Solar energy has been greatly cared as a renewable energy source. Organic photovoltaic devices are attractive low-cost alternative compared with thin-film solar cells (single-poly-crystalline and amorphous thin films) and compound-based solar cells (copper indium gallium (di)selenide (CIGS), GaAs, CdTe). They are easily produced and large-area modules can be made with roll-to-roll process.

The PCE of OPVs with poly(3-hexylthiophene) (P3HT) and [6,6]-phenyl C61-butyric acid methyl ester (PCBM) blend as the photoactive layer is high compared with that of other OPVs so far. The P3HT provides the pi-orbit electron excitation during the photovoltaic process [1]. The PCBM usually acts an electron transport material in polymer solar cells.

The PCE of OPVs under AM 1.5 conditions has exceeded 7.4% [2]. The PCE of OPVs can be improved by doping nanomaterials like single-walled carbon nanotubes [3], multi-walled carbon nanotubes [4], nanodiamond [5], Fe₃O₄ magnetic nanoparticles [6], and ZnO nanorods [7]. Nanomaterials, which can be used to make superstrong metals [8], have become popular as semiconductor nanocrystals and solar cell materials due to their high surface to volume ratio,

quantum confinement [9], quantum size [10], and small size effect [5].

Silicon, which has been successfully applied in solar cell and microelectronics industry, is a potential candidate for polymer-nanomaterials solar cells owing to its abundance, nontoxicity, and strong ultraviolet absorption. Doping Si NP into polymer materials acting as the photoactive layer of OPVs may increase the electron collection rate in the mixture. This work investigates the effect of employing P3HT:PCBM:Si NP as photoactive layer in OPVs on their electrical and optical properties.

2. Experimental Procedure

Organic photovoltaic devices were fabricated on indium tin oxide (ITO) coated glass substrates. The ITO glass substrate was ultrasonic cleaned in acetone, isopropanol, and deionized water in sequence to remove contaminants, then dried by nitrogen. After that, the ITO glass substrates were oxygen plasma cleaned by an inductively coupled plasma system to make the ITO surface hydrophilic. A 40-nm-thick layer of poly(3,4-ethylenedioxythiophene) poly(styrenesulfonate) (PEDOT:PSS, Baytron P 4083) was spin-coated onto the ITO

glass substrate with 2600 rpm spin speed and then baked at 120°C for 30 minutes.

The photoactive layer was made of P3HT:PCBM:Si NP dissolved in 1,2-dichlorobenzene. The P3HT (FEM. Inc.) and PCBM (Nano-C) were 10:8 wt% in proportion. The Si NP (ITRI Taiwan) of size 80–100 nm prepared by the vibrating milled solid-state reaction was used. Various concentration of Si NP was processed in P3HT:PCBM:Si NP. The P3HT:PCBM:Si NP blend film was spin-coated on ITO glass substrate with 1500 rpm spin speed in a glove box. The P3HT:PCBM:Si NP blend film was then annealed at 120°C for 10 min to reduce contact resistance of electrodes. Finally, a 120-nm-thick Ca/Al electrode was deposited onto the P3HT:PCBM:Si NP blend film through a shadow mask by thermal evaporation. The devices were sealed by a glass slide coated with UV glue after UV light irradiation. The device area was about 0.04 cm². Subsequently, the P3HT:PCBM:Si NP blend film was measured with TEM. The current density-voltage measurements were obtained by using a source meter (Keithley, 2410) and a solar simulator (TELTEC) with an AM 1.5 illumination and intensity of 100 mW cm⁻². For external quantum efficiency (EQE) measurements, a xenon lamp (Oriel, 66150, 75 W) was used as the light source, and a chopper and lock-in amplifier were used for phase-sensitive detection. Absorption spectra were measured by an optical spectrometer (Hitachi, U-4100).

3. Results and Discussion

Figure 1 shows the device structure of the produced OPVs, in which P3HT:PCBM:Si NP is the photoactive layer of the device. Calcium was added to the metal electrodes to improve the fill factor (FF) and the open-circuit voltage (V_{oc}) [11]. The organic layer of anhydrous molecular residues must be controlled because of calcium oxidizes if it is exposed to oxygen and moisture [12]. The spherical morphology of Si NP was clearly observed, as evidenced from TEM images in Figure 2. It possesses a uniform dispersion with average diameter about 80–100 nm.

A previous study found that the crystallization, inter-chain interaction, and phase separation of photoactive layers depend on the composite mixture and its doping concentration of nanomaterials. Similar results were obtained for P3HT:PCBM:nanodiamond layers with various nanodiamond concentrations [5]. Phase segregation increases with increasing contact area between aggregated particles. Therefore, doping Si nanoparticles may cause phase separation with high roughness for the OPVs. The Si NP plays an active role in exciton dissociation due to its greater surface-area-to-volume ratio and wider band gap [13]. Furthermore, short-circuit current density (J_{sc}) increases with concentration of Si NP. However, the current could be limited by a bottleneck in the hole transport material, P3HT, or the efficiency of exciton dissociation could decrease rapidly when the concentration of Si NP reaches a certain limit.

The photovoltaic characteristics, namely, V_{oc} , J_{sc} , fill factor (FF), and PCE, for OPVs with different concentration of

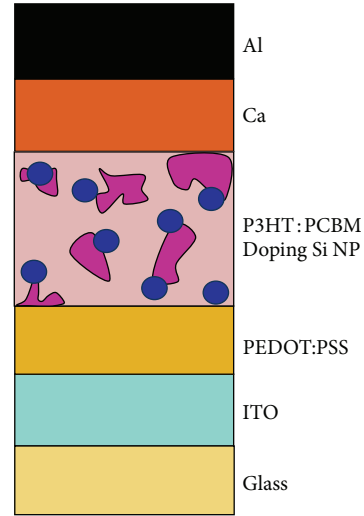


FIGURE 1: The structure of the P3HT:PCBM:Si NP organic photovoltaic device.

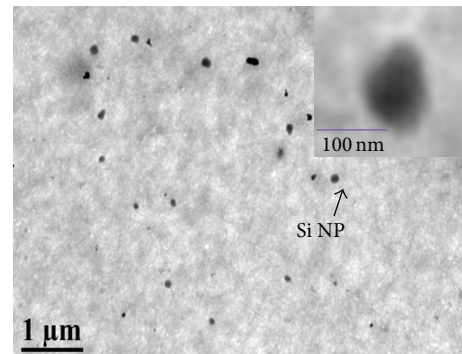


FIGURE 2: TEM micrograph of P3HT:PCBM:0.35 wt % Si NP.

TABLE 1: The photovoltaic characteristics, namely V_{oc} , J_{sc} , FF, and PCE, for P3HT:PCBM:Si NP OPVs with various Si NP concentration.

Concentration of Si NP (wt%)	V_{oc} (V)	J_{sc} (mA/cm ²)	FF	PCE (%)
0	0.599	8.38	60.12	3.01
0.07	0.599	8.54	61.08	3.12
0.35	0.599	9.48	60.42	3.38
0.70	0.649	6.56	53.17	2.27

doping Si NP, are given in Table 1. Figure 3 shows the current-voltage (I - V) characteristics of OPVs measured under an illumination intensity of 100 Mw cm⁻². The J_{sc} and PCE in OPVs rise with Si NP doping concentration till 0.35 wt%. The 0.35 wt% Si NP doping into the photoactive layer results in an increment in J_{sc} from 8.38 to 9.48 mA cm⁻². The PCE of the OPVs grows from 3.01 to 3.38%. The Si NP doping increases the donor/acceptor interface area for charge separation and shortens the electron transfer path in P3HT:PCBM, which improves the J_{sc} and PCE. However, the PCE decreases when

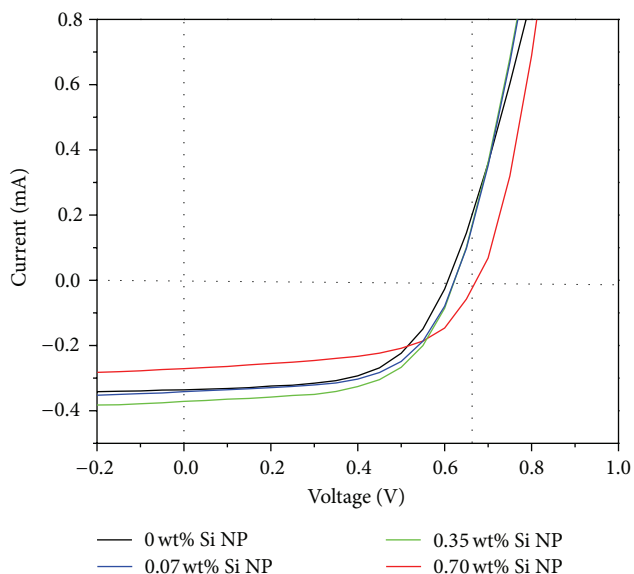


FIGURE 3: The current-voltage (I - V) characteristics of for P3HT:PCBM:Si NP OPVs with various Si NP concentration.

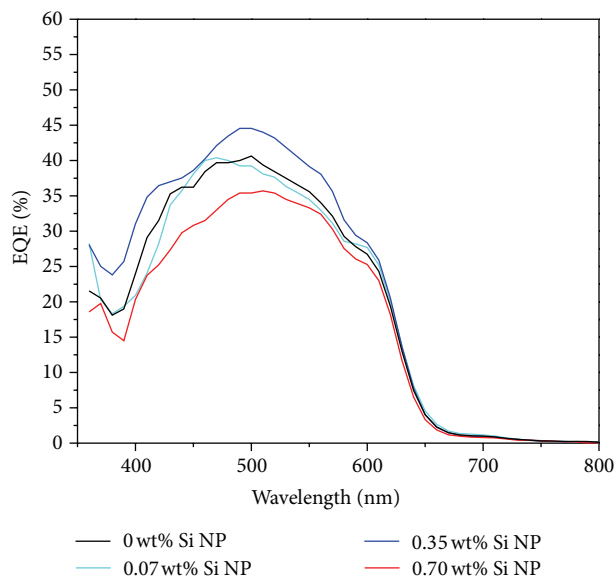


FIGURE 4: The EQE spectra for P3HT:PCBM:Si NP OPVs with various Si NP concentration.

the concentration of Si NP exceeds 0.35 wt%, probably due to rising leakage current [14].

The EQE spectra for OPVs with different concentration of doping Si NP are shown in Figure 4. Although all EQE spectra are similar in shape, the value of EQE spectra for the OPVs containing 0.35 wt% Si NP is the highest among those of all OPVs. For example, the EQE maximum for the OPVs containing 0.35 wt% Si NP is 44.5% at 500 nm whereas that containing 0.7 wt% Si NP is 35.4% at the same wavelength. The difference is due to an increased rate of electron collection in the OPVs. No obvious change in optical absorption spectra was observed when the active

layer was blended with P3HT:PCBM:Si NP. However, the peak wavelengths at approximately 340 nm may attribute to the PCBM band and those at approximately 400–650 nm attribute to the pristine P3HT band in the absorption spectra [15].

4. Conclusion

The OPVs with P3HT:PCBM:Si NP as the photoactive layer have been produced. The Si NP is well dispersed into the P3HT:PCBM polymer matrix. Doping Si NP increases the J_{sc} in OPVs, thus increasing PCE via faster electron collection rate. The highest measured PCE is 3.38%, corresponding to OPVs containing 0.35 wt% Si NP among those of all OPVs. The Si NP can provide extra exciton separation and electron pathways in OPVs, which increases the J_{sc} and PCE.

Acknowledgment

The authors would like to thank the National Science Council of Taiwan for financially supporting this research under Grant NSC 100-2628-E-151-003-MY3 and NSC 102-2221-E-168-037.

References

- [1] H. S. Nalwa, *Handbook of Organic Conductive Molecules and Polymers, Volume 3, Conductive Polymers: Spectroscopy and Physical Properties*, Wiley, 1997.
- [2] Y. Liang, Z. Xu, J. Xia et al., "For the bright future-bulk heterojunction polymer solar cells with power conversion efficiency of 7.4%," *Advanced Materials*, vol. 22, no. 20, pp. E135–E138, 2010.
- [3] R. K. Singh, J. Kumar, A. Kumar, V. Kumar, R. Kant, and R. Singh, "Poly(3-hexylthiophene): functionalized single-walled carbon nanotubes: (6,6)-phenyl-C61-butyric acid methyl ester composites for photovoltaic cell at ambient condition," *Solar Energy Materials and Solar Cells*, vol. 94, no. 12, pp. 2386–2394, 2010.
- [4] M. Wu, Y. Lin, S. Chen et al., "Enhancing light absorption and carrier transport of P3HT by doping multi-wall carbon nanotubes," *Chemical Physics Letters*, vol. 468, no. 1–3, pp. 64–68, 2009.
- [5] Y. Hsiao, T. Fang, L. Ji, Y. Lee, and B. Dai, "Size effect of nanodiamonds on P3HT:PCBM heterojunction solar cells," *Electrochemistry Communications*, vol. 18, no. 1, pp. 4–7, 2012.
- [6] W. Zhang, Y. Xu, H. Wang, C. Xu, and S. Yang, " Fe_3O_4 nanoparticles induced magnetic field effect on efficiency enhancement of P3HT:PCBM bulk heterojunction polymer solar cells," *Solar Energy Materials and Solar Cells*, vol. 95, no. 10, pp. 2880–2885, 2011.
- [7] S. V. Bhat, A. Govindaraj, and C. N. R. Rao, "Hybrid solar cell based on P3HT-ZnO nanoparticle blend in the inverted device configuration," *Solar Energy Materials and Solar Cells*, vol. 95, no. 8, pp. 2318–2321, 2011.
- [8] R. Valiev, "Materials science: nanomaterial advantage," *Nature*, vol. 419, no. 6910, pp. 887–889, 2002.
- [9] S. Q. Feng, D. P. Yu, H. Z. Zhang, Z. G. Bai, and Y. Ding, "The Growth mechanism of silicon nanowires and their quantum confinement effect," *Journal of Crystal Growth*, vol. 209, no. 2–3, pp. 513–517, 2000.

- [10] A. C. Varonides, "Quantum size effects in amorphous Si superlattice solar cells," *Renewable Energy*, vol. 33, no. 2, pp. 273–276, 2008.
- [11] Q. Liu, Z. Liu, X. Zhang et al., "Polymer photovoltaic cells based on solution-processable graphene and P3HT," *Advanced Functional Materials*, vol. 19, no. 6, pp. 894–904, 2009.
- [12] B. Paci, A. Generosi, V. R. Albertini, P. Perfetti, R. de Bettignies, and C. Sentein, "Time-resolved morphological study of organic thin film solar cells based on calcium/aluminium cathode material," *Chemical Physics Letters*, vol. 461, no. 1–3, pp. 77–81, 2008.
- [13] U. R. Kortshagen, C. Liu, and Z. C. Holman, "Hybrid solar cells from P3HT and silicon nanocrystals," *Nano Letters*, vol. 9, no. 1, pp. 449–452, 2009.
- [14] Y. Liu, C. Liu, and Y. Liu, "Investigation on fluorescence quenching of dyes by graphite oxide and graphene," *Applied Surface Science*, vol. 257, no. 13, pp. 5513–5518, 2011.
- [15] G. Li, Y. Yao, H. Yang, V. Shrotriya, G. Yang, and Y. Yang, "Solvent annealing effect in polymer solar cells based on poly(3-hexylthiophene) and methanofullerenes," *Advanced Functional Materials*, vol. 17, no. 10, pp. 1636–1644, 2007.

Research Article

Improvement of Charge-Discharge Characteristics of the Mg-Ni Powder Electrodes at 55°C

Kuan-Jen Chen,¹ Fei-Yi Hung,² Truan-Sheng Lui,² and Ren-Syuan Xiao²

¹ The Instrument Center, National Cheng Kung University, Tainan 701, Taiwan

² Department of Materials Science and Engineering, National Cheng Kung University, Tainan 701, Taiwan

Correspondence should be addressed to Fei-Yi Hung; fyhung@mail.ncku.edu.tw

Received 17 September 2013; Revised 15 November 2013; Accepted 18 November 2013

Academic Editor: Ting-Jen Hsueh

Copyright © 2013 Kuan-Jen Chen et al. This is an open access article distributed under the Creative Commons Attribution License, which permits unrestricted use, distribution, and reproduction in any medium, provided the original work is properly cited.

Magnesium-nickel (Mg-Ni) powders are used as the anode materials for secondary lithium (Li) ion batteries. Mg-Ni powders with ratios of 1:1 (Mg: Ni) are prepared and their structure and electrochemical behavior at room temperature and 55°C are investigated. The results show that adding Ni powders to Mg powders can reduce the charge-discharge capacities and improve cycling life. In charge-discharge cycle testing at 55°C, the Li ion concentration gradually increased with increasing the duration of electrochemical reactions, indicating that the charge-discharge capacities increase with increment of cycling number. The formation of a solid electrolyte interface (SEI) layer restrains Mg ions from dissolving into the electrolyte and thus improves the charge-discharge capacities at high temperature.

1. Introduction

Magnesium (Mg) was used as a negative electrode in lithium (Li) ion secondary batteries due to its high theoretic capacity [1]. However, pure metal electrodes have a serious problem of volume expansion during cycling that resulted in poor cycling life. Adding poor-activity elements into a pure metal matrix reduces the volume expansion of an electrode. Studies on alloy electrode materials have focused on Sn- [2], Si- [3], and Mg-based alloys [4, 5]. Of the electrodes based on these alloys, Mg-based ones are one of the potential material in Li-ion battery applications. Many studies have indicated that Mg-based alloy electrode, such as Mg-Li, Mg-C, and Mg-Ni alloys, can enhance battery performance via various electrochemical mechanisms [4, 6–8]. Adding Li into Mg can enhance the efficiency of lithiation and delithiation [9] and Mg-C alloys can restrain the growth of the solid electrolyte interface (SEI) layer [4]. In the present study, Mg-Ni powder electrodes were fabricated to suppress the volume change of the electrode and increase oxidation resistance.

Mg-Ni material is a typical active/nonactive alloy system that can effectively suppress the volume expansion and improve battery cycling life. Many researchers have prepared

Mg-Ni alloys using the mechanical grinding method [10, 11]. However, the proportion of Mg to Ni is not easy to control, and Mg-Ni alloys with excessive Ni have reduced charge-discharge capacity [12]. In addition, Mg easily oxidized to form MgO phases during mechanical milling [13]. The formation of MgO phases may degrade the cycling performance of batteries. In this study, Mg powder was directly mixed with Ni powder in a glove box. Because the particle size of Mg powder and that of Ni powder is very different, alloying effect prevents oxidation problems [14].

This method is simple and the composition ratio of elements can be easily controlled. Portable electronic devices generate heat during operation, which affects Li-ion battery performance. Thus, the charge-discharge characteristics of batteries at high temperature are an important issue. However, few studies have investigated the thermal effects on the charge-discharge characteristics of Mg-Ni compound electrodes.

This study synthesizes Mg-Ni powders and investigates the structural and electrochemical characteristics of Mg-Ni alloy electrodes at room temperature and 55°C. The relations of electrical resistance and electrochemical reaction cycles of Mg-Ni electrodes at high temperature are derived. The metal

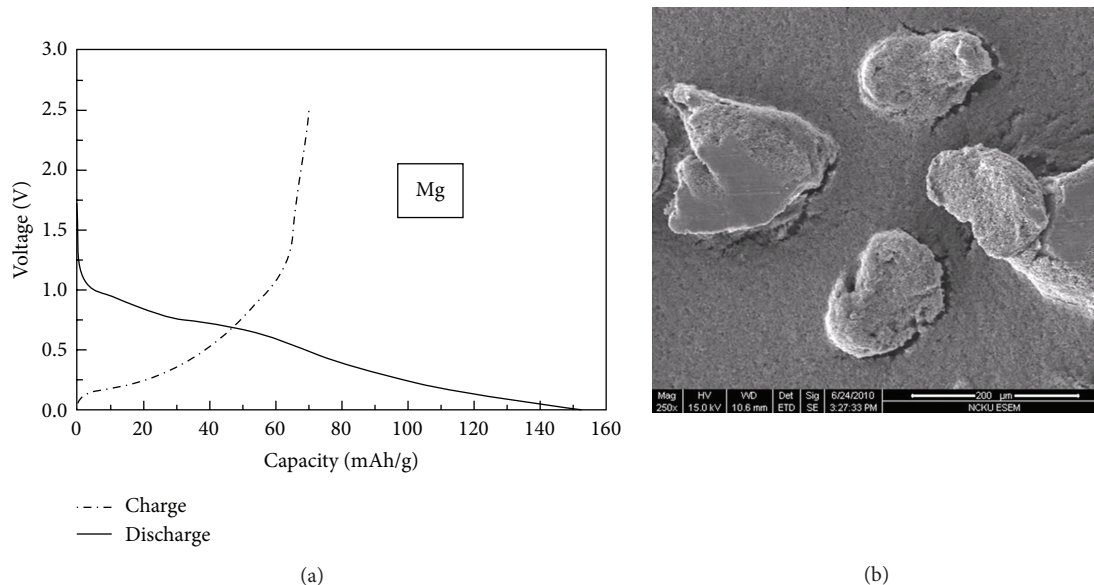


FIGURE 1: The electrode of pure Mg powder: (a) charge-discharge curve of the first cycle and (b) surface characteristic.

ion content in the electrolyte is determined to understand the influence of heat and clarify the contribution of Ni addition.

2. Experimental Procedures

An insufficient Ni powder concentration does not lead to the generation of a sufficient passivation layer around the Mg powder. An excess of Ni powder might cause more compound phases, resulting in degraded deterioration of charge-discharge capacities [6]. Therefore, magnesium-nickel (Mg-Ni) compound powders were prepared by mixing of Mg (Φ 150~180 μm) and Ni (Φ 2~5 μm) powders in weight ratios of Mg:Ni = 1:1 and then milled with a rotation rate of 600 rpm using a planetary micromill (FRITSCH GmbH, PULVERISETTE 7) to acquire alloying effect. The compound powders are designated according to the weight ratio of Mg to Ni as MNII.

The Mg-Ni compound powders were uniformly stirred with carbon black (15 wt.%) and polyvinylidene fluoride (PVDF, 15 wt.%) and then coated on copper (Cu) foils. And then, the electrodes were dried in an oven at 120°C for 1 hour. The Mg-Ni powder electrodes were cut into disks (13 mm in diameter and about 200 μm in thickness) and Li foil was used as a counter electrode (positive electrode). One M LiPF₆, ethylene carbonate (EC) and, diethyl carbonate (DEC) were used as an electrolyte and the volume ratio of EC to DEC was 1.

This study measured the surface characteristics of powder electrodes using high-resolution scanning electron microscopy (HR-SEM, HITACHI/SU8000). The electrochemical testing was performed with a lithium battery testing (LBT) cell using the battery automatic tester (BAT-750B). The cells were tested at a constant current of 20 mA·g⁻¹. Cyclic voltammetry (CV) was used to investigate the cycling efficacy with electrochemical impedance spectroscopy (EIS,

PARSTAT 2273). The electric potential was limited to the range 0~2 V and the velocity of scanning was 0.05 mV·s⁻¹. In addition, the resistances of powder electrodes after the electrochemical testing were measured using a 4-point probe. Finally, inductively coupled plasma-mass spectrometry (ICP-MS, HEWLETT PACKARD 4500) was used to determine the metal ion content in the electrolyte.

3. Results and Discussions

3.1. Charge-Discharge Characteristics of the Mg-Ni Electrodes at Room Temperature. Figure 1(a) shows the voltage profile for the first cycle of a pure Mg powder electrode at room temperature. The charge-discharge curve has a plateau at a voltage of 1.0~0.75 V, which is associated with the formation of the SEI layer [6]. The initial discharge capacity of the Mg powder electrode (151 mA·h·g⁻¹) was much lower than that of Mg film electrode (2644 mA·h·g⁻¹) in our previous experiment, which is due to the surface oxidization and looseness of the Mg powder electrode. The surface characteristics of Mg powder electrode before charging and discharging is shown in Figure 1(b). Some cracks appear on the surface of the electrode, which allowed the Li ions to react with the Cu foil, resulting in degraded charge-discharge capacities. Although the Mg film electrode has good charge-discharge characteristics, the electrochemical reaction might be an explosion hazard due to its activity [1]. Adding Ni powder to Mg powder can promote structural compactness, which may improve the charge-discharge characteristics of a battery. Therefore, the Ni powder was mixed with Mg powder to form a compound phase around Mg powder to avoid intense electrochemical reaction.

Figure 2(a) shows the initial charge-discharge profiles of the MNII powder electrodes at room temperature. Compared to the initial discharge capacity of the pure Mg powder

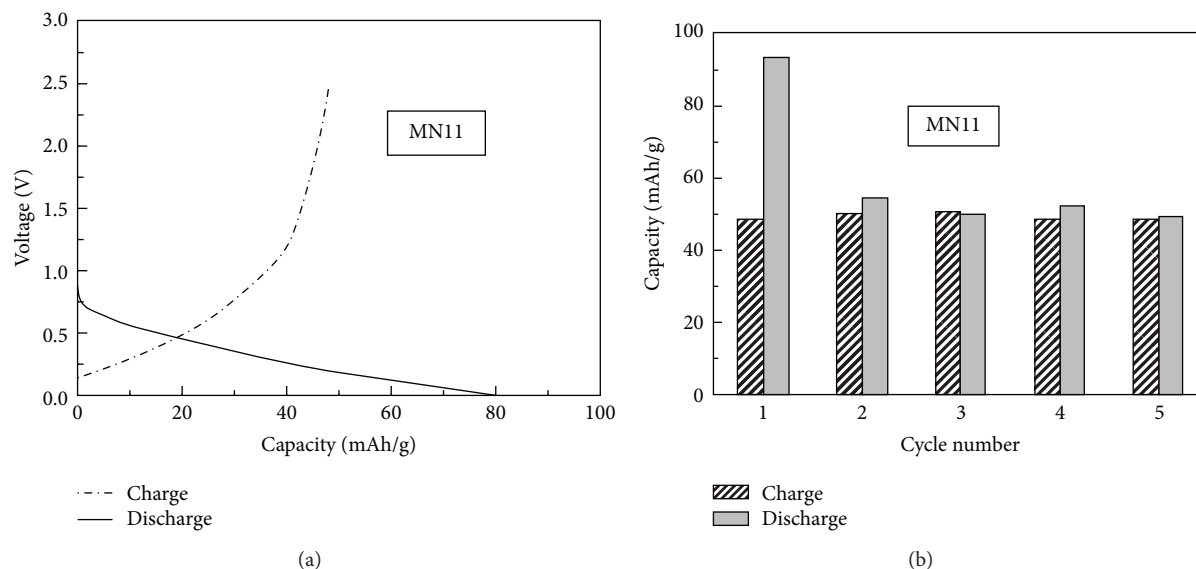


FIGURE 2: MN11 compound powders at room temperature: (a) charge-discharge curves of the first cycle and (b) charge-discharge capacities as a function of cycle number.

electrode, that of MN11 powder electrodes was low, indicating that Mg activity was restrained by Ni [15]. Previous studies [6, 16] have indicated that the Mg_2Ni and $MgNi_2$ alloy phases generated in the Mg-Ni alloy system can restrain volume expansion and thus improve the cycling life of a battery. There is a voltage plateau at 0.2~0.5 V, indicating that the Li ions became embedded in the positive electrode (Li foil). The potential voltage of 0.5~1.25 V was associated with some Li ions moving out from the electrode matrix. The charge-discharge capacities as a function of cycle number for the MN11 powder electrode at the room temperature are shown in Figure 2(b). In addition to having higher initial discharge capacity, MN11 electrode had stable charge-discharge characteristics in the subsequent electrochemical reactions. This result may attribute to the formation of the SEI layer in the initial charge-discharge reaction [17]. Generally, the charge-discharge characteristics of battery could gradually deteriorate with cycling [18]. However, the proposed MN11 electrode still maintained stable charge-discharge capacities due to alloying effect reduced oxidation problem.

3.2. High-Temperature Cycling Performance. In general, the cycle life of a battery operated in a high-temperature environment deteriorates quickly. In order to understand the effects of heat treatment on the cycling performance of batteries, the charge-discharge characteristics at 55°C were tested. The initial discharge curve of the MN11 electrode at 55°C has two plateaus, at voltages of 0.9 and 0.2 V, respectively (Figure 3(a)). The plateau at 0.9 V only appears in the initial discharge curve, indicating that the SEI layer formed [17]. The voltage plateau at 0.2~0 V appears in every discharge curve and is attributed to the potential of lithiation and delithiation [8]. In a high temperature environment, the voltage plateau at 0.2~0 V was longer compared to that of the Mg-Ni electrode at room temperature. This result is due to more Li ions becoming embedded into the electrode matrix

at 55°C due to the high temperature increasing the kinetic energy and chemical activity. Figure 3(b) clearly shows that the cycling capacities of the battery increased with increasing cycle number. This reveals that the Li foil (positive electrode) could more easily react with the electrolyte to liberate more Li ions in the cell at 55°C. Also, the heat affected the diffusion rate of Li ions in the cell. Although a high temperature environment enhances capacity, the cycling performance of the battery deteriorates more quickly. Nevertheless, the Mg-Ni powder electrode had good high temperature cycling characteristics. In fact, some Li ions did not participate in the reaction at room temperature. At 55°C, the heat enhanced the kinetic energy and chemical activity, promoting more Li ions to participate in the reaction and caused the diffusion rate of Li ions to increase with increasing the duration of electrochemical reactions.

To investigate the thermal effect on the electrochemical reaction, the cyclic voltammetry (CV) of the MN11 electrode at 55°C is presented in Figure 4. There is a peak at 0.25 V in the charge curve, indicating that a large number of Li ions inserted into the MN11 electrode. After the first cycle, the irreversible reaction is associated with the formation of the SEI layer [19]. With increasing the cycle number, the peak at 0.25 V gradually increased, indicating that cycle performance improved, which is consistent with Figure 3(b). In addition, the potential voltage shifted, which is related to the variation of the internal resistance of the powder electrode [20].

After 5 charge-discharge cycles, the surface characteristics of the MN11 electrode at room temperature (MN11-RT) and 55°C (MN11-HT) were recorded to clarify the growth behavior of the SEI layer (Figure 5). The surface morphology of the MN11-RT powder electrode shows many cracks (Figure 5(a)). The continuous lithiation and delithiation reactions caused a volume expansion of the electrode, resulting in the fracture of the SEI layer [21]. For the MN11-HT electrode, the electrode surface has a dense SEI layer

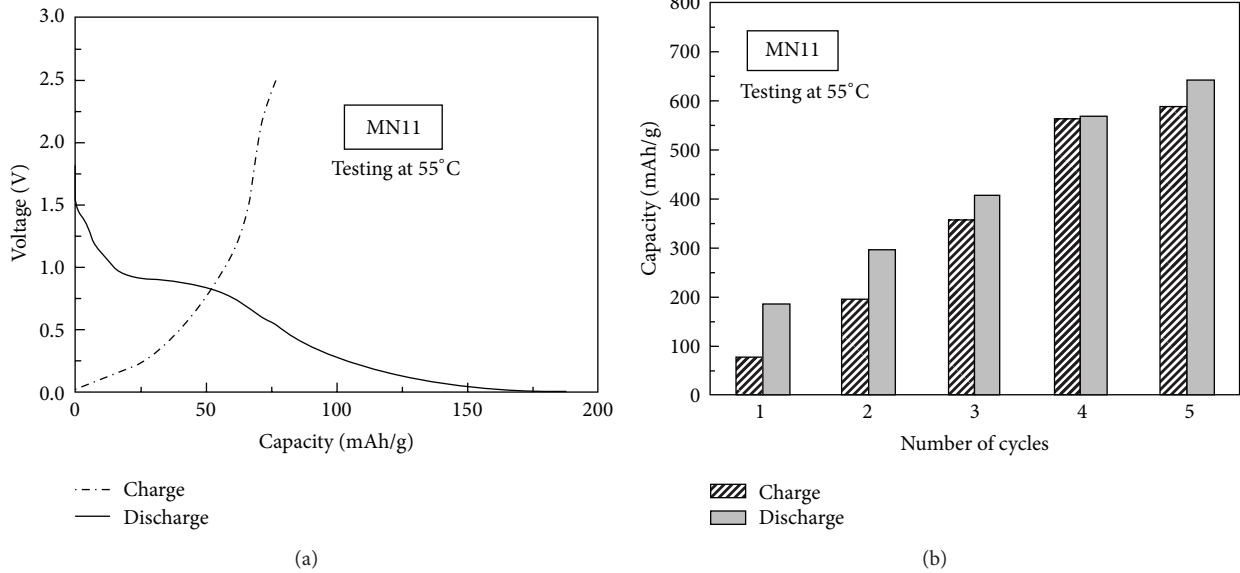


FIGURE 3: (a) Initial charge-discharge curves and (b) charge-discharge capacities as function of cycle number for MN11 compound electrode at 55°C.

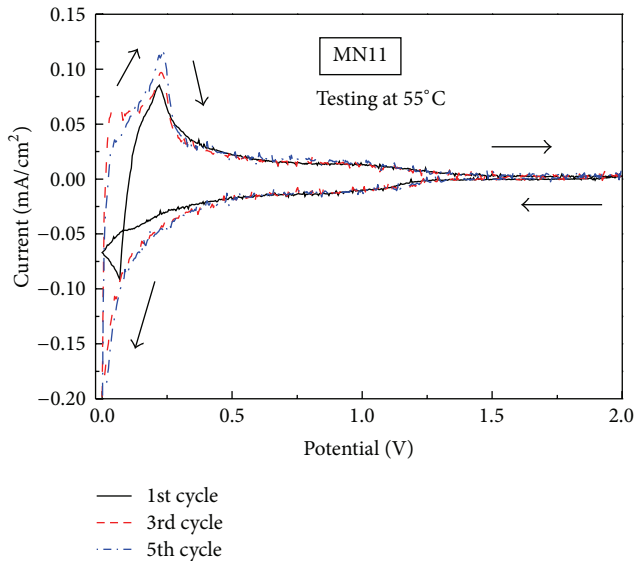


FIGURE 4: Cyclic voltammograms of MN11 electrode with 55°C measured for 5 cycles at scan rate of 0.05 mV s^{-1} .

and fewer cracks (Figure 5(b)). The growth rate of the SEI layer was faster in the high temperature environment [22]; the electrode surface was covered with thicker SEI layer. As a result, the thicker SEI layer was more able to resist the volume expansion of the electrode.

In addition, the SEI structure might decompose during the electrochemical reaction at high temperature, as its thickness did not continuously increase. This explains the improved charge-discharge characteristics of the Mg-Ni electrode at high temperature. The cracks may affect the resistance of the electrode. Therefore, the resistivity of MN11-RT

TABLE 1: The resistance value of the Mg-Ni electrode at room temperature (RT) and 55°C (HT) after different charge-discharge cycling.

Sample	Resistivity ($\Omega \cdot \text{cm}$)		
	1st cycle	3rd cycle	5th cycle
MN11-RT	4.0×10^4	5.6×10^3	7.8×10^3
MN11-HT	2.1×10^4	2.2×10^3	1.7×10^3

TABLE 2: The dissolution of metal ions concentration in an electrolyte for MN11 and pure Mg electrode.

Sample	Ion concentration ($\mu\text{g} \cdot \text{mL}^{-1}$)	
	Mg	Ni
MN11	2.760	0.469
Mg	5.709	N/A

and MN11-HT electrodes at various charge-discharge cycles were measured (Table 1). The resistance of the MN11-RT electrode decreased from the first to the third cycles and then increased. The main reason was that the intense volume expansion of the electrode increased the number of cracks. In contrast, the resistance of the MN11-HT electrode continuously decreased with increasing charge-discharge cycle. This result might be associated with the thicker SEI layer restraining the volume expansion, which is consistent with the CV results (Figure 5(b)).

In order to clarify the thermal effects on ion liberation behavior, the electrolyte was examined using ICP-MS (Table 2). The electrolyte of the MN11-HT electrode had fewer Mg ions ($2.760 \mu\text{g} \cdot \text{mL}^{-1}$) compared to the electrolyte of the Mg electrode ($5.709 \mu\text{g} \cdot \text{mL}^{-1}$). This result indicates that adding Ni powder can reduce the liberation of Mg ions.

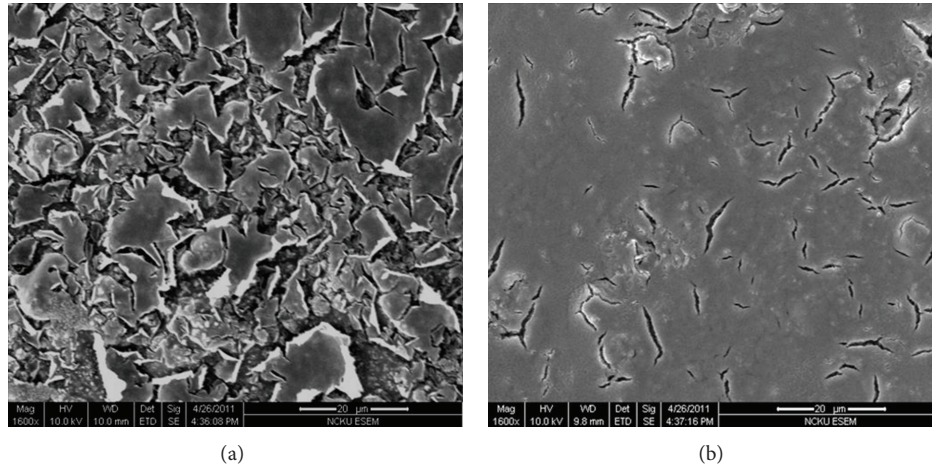


FIGURE 5: The surface characteristics of the solid electrolyte interface layer of MN11 electrode with (a) room temperature and (b) 55°C after 5 charge-discharge cycles.

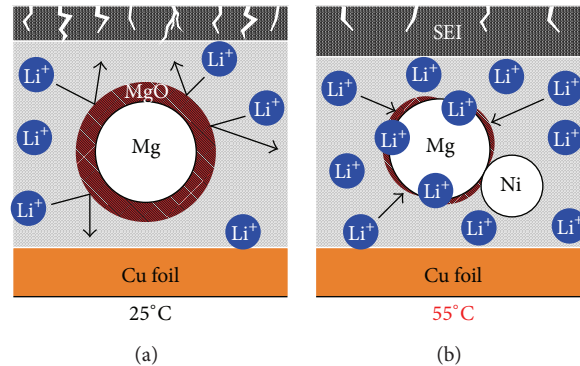


FIGURE 6: Schematic illustrations of pure Mg and the Mg-Ni electrode with the duration of the charge-discharge reactions.

In addition, the Mg-Li compound phases formed at high temperature, enhancing electrode's ability to resist fracture [23].

Schematic illustration of pure Mg and the Mg-Ni electrode with charge-discharge duration is shown in Figure 6. For the pure Mg electrode at the room temperature, the SEI layer was thinner and the volume expansion of the electrode was more obvious, resulting in serious cracks after the charge-discharge. In addition, Mg easily oxidized to form MgO phases, which decreased the activity of Mg. The MgO phases prevented Li ions to react with Mg and thus degraded the charge-discharge efficiencies. Mg-Ni compound phases could restrain the activity of Mg and the volume expansion of electrode during the charge-discharge processes. Notably, a fewer MgO phases allowed Li ions to react with Mg more easily. At 55°C, the heat increased the kinetic energy and chemical activity, making the Li ion concentration increase with increasing charge-discharge cycles. In addition, the growth rate of the SEI layer was faster, which reduced the crack density. The high temperature also caused the decomposition of the SEI layer, which prevented the SEI layer from increasing without bound. The Mg-Ni electrode at 55°C has good charge-discharge capacities, making it suitable for Li-ion battery operation at high temperature.

4. Conclusion

Ni powders mixed with Mg powders were found to effectively suppress the activity of Mg and the volume expansion of the electrode due to the formation of a passivation layer and the existence of Mg-Ni (Mg_2Ni and $MgNi_2$) alloy phases. Adding Ni powder reduced Mg dissolution without significantly degrading. At high temperature of 55°C, the charge-discharge capacities and cycling performance of the Mg-Ni alloy electrode were enhanced. The main reason was that the high temperature increased the kinetic energy and chemical activity, making the Li ion concentration increase with electrochemical reaction time. Additionally, the electrode at high temperature formed a thicker SEI layer, which resisted the volume expansion of the electrode. The decomposition of the SEI structure at high temperature caused the cycle life of the battery. The Mg-Ni alloy electrode is thus suitable for application in Li-ion batteries operated at high temperature.

Acknowledgments

The authors are grateful to the National Science Council (NSC) Instrument Center at the National Cheng Kung

University (NCKU) and National Science Council, Taiwan, for financially supporting this study under Grant nos. 101-2221-E-006-114.

References

- [1] W.-J. Zhang, "A review of the electrochemical performance of alloy anodes for lithium-ion batteries," *Journal of Power Sources*, vol. 196, no. 1, pp. 13–24, 2011.
- [2] A. R. Kamali and D. J. Fray, "Tin-based materials as advanced anode materials for lithium ion batteries: a review," *Reviews on Advanced Materials Science*, vol. 27, no. 1, pp. 14–24, 2011.
- [3] X.-Y. Zhou, J.-J. Tang, J. Yang et al., "Effect of polypyrrole on improving electrochemical performance of silicon based anode materials," *Electrochimica Acta*, vol. 70, pp. 296–303, 2012.
- [4] F.-Y. Hung, T.-S. Lui, R.-S. Xiao, Y.-W. Tseng, and C.-H. Wang, "Structural effects and charge-discharge characteristics of Mg-C/Mg-Li alloy thin film materials," *Materials Transactions*, vol. 52, no. 6, pp. 1127–1131, 2011.
- [5] D. X. Cao, L. Wu, Y. Sun, G. Wang, and Y. Lv, "Electrochemical behavior of Mg-Li, Mg-Li-Al and Mg-Li-Al-Ce in sodium chloride solution," *Journal of Power Sources*, vol. 177, no. 2, pp. 624–630, 2008.
- [6] H. Kim, B. Park, H.-J. Sohn, and T. Kang, "Electrochemical characteristics of Mg-Ni alloys as anode materials for secondary Li batteries," *Journal of Power Sources*, vol. 90, no. 1, pp. 59–63, 2000.
- [7] C.-M. Park, Y.-U. Kim, H. Kim, and H.-J. Sohn, "Enhancement of the rate capability and cyclability of an Mg-C composite electrode for Li secondary batteries," *Journal of Power Sources*, vol. 158, no. 2, pp. 1451–1455, 2006.
- [8] H. Kim, J. Choi, H.-J. Sohn, and T. Kang, "The insertion mechanism of lithium into Mg₂Si anode material for li-ion batteries," *Journal of the Electrochemical Society*, vol. 146, no. 12, pp. 4401–4405, 1999.
- [9] R. Benedek and M. M. Thackeray, "Lithium reactions with intermetallic-compound electrodes," *Journal of Power Sources*, vol. 110, no. 2, pp. 406–411, 2002.
- [10] H. Inoue, T. Ueda, S. Nohara, N. Fujita, and C. Iwakura, "Effect of ball-milling on electrochemical and physicochemical characteristics of crystalline Mg₂Ni alloy," *Electrochimica Acta*, vol. 43, no. 14–15, pp. 2215–2219, 1998.
- [11] R. A. Varin, T. Czujko, and J. Mizera, "Microstructural evolution during controlled ball milling of (Mg₂Ni+MgNi₂) intermetallic alloy," *Journal of Alloys and Compounds*, vol. 350, no. 1–2, pp. 332–339, 2003.
- [12] S. G. Zhang, Y. Hara, T. Morikawa, H. Inoue, and C. Iwakura, "Electrochemical and structural characteristics of amorphous MgNi_x ($x \geq 1$) alloys prepared by mechanical alloying," *Journal of Alloys and Compounds*, vol. 293, pp. 552–555, 1999.
- [13] G. Liu, S. Xi, G. Ran, K. Zuo, P. Li, and J. Zhou, "A new phase MgNi₃ synthesized by mechanical alloying," *Journal of Alloys and Compounds*, vol. 448, no. 1–2, pp. 206–209, 2008.
- [14] M. Anik, G. Özdemir, N. Küükdeveci, and B. Baksan, "Effect of Al, B, Ti and Zr additive elements on the electrochemical hydrogen storage performance of MgNi alloy," *International Journal of Hydrogen Energy*, vol. 36, no. 2, pp. 1568–1577, 2011.
- [15] S.-S. Lee, K.-W. Kim, B.-Y. Hur, T.-H. Nam, and H.-J. Ahn, "A study on the electrochemical properties of an Mg-Ni based thin film electrode for a microbattery," *Metals and Materials International*, vol. 7, no. 3, pp. 265–268, 2001.
- [16] R. A. Varin, T. Czujko, and J. Mizera, "The effect of MgNi₂ intermetallic compound on nanostructurization and amorphization of Mg-Ni alloys processed by controlled mechanical milling," *Journal of Alloys and Compounds*, vol. 354, no. 1–2, pp. 281–295, 2003.
- [17] C.-H. Wu, F.-Y. Hung, T.-S. Lui, and L.-H. Chen, "Microstructures and the charge-discharge characteristics of advanced Al-Si thin film materials," *Materials Transactions*, vol. 51, no. 10, pp. 1958–1963, 2010.
- [18] A. Etienneble, S. Rousselot, W. Guo, H. Idrissi, and L. Roué, "Influence of Pd addition on the electrochemical performance of MgNi₂TiAl-based metal hydride for NiMH batteries," *International Journal of Hydrogen Energy*, vol. 38, no. 17, pp. 7169–7177, 2013.
- [19] C.-H. Wang, F.-Y. Hung, T.-S. Lui, and L.-H. Chen, "The charge-discharge characteristics of woody carbon modified with Fe₃O₄ nano phase using the hydrothermal method," *Materials Transactions*, vol. 51, no. 1, pp. 186–191, 2010.
- [20] K.-L. Lee, J.-Y. Jung, S.-W. Lee, H.-S. Moon, and J.-W. Park, "Electrochemical characteristics of a-Si thin film anode for Li-ion rechargeable batteries," *Journal of Power Sources*, vol. 129, no. 2, pp. 270–274, 2004.
- [21] Y. Liu, H. Pan, M. Gao, H. Miao, Y. Lei, and Q. Wang, "Function of Al on the cycling behavior of the La-Mg-Ni-Co-type alloy electrodes," *International Journal of Hydrogen Energy*, vol. 33, no. 1, pp. 124–133, 2008.
- [22] H. Song, Z. Cao, X. Chen et al., "Capacity fade of LiFePO₄/graphite cell at elevated temperature," *Journal of Solid State Electrochemical*, vol. 17, pp. 559–605, 2013.
- [23] R. A. Guidotti and P. J. Masset, "Thermally activated ("thermal") battery technology. Part IV. Anode materials," *Journal of Power Sources*, vol. 183, no. 1, pp. 388–398, 2008.